


Title	Polymer and metallodielectric based photonic crystals
Author(s)	Kassim, Syara
Publication date	2014
Original citation	Kassim, S. 2014. Polymer and metallodielectric based photonic crystals. PhD Thesis, University College Cork.
Type of publication	Doctoral thesis
Rights	<p>© 2014, Syara Kassim.</p> <p>http://creativecommons.org/licenses/by-nc-nd/3.0/</p> 
Item downloaded from	http://hdl.handle.net/10468/2043

Downloaded on 2017-02-12T13:47:27Z



UCC

University College Cork, Ireland
Coláiste na hOllscoile Corcaigh

POLYMER AND METALLODIELECTRIC BASED PHOTONIC CRYSTALS



A thesis submitted for the degree of
Doctor of Philosophy
to the
Chemistry Department
University College Cork

Syara Kassim

2014

Supervisor and Head of Department: **Prof. Dr. Martyn E. Pemble**



Advanced Materials Surface Group

Tyndall National Institute,

University College Cork, Dyke Parade, Cork, Ireland.

Table of Contents

Table of contents	i
Dedication	vi
Acknowledgements	vii
Statement in lieu of an oath.....	ix
Glossary	x
Abstract.....	xiv
Thesis content	xvii
Chapter 1 Polymer and Metallodielectric Photonic Crystals (MDPCs)	1
1.1 Introduction to Photonic Crystals	1
1.2 Colloidal Photonic Crystals	6
1.3 Self-Assembly of Photonic Crystals	9
1.4 Metallodielectric Materials and their Properties	13
1.4.1 Metallodielectrics	13
1.4.2 Surface Plasmon Resonance (SPR)	15
1.4.3 Inverse Opals	17
1.4.4 Synthesis of Highly Monodisperse PMMA@Au Core-Shell Particles.....	20
1.5 Objectives	22
References	23
Chapter 2 Experimental Techniques.....	34
2.1 Materials	34

2.2	Synthesis of Monodisperse PMMA Colloidal Spheres	35
2.3	Substrates Cleaning	37
2.4	Self-Assembly Evaporation Experimental	38
2.5	Dip Coating	41
2.6	Synthesis of PMMA@Au Core-Shell Particles	42
2.7	Electrochemical Deposition of Gold and Nickel into PMMA Photonic Crystal Templates.....	43
2.8	Co-Crystallisation of Silica Sol/Au NPs/PMMA and the Subsequent Inverted Structure	44
2.9	Co-Crystallisation of Silica Sol/PMMA and the Subsequent Silica Inverted Structure	44
2.10	Instrumentation and Characterisation	45
2.10.1	Optical Characterisation	45
2.10.2	Scanning Electron Microscope (SEM)	46
2.10.3	Transmission Electron Microscope (TEM)	46
2.10.4	UV Visible Absorption Spectroscopy	47
2.10.5	Zeta Potential	47
2.10.6	Raman Spectroscopy	47
References	48
Chapter 3	Synthesis of Poly(methyl methacrylate) Spheres	49
3.1	Introduction.....	49
3.2	Synthesis of Monodisperse PMMA Spheres.....	50
3.3	Conclusions.....	60
References	62

Chapter 4 Synthesis of Highly Monodisperse Poly(methyl methacrylate)-Au Core-Shell Particles and their use in the Fabrication of 3-D Metallodielectric Photonic Crystals.....	64
4.1 Introduction.....	64
4.2 Preparation of Gold Nanoparticles	66
4.3 Synthesis of PMMA@Au Core-Shell Nanoparticles	69
4.4 Fabrication of PMMA@Au Photonic Crystal Films	79
4.5 Optical Properties of PMMA@Au Core-Shell Photonic Crystal Films.....	80
4.6 Conclusions.....	86
References	88
Chapter 5 Preparation of Gold and Nickel Metallodielectric Photonic Crystals (MDPCs) using PMMA Spheres via Electrodeposition	92
5.1 Introduction.....	93
5.2 Preparation of Gold Infiltrated Opals and Inverse Opal.....	95
5.2.1 Gold Infiltration	95
5.2.2 Inverted Structure of Gold.....	96
5.3 Preparation of Nickel Infiltrated Opal and Inverse Opal.....	98
5.3.1 Nickel Infiltration.....	98
5.3.2 Inverted Nickel	98
5.4 Optical Properties	101
5.5 Conclusions and Future Work.....	104
References	108

Chapter 6 Colloidal Co-Crystallisation: A New Route to the Production of Three-Dimensional Metallodielectric Photonic Crystals	110
6.1 Introduction	110
6.2 SEM of Silica-PMMA Composite, Silica Inverse Opal and Metallodielectric Inverse Opal.....	112
6.3 Optical Properties	115
6.4 Conclusions.....	123
References	125
Chapter 7 A Bottom-Up Fabrication Method for the Production of Visible Light Active Photonic Crystals	128
Chapter 8 Summary, Conclusions and Suggestions for Future Work.....	137
8.1 Summary and Conclusions	137
8.2 Suggestions for Future Work.....	139
Appendix A: Preliminary Studies of the use of Metallodielectric Photonic Crystals as Substrates for Surface-Enhanced Raman Spectroscopy	141
A.1 Introduction.....	141
A.2 Results and Discussion	144
A.2.1 Optical Absorption from PMMA: Au Nanoparticle Composite Films.....	144
A.2.2 Surface-Enhanced Raman Spectroscopy (SERS) Effects	146
A.3 Conclusion	151
References	152

Appendix B: Preparation and Properties of Silica Inverse Opal via Self-Assembly.....	155
Appendix C: Chapter 7, Figure 1 (f) & (h) enlarged for clarity.....	164
Appendix D: List of Publications and Conference Presentations	165

Dedication

In the name of Allah the Most Gracious and the Most Merciful.

I dedicate this work to the loving memory of my father. May Allah S.W.T. grant you a jannah. Al-Fatihah.

To my mother, sacrifice for the sake of raising their children after the death of my father, no words are sufficient to describe your contribution to my life. I owe every bit of my existence to you.

To my Husband, who has supported me in all my endeavours’.

To my son and daughter, the great God-given, who makes life more filled and exciting.

Acknowledgements

First and foremost, I would like to thank my supervisor Prof. Dr. Martyn E. Pemble for giving me the opportunity to start my research career. I am indebted to my Professor for his consistent support and kind assistance in all aspects of my PhD life has made my time a joyful and unforgettable experience. I am grateful to Dr. Siby Padmanabhan, Dr. Joe Mc Grath and Dr. Maria Bardosova without whom this thesis would not have been possible. I am thankful for the unparalleled level of supervision that they have offered in relation to my thesis work; I sincerely appreciate the friendships, encouragement, criticisms, unlimited support and invaluable guidance I have received during the past four and half years.

I owe my deepest gratitude to Prof. Dr. Justin Holmes for his encouragement, insightful comments, and hard questions. I cannot find words to express my gratitude to colleagues who supported my research work: Patrick Coralan, Vince Lodge, Mary-Claire O'Regan and the other members of the Advanced Materials and Surfaces Group within the Tyndall National Institute for all their help, friendship and fun.

This thesis is dedicated to my husband and son who have always stood by me and all my family members who dealt with my absence from many family occasions with a smile. I would like to thank my beloved husband who sacrificed a lot and understands my career

as a student, wife and mother to our son Mohd Arief Hakim and little baby girl named Nur Safiyah Eryna who was born recently- on the 27th August 2014. Their encouragement and support have been priceless. I am so grateful for their love, support and patience. To my friends Dr. Aniza Harun and Dr. Azrilawani Ahmad who has always encouraged me in this journey of my Ph.D life.

My sincere gratitude also to the Ministry of Higher Education, Malaysia and Universiti Malaysia Terengganu, Malaysia who have sponsored my studies and Science Foundation Ireland (SFI) Principal Investigator Grant 07/IN.1/I787 who funded this research.

Statement in lieu of an oath

I hereby declare in lieu of an oath that I have composed this thesis independently with help from my supervisors and permitted aids only. There has not been assistance from any prohibited means.

I also declare that all parts which have been taken from published and unpublished sources, documents or talks and have been reproduced whether as original, slightly changed or in thought, have been mentioned as such at the corresponding places in the thesis by citation, where the extent of the original quotes is indicated.

Cork, Aug 2014

A handwritten signature in blue ink, reading "Syed Rafiq Kassim". The signature is written in a cursive style with a horizontal line underneath.

Glossary

Chemicals

$(\text{CH}_3)_2\text{CO}$	Acetone
H_3BO_3	Boric acid
HCl	Hydrochloric acid
H_2O_2	Hydrogen peroxide
H_2SO_4	Sulphuric acid
NaBH_4	Sodium borohydrate
HAuCl_4	Chloroauric acid
KPS	Potassium persulfate
MMA	Methyl methacrylate
N_2	Nitrogen
NH_4OH	Ammonium hydroxide
$\text{Na}_3\text{C}_6\text{H}_5\text{O}_7 \cdot 2\text{H}_2\text{O}$	Trisodium citrate dihydrate
NiCl_2	Nickel chloride
NiSO_4	Nickel sulfate
PEI	Polyethelnyimine
PMMA	Poly(methyl methacrylate)
PSSS	poly(sodium 4-styrene sulfonate)
TEOS	Tetraethyl orthosilicate

Abbreviations

AACVD	aerosol assisted chemical vapour deposition
ALD	atomic layer deposition
cPBG	complete photonic bandgap
CS	core-shell
CSS	core-shell-shell
CVD	chemical vapour deposition
FCC	face-centered cubic
FIB	focus ion beam
LED	light emitting diode
ITO	indium tin oxide
LBL	layer-by-layer
LSPR	localized surface plasmon resonance
MDPC	metallodielectric photonic crystal
NP	nanoparticle
PhC	photonic crystal
PL	photoluminescence
RPM	revolutions per minute
SAED	selected area (electron) diffraction
SEM	scanning electron microscope
SERS	Surface-enhanced Raman spectroscopy or surface-enhanced Raman scattering

SPR	surface plasmon resonance
SSV	sphere segment void
TEM	transmission electron microscope
TSC	Trisodium citrate dihydrate
UV	ultra violet
XRD	X-ray diffraction

Symbols

d	periodicity of the structure
D	diameter
°C	degree Celsius
h	hour
θ	angle of incident
η	refractive index
η_{eff}	effective refractive index
λ	wavelength
ζ	zeta potential
s	second
T	temperature
t	time
μ	micro
V	volume fraction
V	volt

Abstract

The so-called bottom-up colloidal synthesis of photonic band gap (PBG) materials or photonic crystals (PhCs) has attracted considerable interest over the top-down approaches due to the relatively simple processing steps involved, the potential for large area sample production and the relatively low-costs associated with this approach for the fabrication of complex 3-dimensional (3D) structures. Accordingly, this thesis focuses on the use of this bottom-up approach in the fabrication of polymeric colloidal PhCs and their subsequent modification.

Poly(methyl methacrylate) (PMMA) was used both as a host material and as a crystal template in order to produce opals, inverse opals or 3D metallodielectric photonic crystal (MDPC) structures. The fabrication of MDPCs with Au nanoparticles attached to the PMMA spheres, referred to as PMMA@Au core-shell particles, is described. These have potential for use in the creation of sensors or so-called complete PBG materials. The incorporation of metallic nanostructures such as Au, is interesting because such nanostructures possess surface plasmon resonances (SPRs), which manifest as additional absorption bands, when the incident photon frequency is resonant with the collective oscillation of the conduction electrons. Various alternative procedures for the fabrication of PhCs and MDPCs are described and preliminary results on the use of an Au-based MDPC for surface-enhanced Raman scattering (SERS) are presented. These preliminary results suggest perhaps a threefold increase of the Raman signal with the MDPC as compared to the bare PMMA PhC.

The fabrication of PMMA-gold and PMMA-nickel MDPC structures via an optimised electrodeposition process is described. This process results in the formation of a continuous dielectric-metal interface throughout the 3D PhC structure from which the polymer host may be simply removed by solvent washing, leaving metal-air structures consisting of gold and nickel, which are shown to possess interesting optical properties.

The fabrication of a robust 3D silica inverted structure with embedded Au nanoparticles (Au NPs) is described by way of illustrating a novel co-crystallisation method. This method is demonstrated to be capable of creating a SiO₂/Au NP composite structure in a single step process, following which the corresponding inverted structure may be simply created by removal of the host PMMA spheres. Although this work focuses on the creation of photonic crystals, the simplicity of the approach described clearly makes it a candidate for the creation of other types of functional materials.

A new method for the fabrication of inverted opals containing pre-formed ‘designer’ silicon nanoparticles using aerosol assisted chemical vapour deposition (AACVD) is described. Silicon is a relatively high dielectric material and nanoparticles of silicon are capable of improving the visible light band gap properties and absorption properties of the resulting structure, and therefore the approach described has the potential to be exploited in photovoltaic devices. Importantly, the AACVD process is shown to result in

the incorporation of the Si NPs without any evidence of additional oxidation- the particles are effectively Si, with a thin SiO₂ shell, and are not all SiO₂.

Thesis content

This thesis reports a study on polymer and metallodielectric based photonic crystals. PMMA was used in all cases as the standard material, and as a crystalline template in producing inverse opals. This thesis also discusses the metallic components employed in the fabrication of metallodielectric photonic crystals. The content of each chapter is summarised below.

Chapter 1 has presented a brief introduction to photonic crystals, with placing an emphasis on the previous work related to this thesis. It describes the effects of materials with interesting physical/chemical properties that can be incorporated into photonic crystals. Specifically, these are the structure-related optical properties of colloidal crystals, and surface plasmon resonance theory on spheres coated with metal/metal inverse opal.

Chapter 2 describes the experimental techniques adopted. The experimental work in this PhD project can be divided into five parts: 1st, synthesis of the colloidal spheres (PMMA); 2nd, the preparation of colloidal crystal samples on substrate via self-assembly processes; 3rd, infilling metals (e.g Ni and Au) into the 3D PMMA crystal template via an electrodeposition process, and the subsequent conversion of the resulting structures to inverted structures; 4th, synthesis of Au nanoparticles and PMMA@Au core-shell particles; 5th, co-crystallisation of film involving PMMA spheres, Au NPs and hydrolysed TEOS to form metallodielectric photonic crystals (MDPC) and inverted MDPC and silica

inverse opals prepared for comparison; 6th, the characterization of samples by SEM, TEM and their optical measurement.

Chapter 3 deals with the preparation of PMMA colloidal spheres via modification emulsifier-free polymerisation in a water based system. Parameters such as temperature of the reaction, concentration of monomer methyl methacrylate and initiator, were investigated to yield monodisperse PMMA particles of varying sizes. All particles were measured under SEM to determine the average particle size and to confirm their quality of mono-dispersion.

Chapter 4 reports on the use of particles made from Au nanoparticles embedded onto the PMMA spheres, so called PMMA@Au core-shell particles. These colloidal PMMA@Au core-shell particles were then assembled by a controlled evaporation process onto glass substrates, and their optical properties measured.

Chapter 5 describes the formation of a PMMA opal on a conductive substrate (e.g Au, ITO surface) followed by a metal infilling process (Au and Ni) via electrodeposition, and their conversion into inverse opal films

Chapter 6 relates to co-crystallisation of PMMA, Au NPs and hydrolysed TEOS to fabricate a MDPC structure. The PMMA was removed to form a silica-Au inverse opal.

The optical properties of bare PMMA, silica inverse opal and MDPC are discussed further.

Chapter 7 presents a paper published in Journal of Materials Chemistry C, entitled ‘A Bottom-Up Fabrication Method for the Production of Visible Light Active Photonic Crystals’. In this work, silica inverse opals were first prepared via co-crystallisation, and then silicon nanocrystals (ncSi) were integrated into the silica inverse opal template by a modified aerosol assisted CVD (AACVD) process.

Chapter 8 summarises the thesis and provides an outlook of future research.

Appendix A introduces preliminary studies of the use of metallodielectric photonic crystals as substrates for surface-enhanced Raman spectroscopy.

Appendix B present a paper entitled “Preparation and Properties of Silica Inverse Opal via Self-Assembly”.

Appendix C gives Chapter 7, Figure 1 (f) and (h) enlarged for clarity.

Appendix D is list of publications and conference presentations.

Chapter 1: Polymer and Metallodielectric Photonic Crystals (MDPCs)

1.1 Introduction to Photonic Crystals

Photonic crystals (PhCs) are periodic systems that consist of separate high dielectric and low dielectric regions which exhibit diffraction-based phenomena called stop bands. A PhC is said to be a “crystal” because it is formed by a periodic arrangement of basic building blocks. The term “photonic” is added since photonic crystals are designed to affect the propagation properties of photons. Depending on the periodic structure involved, photonic crystals may have a 1D, 2D or 3D framework. The dimensionality is based on how the differing refractive index materials align within the crystal. In a 1D photonic crystal the refractive index varies along one direction only, while in 2D and 3D photonic crystals the refractive index varies along two and three axes respectively. Figure 1.1 illustrates the structures of one-, two-, and three-dimensional photonic crystals that can be engineered based on a conceptual view of this phenomenon using a simple cubic example [1].

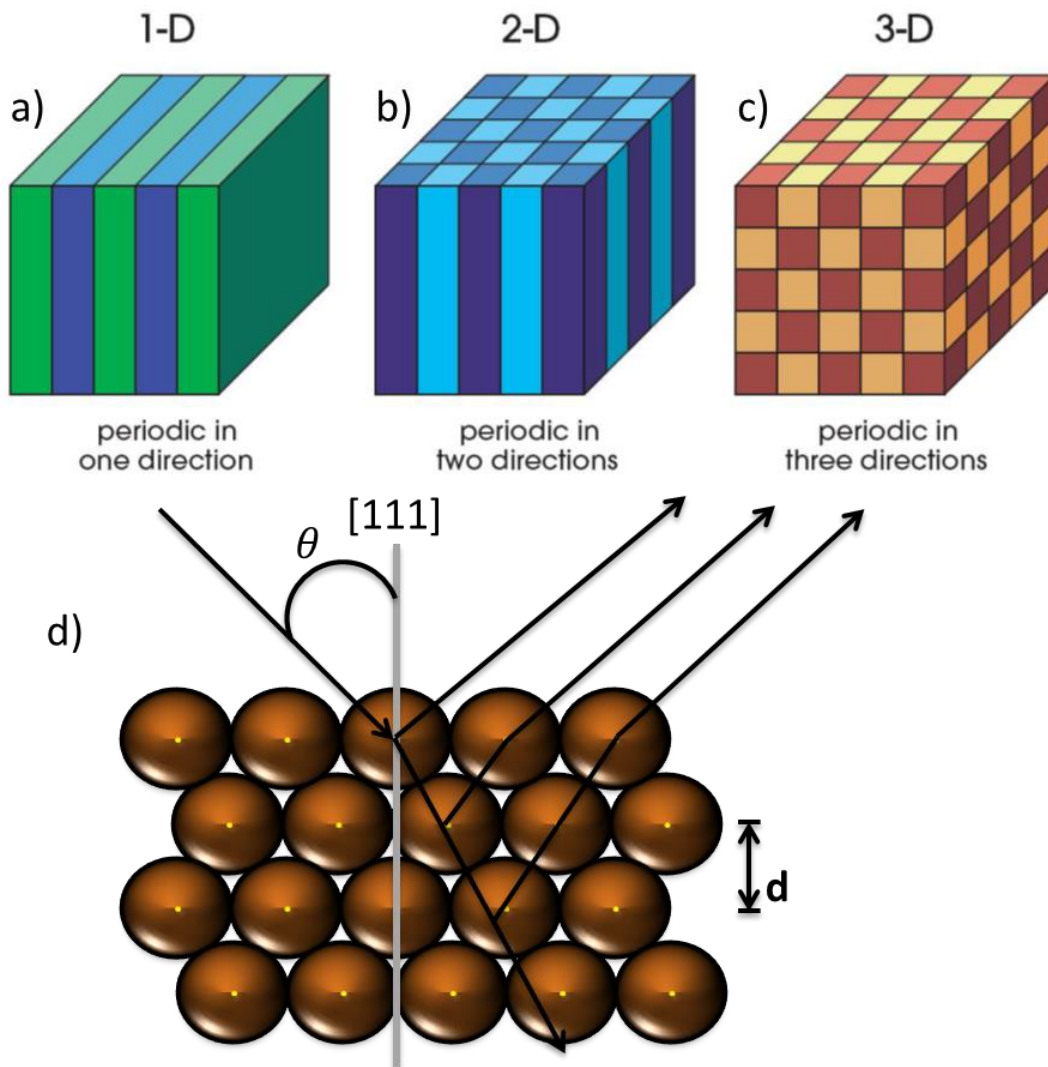


Figure 1.1 Schematics of (a) one-, (b) two-, and (c) three-dimensional photonic crystals. (Taken from [1]). (d) Incident light with a wavelength predicted by a modified Bragg equation (Eq.1.1) undergoes diffraction when propagating through a photonic crystal. The wavelength of light that is coherently scattered is centred on λ , and can be estimated from the angle of incidence, θ , the effective refractive index, η_{eff} , and the periodicity of the structure, d .

Chapter 1

In particular, three-dimensional photonic crystals with a sufficiently high value of refractive index contrast, $\Delta\eta$ between the constituent phases, may possess a full photonic bandgap, where light of a specific wavelength range is inhibited from propagating in all directions.

In general, the propagation of a wave is affected when it enters into a material where some feature that concerns this wave is modulated. In the case of photons this feature is the RI. The wave scatters coherently at the interfaces between different featured regions. The behaviour of a photon with a certain frequency will depend on the propagation direction within the photonic crystal. The modulation of the RI will result in the observation that certain energies and directions, wave vectors, are forbidden for the photons in question. A region of energies where the photonic crystal does not allow photons to propagate regardless of their direction and polarization is called a complete photonic band gap (cPBG) [2-5]. Structures with sufficiently large variations in refractive index $\Delta\eta$ (>2.8) have been predicted to exhibit a complete band gap, which would stop the transmission of particular wavelengths of light through the crystal from any direction, allowing control over the location, direction, and emission of light [6-8]. However, significant reflection can be observed, even for lower values of the refractive index contrast. Inverse opals can illustrate this phenomenon, as they have a uniform arrangement of void spaces containing air (with a low refractive index of 1.000) and solid walls (with a higher refractive index, e.g. 1.455 for silica). A peculiar property of these materials is their ability to “filter” light. When white light, which contains all visible

Chapter 1

colours of light, is incident on a photonic crystal, some wavelengths are forbidden from passing through the material, being reflected instead (Figure 1.2). The remaining wavelengths are unaffected by the photonic crystal, and they simply pass through. For complete reflection, the refractive index of the wall material must exceed a value of 2.8 [9].

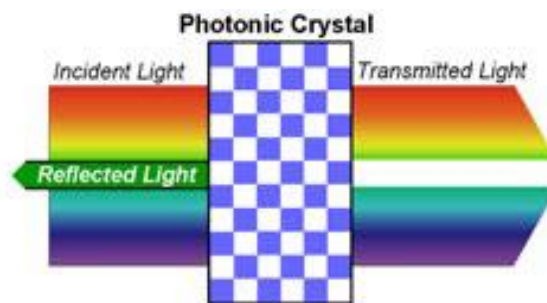


Figure 1.2 Interaction of white light (which contains all visible colours) with an inverse opal photonic crystal. When white light impinges upon a photonic crystal, a range of light wavelengths is reflected, while the remaining light is transmitted. Taken from [9].

The term “Photonic Crystal” is therefore coined to signify the similarity between photonic crystals that act upon photons and atomic crystals that act on electrons therein. The periodicity of spacing determines the relevant light frequencies. Application of these properties to Bragg’s law of diffraction and Snell’s law which relates to refraction led to development of the modified Bragg-Snell law (Equation 1.1), which provides a useful means of explaining the position of the stop-band and for calculating the effective refractive index:

$$\lambda = 2d \sqrt{(\eta^2_{eff} - \sin^2 \theta)}$$

Equation 1.1

Chapter 1

Upon calculating the effective refractive index of the photonic crystal sample the refractive indices of the contrasting materials can be calculated separately via the following equation:

$$\eta_{eff} = \sqrt{(\eta_1^2 V_1 + \eta_2^2 V_2)} \quad \text{Equation 1.2}$$

Where η is the refractive index of the respective materials and V is the volume fraction of the respective materials [10].

Where the PhC is fabricated from layers of assembled particles which is the case for the materials described in this thesis

$d = \text{periodicity or layer spacing} = (D) * (2/3)^{1/2}$ for a face-centred cubic (FCC) structure, where D is the particle diameter

From the modified Bragg-Snell equation, the position of so-called stop band (Bragg peak) can be changed by varying one of a number of factors, either:

- D , the particle diameter: wavelength of Bragg peak increases with increasing particle size
- θ , angle of incident: wavelength of Bragg peak decreases with increasing angle of incident

- d , lattice type: the Bragg peak can be changed by changing the lattice structure from FCC to another, e.g. hexagonal structure, diamond structure, etc; or by stretching / compressing the lattice structure
- η_{eff} , effective refractive index: the position of Bragg peak can be changed by changing the construction materials of the photonic crystal

Colloidal particle systems in general and opals in particular, have been shown to present photonic crystal properties. Artificial opals are most appreciated not for their own photonic properties, but for their use as hosts to other materials and especially, as matrices for the moulding of so-called inverse opals. The emergence of artificial opals that can be grown by self-assembly from a suspension of colloidal spheres is a typical approach for forming materials with periodic structures which offers a cheap and simple approach to fabricate 3D PhCs [11-14]. Monodisperse colloidal particles can readily assemble themselves to form an FCC crystal that will be discussed in greater detail later in this thesis.

1.2 Colloidal Photonic Crystals

So-called colloidal photonic crystals are made from monodisperse colloids during a process, in which the colloidal particles self-organize or are forced into long-range-ordered crystal-like structures. Monodispersity of the colloidal particles is essential for the observation of effective ‘crystallisation’. A natural example of this phenomenon can

Chapter 1

be found in the gemstone opal and certain butterfly wings. Opals are among the most colourful of all gems despite being composed primarily of silica, a colourless solid with the chemical formula SiO_2 (opals have the same chemical composition as window glass and quartz). Their name comes from the Latin word *opalus* meaning “to see a change of colour” [9]. They exhibit a “play of colour” (opalescence), which consists of iridescent colour flashes that change with the angle at which they are viewed (Figure 1.3). In fact opals consist of spheres of amorphous silica spheres of diameters ranging from 100 nm to over 1000 nm, packed together in regular arrangements, which then display novel reflection and diffraction properties, in turn giving rise to the pleasing appearance of opal gemstones- opalescence. However, the structures present in natural opal gemstones are generally disordered because they are usually ‘polycrystalline’, but in the sense of a photonic crystal rather than a truly crystalline solid. This gives a beautiful appearance in gemstones, but it is not desirable for photonic applications. By borrowing from nature it is possible to create artificial opals and reduce the number of defects found in colloidal crystals by utilizing careful assembly methodologies. The self-assembly of colloidal crystals can be achieved by gravity sedimentation [15], crystallisation in physically confined cells [16], controlled evaporation method [12], vertical deposition [17], under oil crystallisation [18], spin coating [19], and other methods [20].

Chapter 1



Figure 1.3 Left, natural opals and right iridescent butterfly wings, are both examples of photonic engineering in nature

Among the materials used to fabricate colloidal photonic crystals, the most commonly used are silica and polymers [21-25]. Owing to a higher surface charge to density ratio, polymer particles tend to behave better than silica ones for the purpose of colloidal crystallisation [26]. One disadvantage of using colloidal silica is the need to use an aggressive hydrofluoric acid (HF) etching process to remove the silica crystal template when attempting to produce inverse opals. Herein, the first part of this research focuses on the self-assembly of colloidal crystals from polymer colloids. Monodisperse polymer colloids, mainly poly(methyl methacrylate) (PMMA) and polystyrene (PS) microspheres have been prepared via a modified emulsion polymerisation technique developed in this work. There are many advantages in using polymer colloids as building blocks in the construction colloidal crystals, including multiple choices of chemical composition, tuneable particle size, low cost and the ability to change their shape [27]. In addition, they are easily removed by solvent dissolution or thermal calcination, when acting as template

structures for macroporous materials and inverse opals. The synthesis of PMMA particles is more economical than the synthesis PS particles, and hence led us to their use in the present study. The advantages of PMMA are; less complicated apparatus required for the synthesis, shorter reaction times, higher yield and the high degree of monodispersity of the particles.

1.3 Self-Assembly of Photonic Crystals

Colloidal self-assembly is one of the most efficient methods for the fabrication of 3D photonic crystals. In this method, predesigned building blocks (usually monodispersed silica or polymer nanospheres) spontaneously organise themselves into a stable structure. Self-assembly is considered to be a cost effective method, in comparison to “top down” assembly methods, such as lithographic and other mechanised techniques to make 3D ordered photonic crystals. Lithographic techniques are based on the approach followed in microelectronics to fabricate electronic chips. The first 3-dimensional photonic structure was produced by Yablonovitch and co-workers [3], who were amongst the first to suggest constructing artificial three dimensional periodic structures designed to manipulate the propagation of light. The structure he designed now goes under name of ‘Yablonovite’ and was built on a length scale of millimetres and shown to have a complete photonic band gap, capable of prohibiting the propagation of microwaves in all directions for certain wavelengths. Later, lithographic methods were designed by Noda *et al.* [28] and Lin *et al.* [29, 30] and used for making 3D photonic crystals, often referred to as woodpile or layer-by-layer structures. Other techniques that have been used are

Chapter 1

micromanipulation [31], and a holographic technique [32, 33]. These “top down” processes are generally complex, multi-step methods (Figure 1.4). They are also generally very expensive procedures that many research laboratories cannot afford. By contrast, the self-assembly of monodisperse submicron silica or polymer spheres into colloidal crystals provides a simple, fast, and cheap materials chemistry approach to producing photonic crystals [34]. Finally, it is noteworthy that at least in principle, the method is scalable such that large area PhCs could be fabricated.

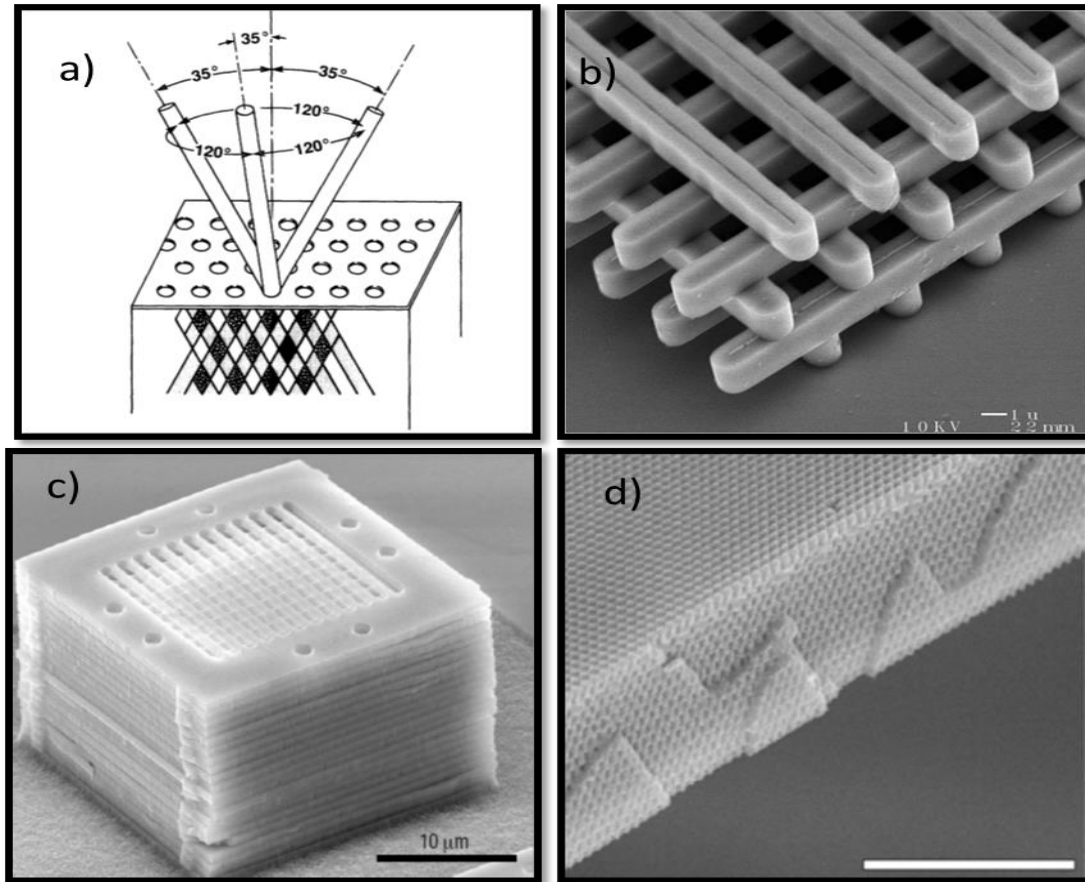


Figure 1.4 Photonic crystals fabricated by (a) drilling (Yablonovite) [3] (b) wafer etching (woodpile structure) [28-30] (c) micromanipulation [31] (d) holography [32, 33]

A number of techniques are available for colloidal self-assembly fabrication. The vertical deposition method or dip coating, is the most widely used technique for creating colloidal crystals to form high quality, large scale colloidal crystals with controllable thickness. In this project, in order to control the morphology and improve the quality of colloidal crystals, dip coating and controlled evaporation methods have been studied in detail in terms of conditions and parameters, such as temperature, solvent, humidity and the type of substrates.

Chapter 1

Self-assembly techniques constitute the most popular approach to fabricate 3D photonic crystals. Since its introduction in 1999 by Jiang *et al.* [12] the vertical deposition method has become the most widely used method within the range of self-assembly techniques employed in order to fabricate opal-based 3D photonic crystals. It is based on the convective self-assembly of colloids on a substrate by the action of a moving meniscus, which was described by Nagayama and co-workers [35]. Based on the natural tendency of monodisperse colloidal particles to organize into ordered arrays, this method represent the best option due to the ease of fabrication, producing larger areas economically.

Gu *et al.* [17] used a dipping method for the fabrication photonic crystals from polystyrene particles, the film thickness being controlled by either the particle concentration or the lifting speed.

Ye *et al.* [36] adapted the method from Gu to allow for the fabrication of opaline photonic crystals from large silica spheres (890 nm diameter) used a combination of “lifting and stirring” (where evaporation has only a minor influence on the speed of the moving meniscus). Khunsin *et al.* alternatively maintained 398 nm PMMA particles in suspension using noise vibrations, the acoustic vibration apparently giving the spheres a chance to move along the substrate and equalise the stress over the lattice, producing larger crystalline domain sizes [37].

In the most favourable situation, an artificial opal will consist of a face-centered cubic (FCC) arrangement of spheres, which, for the appropriate refractive index contrast can develop a complete photonic band gap (cPBG) [9]. Complete photonic band gaps are easily destroyed by crystal imperfections, even from a moderate amount of disorder in the positions and sizes of the voids in macroporous inverse opals. Such defects arise from both the colloidal crystal template and from the infiltration and processing steps. Defects will significantly reduce the gap and may eventually close it [38]. However, even if a cPBG is absent, these structures are interesting in their own right as they represent a playground in which one may explore the optical properties of photonic crystals.

1.4 Metallodielectric Materials and their Properties

1.4.1 Metallodielectrics

The concept of the incorporation of metals or metallic particles into PhCs has attracted interest ever since such composite systems were theoretically predicted to have potential in terms of opening up cPBGs [2, 39]. Another interesting and closely linked field that has attracted a lot of attention is plasmonics. Surface plasmons are characterized as surface bound waves that propagate at the interface between metals and dielectrics (the subject will be elaborated on more in the next section). The first three-dimensional metallic photonic crystal was proposed by the group of Yablonovitch [40]. This structure was made from metal wires based on a diamond lattice with centimetre-scale lattice spacing. A forbidden band below a cut-off frequency in GHz frequency range was

Chapter 1

demonstrated. McCalmont *et al.* [41] proposed a simpler structure based on a metallic square mesh separated by dielectric. Their results were in qualitative agreement with the Yablonovitch structure, identifying a finite cut-off frequency below which no modes could propagate. In 1999 Moroz [2] suggested that it is possible to avoid constraint on the dielectric constant by using metallic spheres coated by a dielectric layer. His results showed that the gap width can increase up to 50% as compared to the same crystal made from simple dielectric spheres. He proposed to incorporate metals into a photonic crystal having a gap in a certain frequency window, in which the metal behaves as a conventional, and a highly dispersive, dielectric. Photonic crystals that contain metals, so-called metallodielectric materials, are of additional interest because of the possible influence of the metal plasmonic resonances on the photonic band gap properties. When the metal film is corrugated, the surface plasmon experiences band gaps [42] in the same way as a mode does in a corrugated waveguide. Surface plasmons are usually associated with thin films, but they can also be observed in systems of small metal spheres [43]. The study of coupling of metal plasmonic resonance excitations with the PBG of the host opal in these structures has also gained enormous interest as they could lead to a wide range of new or improved devices including decorative coatings, sensors, photovoltaics, solar concentrators, passive optical components (filters, splitters). Chen *et al.* [44] mention that a mushroom-like composite metallodielectric nanostructure is shown to have improved characteristics for surface plasmon resonance (SPR) bio-sensing applications compared to conventional metallic nano-hole structures.

1.4.2 Surface Plasmon Resonance (SPR)

Surface plasmon resonance was first observed in 1902 by Wood [45] when he recorded an “anomalous” pattern in reflected light from a mirror with a diffraction grating on it. In 1958 Thurbadar noted a drop in reflectivity of thin metal films, which was later proven to be due to SPRs in 1968 via two separate observations- those of Otto [46] and those of Kretschmann and Raether [47]. Today we know that a surface plasmon band will be allowed and possibly observed in the presence of metals with free electrons. Free electrons at the junction of two materials are essential for surface plasmon to exist. This implies that one of the materials will be a metal. Some metals e.g.: Ag, Au, alkali metals, can be considered as (nearly) free electron systems. With sufficient free electrons the surface plasmon field intensity can be increased dramatically. Surface plasmon in these systems can be considered as propagating electron density waves occurring at the interface between the metal and the dielectric. When exposed to waves from an electromagnetic field the surface plasmon will oscillate in anti-phase with the electromagnetic field, Figure 1.5.

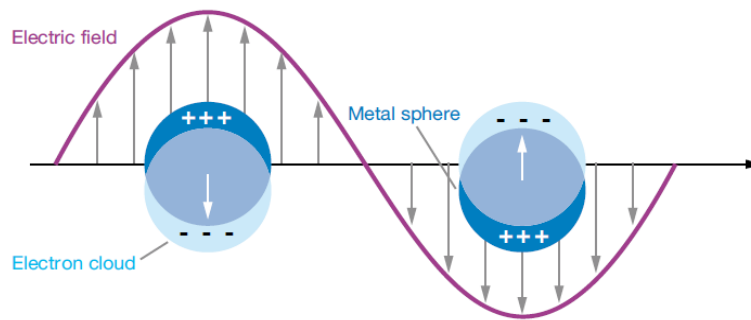


Figure 1.5 Schematic descriptions of electronic cloud displacements in nanoparticles under the effect of an electromagnetic wave. These oscillations give rise to so-called surface plasmon polariton resonances, more commonly referred to simply as SPRs, surface plasmon resonances. Taken from [25]

The signal observed from an electromagnetic wave interacting in this fashion decays exponentially with distance from the metal surface which is why a plasmon resonance localized at a surface is important in terms of the optical response from the surface. The position, shape and intensity of the surface plasmon resonance peak will depend upon several factors associated with the nanoparticles, namely: size, shape, monodispersity and dielectric constant of the material and the surrounding medium. The imaginary part of the dielectric constant increases with decreasing wavelength, and surface plasmon propagation decreases accordingly showing that the relationship relies on larger dielectric constants to work. This observation explains why despite the fact that surface plasmon resonances are theoretically possible for all materials, they are only actually observed in a few, selected materials. Silver shows better surface plasmon resonances due to larger real

part of its dielectric constant, though its disadvantage is that it is not as chemically inert in comparison to gold. A plasmon will propagate until it reaches an irregularity in the system, such as a roughened surface; at such a time the plasmon may be re-emitted as a photon. Recent years have seen a strong revival of interest in exploiting the properties of surface plasmon polaritons, motivated by the possibility that they offer for realizing a strong spatial confinement of electromagnetic fields. Optical devices capable of simultaneous measurement of the SPR spectrum and SERS spectrum will play an important role in future integrated nano-optical devices [48, 49].

1.4.3 Inverse Opals

As well as making photonic crystals from PMMA spheres, we also infill the spaces between the spheres with a variety of other materials in order to modify the periodic variation in refractive index that gives rise to the photonic band gap. An artificial opal made of PMMA spheres does not present a complete photonic band gap (cPBG), because to obtain a cPBG from an FCC structure of spheres embedded in a high dielectric constant material it would be necessary to ensure that the ratio between the embedding material and that of the spheres were above 2.8, which is not a practical reality. For this reason opals are usually regarded as templates to load with high RI material. They are used as an intermediate step to obtain a structure with cPBG. Inverse opal structures are being considered as relatively inexpensive photonic crystal materials with potential value. This research has involved monodisperse PMMA spheres as the building blocks for

Chapter 1

colloidal crystals, appropriate for producing inverse opals, which are inverse replicas of the original opals. Instead of consisting of regular arrangement of uniform spherical particles, inverse opals consist of a regular arrangements of uniform spherical voids surrounded by solid walls. Metallic inverse opals are made after deposition of the metal in the void spaces of the synthetic PMMA opals, and then removing the PMMA template by thermal processing, solvent extraction, or chemical etching. In the case of metal infilling, these materials also display novel plasmonic properties that are potentially useful for fabricating a range of novel devices, which extends to improved solar cells and surface enhanced Raman spectroscopy (see earlier). In some cases, particularly where we employ electro-deposition and co-crystallisation to infill periodic 3-D structures, we can remove the host spheres to produce an inverted photonic crystal or metallodielectric inverse opal (opal⁻¹). The approaches presently being employed for the integration of metals into PhCs are chemical vapour deposition (CVD) [50], atomic layer deposition (ALD) [51], dipping processes [52] and electrodeposition [53, 54]. However, these techniques have their own restrictions, such as the fact that the preliminary infiltration of a layer of metal nanoparticles may form a barrier to subsequent deposition, thus preventing complete metal infiltration. Electrodeposition is a potential alternative approach where the barrier formation can be avoided by depositing the metals from the bottom (substrate) to top (surface of the opal film). In another approach, we have employed a new route involving bottom-up co-crystallisation in order to prepare metallodielectric inverse opals (Figure 1.6). We designed the composite microporous

Chapter 1

metallic nanostructure using a combination of PMMA particles, hydrolyzed TEOS and Au nanoparticles. PMMA acts as the crystal template and colloidal gold nanoparticles 10-25 nm were then slowly deposited in the interstices of the PMMA crystals. Hydrolyzed TEOS works as a cementing component that holds the Au NPs together on the PhCs backbone. The PMMA crystal template was removed to form a silica gold inverse opal. It is demonstrated that the optical properties of the silica–gold composite inverse opals can be engineered by varying the type of nano metals and/or the nanoparticle volume-filling ratio of the composite. The use of metal nanoparticles to form inverse opals offers a versatile approach to prepare photonic materials that may exhibit absolute band-gaps. This method is a new route to fabricate metallodielectric inverse opals with high quality ordering, into large areas, which is more cost effective as compared to processes that have been reported so far, such as ALD and CVD [55]. Such materials may well lead to more well-developed or more complete photonic band gaps.

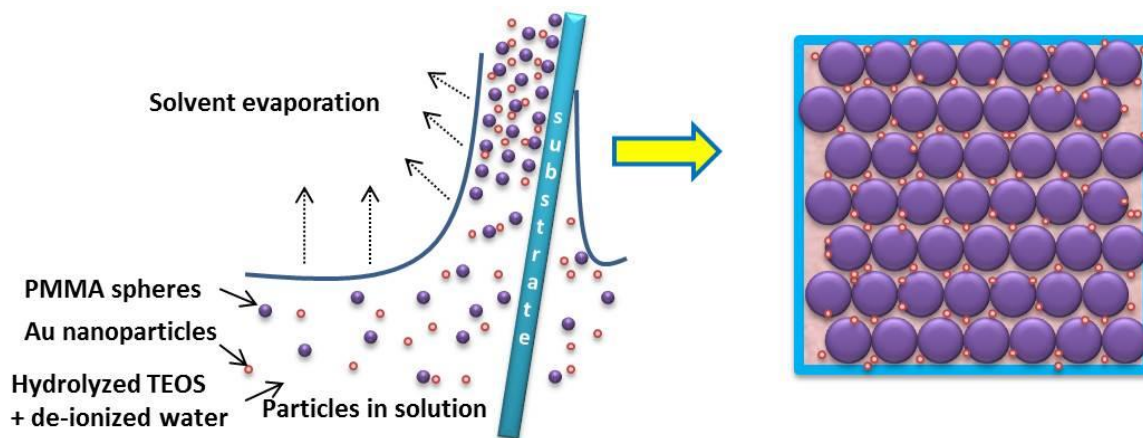


Figure 1.6 Bottom-up co-crystallisation process for the fabrication composite metallodielectric 3D-structure

1.4.4 Synthesis of Highly Monodisperse PMMA@Au Core-Shell Particles

Colloidal particles surrounded with metal nanoparticles (NPs) have recently attracted considerable attention due to their topological complexity and their unusual optical properties, often consequent from the motion of surface plasmon (polariton) resonances. Among those fabricated particles, core-shell (CS) or core-shell-shell (CSS)-type structures, with metal nanoparticles (gold, silver) are of particular interest, since they provide the possibility of employing metal NPs and manipulating their properties easily and simply [56-60]. In our case, based on previous research, we chose to study Au NPs due to their stability against chemicals while retaining their plasmonic properties [61]. Caruso and associates have proposed that the creation of thin silica shells on Au NPs enhances the Au NPs loading onto PS spheres when depositing them by a layer-by-layer (LBL) deposition process [62-66]. Yau *et al.* have studied single electron tunnelling

Chapter 1

through the silica shell of Au@SiO₂ in an effort to use them for electronic devices [67]. These core-shell materials may also be appropriate for engineering metallodielectric photonic crystals (MDPC) [68-72], providing a comparatively novel class of metamaterials, when they are prepared as monodisperse particles with smooth, round outer silica shells [73]. Here the term metamaterial has been coined to describe exactly-designed structures that have no analogues in nature. From previous studies in the literature it may be suggested that silica@Au core-shell constructions are less likely to form photonic crystal films [74]. This has then been the motivation behind our development of a process designed to form a concentric silica shell around the metal NPs as in the core-shell-shell (CSS) system. This should enable the establishment of a smooth and round outer silica@metal shell, making them more stable, and processable, for the formation of photonic crystal films. In this study we have focused on poly(methyl methacrylate) (PMMA) as a core material decorated with gold NPs. We demonstrate that our PMMA@Au core-shell particles are stable when immobilised into a photonic crystal film without any further encapsulating outer shell. Employing control over chemical reactions at the colloidal level has always been a challenge. With this in mind, various approaches have been employed to make dielectric@metal (Au or Ag) core-shell particles [74-80]. These will be discussed in Chapter 4. PMMA@Au composites are expected to have potential application in many technological areas such as surface-enhanced Raman spectroscopy (SERS), catalysis, biochemistry and solar cells.

1.5 Objectives

The main objectives of this research are:

- To synthesise monodispersed polymer spheres of PMMA and fabrication of colloidal crystals from synthesized PMMA.
- To demonstrate the potential of using various metals such as Ni, Au, deposited on PMMA colloidal crystal template via electrochemical processes and to generate metallodielectric inverse opals.
- To prepare PMMA@Au core-shell particles and explore their use as dielectric-coated metallic spheres for the creation of new PBG materials.
- To utilise the ‘co-crystallisation’ approach to make novel nanoparticle-loaded inverse opals.

References

1. Joannopoulos, J.D., Johnson, S.G., Winn, J.N. and Meade, R.D. *Photonic crystals - molding the flow of light*. Princeton: Princeton University Press, 2007.
2. Moroz, A. *Three-dimensional complete photonic-band-gap structures in the visible*. Physical Review Letters, 1999. **83**(25): p. 5274-5277.
3. Yablonovitch, E., Gmitter, T.J. and Leung, K.M. *Photonic band structure: The face-centered-cubic case employing nonspherical atoms*. Physical Review Letters, 1991. **67**(17): p. 2295-2298.
4. Ho, K.M., Chan, C.T. and Soukoulis, C.M. *Existence of a photonic gap in periodic dielectric structures*. Physical Review Letters, 1990. **65**(25): p. 3152-3155.
5. Liu, Z.-F., Zhang, G., Song, K., Clays, K. and Tung, C.-H. *Ternary inverse opal system for convenient and reversible photonic bandgap tuning*. Langmuir, 2008. **24**(18): p. 10519-10523.
6. Yablonovitch, E., *Inhibited spontaneous emission in solid-state physics and electronics*. Physical Review Letters, 1987. **58**(20): p. 2059-2062.
7. John, S., *Strong localization of photons in certain disordered dielectric superlattices*. Physical Review Letters, 1987. **58**(23): p. 2486-2489.
8. Joannopoulos, J.D., Villeneuve, P.R. and Fan, S.H. *Photonic crystals: Putting a new twist on light*. Nature, 1997. **386**(6621): p. 143-149.
9. Schrodén, R. and Balakrishnan, N. *Inverse opal photonic crystals a laboratory guide*. 2001, University of Minnesota. p. 1-32.

10. Fudouzi, H., *Optical properties caused by periodical array structure with colloidal particles and their applications*. Advanced Powder Technology, 2009. **20**(5): p. 502-508.
11. López, C., *Materials aspects of photonic crystals*. Advanced Materials, 2003. **15**: p. 1679-1704.
12. Jiang, P., Bertone, J.F., Hwang, K.S. and Colvin, V.L. *Single-crystal colloidal multilayers of controlled thickness*. Chemistry of Materials. 1999. **11**: p. 2132-2140.
13. Philipse, A.P., *Solid opaline packings of colloidal silica spheres*. J. Mater. Sci. Lett, 1989. **8**: p. 1371.
14. Blaaderen, A.V., Ruel, R. and Wiltzius, P. *Template directed colloidal Crystallization*. Nature, 1997. **385**: p. 321-324.
15. Vlasov, Y.A., Bo, X.-Z., Sturm, J.C. and Norris, D.J. *On-chip natural assembly of silicon photonic band gap crystals*. Nature (London), 2001. **414**: p. 289-293.
16. Park, S.H. and Xia, Y.N. *Assembly of mesoscale particles over large areas and its application in fabricating tunable optical filters*. Langmuir, 1999. **15**: p. 266-273.
17. Gu, Z.Z., Fujishima, A. and Sato, O. *Fabrication of high-quality opal films with controllable thickness*. Chemistry of Materials, 2002. **14**(2): p. 760-765.
18. Fudouzi, H., *Fabricating high-quality opal films with uniform structure over a large area*. Journal of Colloid and Interface Science, 2004. **275**(1): p. 277-283.

Chapter 1

19. Wang, A.-J., Chen S.L., Dong, P., Cai, X.G., Zhou, Q., Yuan, G.-M., Hu, C.-T. and Zhng, D.-Z. *Fabrication of colloidal photonic crystals with heterostructure by spin-coating method*. Chinese Physics Letters, 2009. **26**(2): p. 024210.
20. Jiang, X.C., Zeng, Q.H., Chena, C.Y. and Yu, A.B. *Self-assembly of particles: some thoughts and comments*. *Journal of Materials Chemistry*. 2011. **21**(42): p. 16797-16805.
21. Liu, Z., Jin, Z., Li, W., Qiu, J., Zhao, J. and Liu, X. *Synthesis of PS colloidal crystal templates and ordered ZnO porous thin films by dip-drawing method*. *Applied Surface Science*, 2006. **252**(14): p. 5002-5009.
22. Jiang, P., Sun, C.H., Linn, N.C., Ho, B.J. and Venkatesh, S. *Self-assembled photonic crystals and templated nanomaterials*. *Current Nanoscience*, 2007. **3**(4): p. 296-305.
23. Waterhouse, G.I.N. and Waterland, M.R. *Opal and inverse opal photonic crystals: Fabrication and characterization*. *Polyhedron*, 2007. **26**(2): p. 356-368.
24. Paquet, C. and Kumacheva, E. *Nanostructured polymers for photonics*. *Materials Today*, 2008. **11**(4): p. 48-56.
25. Willets, K.A. and Van Duyne, R.P. *Localized surface plasmon resonance spectroscopy and sensing*. 2007, *Annual Review of Physical Chemistry*. p. 267-297.
26. Romanov, S.G., Maka, T., Sotomayor Torres, C.M., Muller, M., Zentel, R., Cassagne, D., Manzanares-Martinez, J. and Jouanin, C. *Diffraction of light from thin-film polymethylmethacrylate opaline photonic crystals*. *Physical Review E*, 2001. **63**(5): p. 056603.

Chapter 1

27. Zhang, J., Sun, Z. and Yang, B. *Self-assembly of photonic crystals from polymer colloids*. Current Opinion in Colloid & Interface Science, 2009. **14**(2): p. 103-114.
28. Noda, S., Tormoda, K., Yamamoto, M. and Chutinan. *Full three-dimensional photonic bandgap crystals at near-infrared wavelengths*. Science, 2000. **289**(5479): p. 604-606.
29. Lin, S.Y., Fleming, J.G., Hetherington, D.L., Smith, B.K., Biswas, R., Ho, K.M., Sigalas, M.M., Zubrzycki, W., Kurtz, S.R. and Bur, J. *A three-dimensional photonic crystal operating at infrared wavelengths*. Nature, 1998. **394**(6690): p. 251-253.
30. Fleming, J.G. and Lin, S.Y. *Three-dimensional photonic crystal with a stop band from 1.35 to 1.95 μm* . Optics Letters, 1999. **24**(1): p. 49-51.
31. Aoki, K., Miyazaki, H.T., Hirayama, H., Inoshita, K., Baba, T., Shinya, N. and Aoyagi, Y. *Three-dimensional photonic crystals for optical wavelengths assembled by micromanipulation*. Applied Physics Letters, 2002. **81**(17): p. 3122-3124.
32. Campbell, M., Sharp, D.N., Harrison, M.T., Denning, R.G. and Turbefeild, A.J. *Fabrication of photonic crystals for the visible spectrum by holographic lithography*. Nature, 2000. **404**(6773): p. 53-56.
33. Sharp, D.N., Campbell, M., Dedman, E.R., Harrison, M.T., Denning, R.G. and Turbefeild, A.J. *Photonic crystals for the visible spectrum by holographic lithography*. Optical and Quantum Electronics, 2002. **34**(1-3): p. 3-12.
34. Ozin, G.A. and Yang, S.M. *The race for the photonic chip: Colloidal crystal assembly in silicon wafers*. Advanced Functional Materials, 2001. **11**(2): p. 95-104.

Chapter 1

35. Dimitrov, A.S. and Nagayama, K. *Continuous convective assembling of fine particles into two-dimensional arrays on solid surfaces*. Langmuir, 1996. **12**: p. 1303-1311.
36. Ye, J.H., Zentel, R., Arpiainen, S., Ahopelto, J., Jonsson, F., Romanov, S.G. and Sotomayor Torres, C.M. *Integration of self-assembled three-dimensional photonic crystals onto structured silicon wafers*. Langmuir, 2006. **22**(17): p. 7378-7383.
37. Khunsin, W., Kocher, G., Romanov, S.G., Sotomayor Torres, C.M. *Improving the opal-based photonic crystals by noise-assisted crystallization*. International Workshop and Conference on Photonics and Nanotechnology 2007, Proc. of SPIE Vol. **6793**, 67930B.
38. Li, Z.Y. and Zhang, Z.Q. *Fragility of photonic band gaps in inverse-opal photonic crystals*. Phys. Rev. Lett., 2000. **B 62**: p. 1516-1519.
39. Fleming, J.G., Lin, S.Y., El-Kady, I., Biswas, R. and Ho, K.M. *All-metallic three-dimensional photonic crystals with a large infrared bandgap*. Nature, 2002. **417**(6884): p. 52-55.
40. Sievenpiper, D.F., Sickmiller, M.E. and Yablonovitch, E. *3D wire mesh photonic crystals*. Phys. Rev. Lett. , 1996. **76**: p. 2480-2483.
41. McCalmont, J.S., Sigalas., M.M., Tuttle, G., Ho, K.-M. and Soukoulis, C.M. *A layer-by-layer metallic photonic band-gap structure*. Appl. Phys. Lett. , 1996. **68**: p. 2759-2761.

Chapter 1

42. Kitson, S.C., Barnes, W.L. and Sambles, J.R. *Full photonic band gap for surface modes in the visible*. Phys. Rev. Lett., 1996.**77**: p. 2670-2673.
43. Klar, T., Perner, M., Grosse, S., Von Plessen, G., Spirkl, W. and Feldmann, J. *Surface-plasmon resonances in single metallic nanoparticle*. Phys. Rev. Lett., 1998. **80**: p. 4249-4252
44. Chen, H.M., Pang, L., Kher, A. and Fainman, Y. *Three-dimensional composite metallodielectric nanostructure for enhanced surface plasmon resonance sensing*. Applied Physics Letters, 2009. **94**(7): p. 073117-3.
45. Wood, R.W., *XLII. On a remarkable case of uneven distribution of light in a diffraction grating spectrum*. 1902. **Vol. 4**(21).
46. Otto, A.Z. *Excitation of nonradiative surface plasma waves in silver by the method of frustrated total reflection*. Phys, 1968. **216**: p. 398-410.
47. Kretschmann, E. and Reather H. *Radioactive decay of non-radiative surface plasmon excited by light*. Z. Naturforsch. 1968. **23A**: p. 2135-2136.
48. Alvarez-Puebla, R.A., Dos Santos Jr, D.S. and Aroca, R.F. *Surface-enhanced Raman scattering for ultrasensitive chemical analysis of 1 and 2-naphthalenethiols*. Analyst, 2004. **129**(12): p. 1251-1256.
49. Moskovits, M., *Surface-enhanced Raman spectroscopy: a brief retrospective*. Journal of Raman Spectroscopy, 2005. **36**(6-7): p. 485-496.

Chapter 1

50. Zakhidov, A.A., Baughman, R.H., Iqbal, Z., Cui, C., Khayrullin, I., Dantas, S.O., Marti, J. and Ralchenko, V.G. *Carbon structures with three-dimensional periodicity at optical wavelengths*. Science, 1998. **282**(5390): p. 897-901.
51. Povey, I., Whitehead, D., Thomas, K., Pemble, M.E., Bardosova, M. and Renard, J. *Photonic crystal thin films of GaAs prepared by atomic layer deposition*. Applied physics letters, 2006. **89**(10): p. 104103-3.
52. Gu, Z.-Z., Chen, H., Zhang, S., Sun, L., Xie, Z. and Ge, Y. *Rapid synthesis of monodisperse polymer spheres for self-assembled photonic crystals*. Colloids and Surfaces A: Physicochemical and Engineering Aspects, 2007. **302**(1-3): p. 312-319.
53. Chung, Y.W., Fang, H.-S., Lee, J.H. and Tsai, C.J. *Fabrication of flexible thin film with pattern structure and macroporous array consisting of nanoparticles by electrophoretic deposition*. Jpn. J. Appl. Phys., 2010. **49**: p. 06GH11.
54. Kassim, S., Padmanabhan, S.C., Salaun, M. and Pemble, M.E. *PMMA-gold metallodielectric photonic crystals and inverse opals: preparation and optical properties*. AIP Conference Proceedings, 2011. **1391**(1): p. 263-265.
55. Padmanabhan, S., Linehan, K., O'Brien, S., Kassim, S., Doyle, H., Povey, I., Schmidt, M. and Pemble, M.E. *A bottom-up fabrication method for the production of visible light active photonic crystals*. Journal of Materials Chemistry C, 2014.**2**(9): p. 1675-1682
56. Liz-Marzán, L.M., Giersig, M. and Mulvaney, P. *Synthesis of nanosized gold-silica core-shell particles*. Langmuir, 1996. **12**: p. 4329-4335.

Chapter 1

57. Rosemary, M.J., MacLaren, I. and Pradeep, T. *Investigations of the antibacterial properties of ciprofloxacin@SiO₂*. Langmuir, 2006. **22**: p. 10125-10129.
58. Mongin, D., Juvé, V., Maioli, P., Crut, A., Fatti, N.D. and Vallée, F. *Acoustic vibrations of metal-dielectric core-shell nanoparticles*. Nano Lett. , 2011. **11**: p. 3016-3021.
59. Lekeufack, D.D., Brioude, A., Mouti, A., Alauzun, J.G., Stadelmann, P., Coleman, A.W. and Miele, P. *Core-shell Au@(TiO₂, SiO₂) nanoparticles with tunable morphology*. Chem. Commun. , 2010. **46**: p. 4544-4546
60. Asefa, T., Duncanc, C.T. and Sharma, K.K. *Recent advances in nanostructured chemosensors and biosensors*. Analyst, 2009. **134**: p. 1980-1990.
61. Kandimalla, V.K., *Influence of metal nanoparticles on fluorescence properties*, (Master's thesis) in *Department of Chemistry*. 2010, Eastern Michigan University: Ypsilanti, Michigan.
62. Caruso, F., Spasova, M., Salgueiriño-Maceira, V. and Liz-Marzán, L.M. *Multilayer assemblies of silica-encapsulated gold nanoparticles on decomposable colloid templates*. Adv. Mater., 2001. **13**: p. 1090 - 1094.
63. Caruso, F., Caruso, R.A. and Möhwald, H. *Production of hollow microspheres from nanostructured composite particles*. Chem. Mater., 1999. **11**: p. 3309–3314.
64. Caruso, R.A., Susha, A. and Caruso, F. *Multilayered titania, silica, and laponite nanoparticle coatings on polystyrene colloidal templates and resulting inorganic hollow spheres*. Chem. Mater. , 2001 **13**: p. 400–409.

Chapter 1

65. Wang, Y., Angelatos, A.S. and Caruso, F. *Template synthesis of nanostructured materials via layer-by-layer assembly*. Chem. Mater., 2008 **20**: p. 848–858.
66. Yan, Y., Such, G.K., Johnston, A.P.R., Lomas, H. and Caruso, F. *Toward therapeutic delivery with layer-by-layer engineered particles*. ACS Nano, 2011. **5**: p. 4252–4257.
67. Yau, S.-T., Mulvaney, P., Xu, W. and Spinks, G.M. *Nonlinear single-electron tunneling through individually coated colloid particles at room temperature*. Phys. Rev. B, 1998. **57**: p. R15124.
68. Wang, D., Salgueiriño-Maceira, V., Liz-Marzán, L.M. and Caruso, F. *Gold-silica inverse opals by colloidal crystal templating*. Adv. Mater., 2002. **14**: p. 908-912.
69. Lu, Y., Yin, Y., Li, Z.-Y. and Xia, Y. *Synthesis and self-assembly of Au@SiO₂ core-shell colloids*. Nano Lett., 2002. **2**: p. 785-788.
70. Liang, Z., Susha, A.S. and Caruso, F. *Metallodielectric opals of layer-by-layer processed coated colloids*. Adv. Mater., 2002. **14**: p. 1160-1164.
71. Liang, Z., Susha, A. and Caruso, F. *Gold nanoparticle-based core-shell and hollow spheres and ordered assemblies thereof*. Chem. Mater. , 2003. **15**: p. 3176-3183.
72. Wang, D., Li, J., Chan, C.T., Salgueiriño-Maceira, V., Liz-Marzán L.M., Romanov, S. and Caruso, F. *Optical properties of nanoparticle-based metallodielectric inverse opals*. Small, 2005. **1**: p. 122-130.
73. Padmanabhan, S.C., McGrath, J., Bardosova, M. and Pemble, M.E. *A facile method for the synthesis of highly monodisperse silica@gold@silica core-shell-shell particles*

Chapter 1

- and their use in the fabrication of three-dimensional metallodielectric photonic crystals.* Journal of Materials Chemistry, 2012. **22**(24): p. 11978-11987.
74. Pastoriza-Santos, I. and Liz-Marzán, L.M. *Binary cooperative complementary nanoscale interfacial materials. Reduction of silver nanoparticles in DMF. Formation of monolayers and stable colloids.* Pure Appl. Chem., 2000. **72**: p. 83-90.
75. Pastoriza-Santos, I. and Liz-Marzán, L.M. *Formation and stabilization of silver nanoparticles through reduction by N,N-dimethylformamide.* Langmuir 1999. **15**: p. 948-951.
76. Graf, C., Dembski, S., Hofmann, A. and Rühl, E. *A general method for the controlled embedding of nanoparticles in silica colloids.* Langmuir, 2006.**22**: p. 5604-5610.
77. Shi, Y.-L. and Asefa, T. *Tailored core-shell-shell nanostructures: Sandwiching gold nanoparticles between silica cores and tunable silica shells.* Langmuir, 2007. **23**: p. 9455-9462.
78. Chen, Z., Wang, Z.L., Zhan, P., Zhang, J.H., Zhang, W.Y., Wang, H.T. and Ming, N.B., *Preparation of metallodielectric composite particles with multishell structure.* Langmuir, 2004, **20**: 3042–3046.
79. Xu, S., Hartvickson, S. and Zhao, J.X. *Engineering of SiO₂-Au-SiO₂ sandwich nanoaggregates using a building block: single, double and triple cores for enhancement of near infrared fluorescence.* Langmuir, 2008, **24**(14), 7492-7499.

Chapter 1

80. Wang, T., Shi, S., Akiyama, Y., Zhaou, L.M. and Kuroda, S. *Chemically immobilizing gold nanoparticles to the surface of polystyrene particles*. Journal of Materials Science, 2010. **45**(16): p. 4539-4542.

Chapter 2: Experimental Techniques

2.1 Materials

Methyl methacrylate (MMA) monomer and potassium persulfate (KPS) were purchased from Sigma Aldrich and used as supplied for the synthesis of PMMA spheres. Polyethyleneimine (PEI), poly(sodium 4-styrene sulfonate) (PSSS, MW ca. 70, 000 Da), sodium borohydrate (NaBH_4) and chloroauric acid, (HAuCl_4) were purchased from Sigma Aldrich and used as supplied for the synthesis PMMA@Au core shell. Ultrapure water (18.2 M Ω cm) was used directly from a Millipore water system as a medium of reaction, for cleaning substrates and for film fabrication. Standard glass microscope slides were cut to required sizes and used as substrates. Sulphuric acid (95-98%), ammonium hydroxide (25%), hydrogen peroxide (30%), were purchased from Sigma-Aldrich, and used as received without further purification. Prior to rendering hydrophilic, substrates were ultrasonically cleaned in ethanol for 5 minutes, which also helped remove dirt and particulates from the cutting process.

2.2 Synthesis of Monodisperse PMMA Colloidal Spheres

PMMA colloidal particles, 373 nm (relative standard deviation <5%) were prepared by an emulsifier-free emulsion polymerisation reaction in a water-based system in the presence of an initiator, potassium persulfate. Specifically, ultrapure water was bubbled with nitrogen gas for 20 minutes. After this, 15 ml MMA was added under nitrogen atmosphere and rapid stirring, followed by the potassium persulfate. The solution was heated to 80°C and maintained at this temperature for 40 minutes. After the polymerisation reaction, the colloid was centrifuged and washed in ultrapure water 5-6 times. The apparatus for the preparation of monodisperse PMMA spheres is illustrated in Figure 2.1. The synthesis is summarised schematically in Figure 2.2. The procedure was repeated as necessary in order to investigate the influence of various parameters such as, concentration of monomer and initiator, temperature, and time of polymerisation, on the PMMA sphere size.

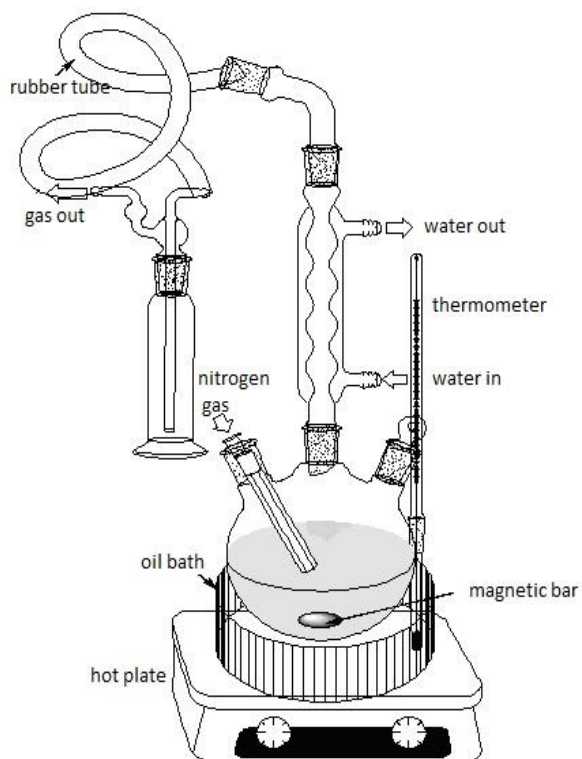


Figure 2.1 A schematic diagram showing the set-up of the polymerisation apparatus. A 3-neck round-bottom flask was used to attach a nitrogen line and water cooling, while the remaining neck, which was covered by a stopper during the reaction, was used for the addition of reagents.

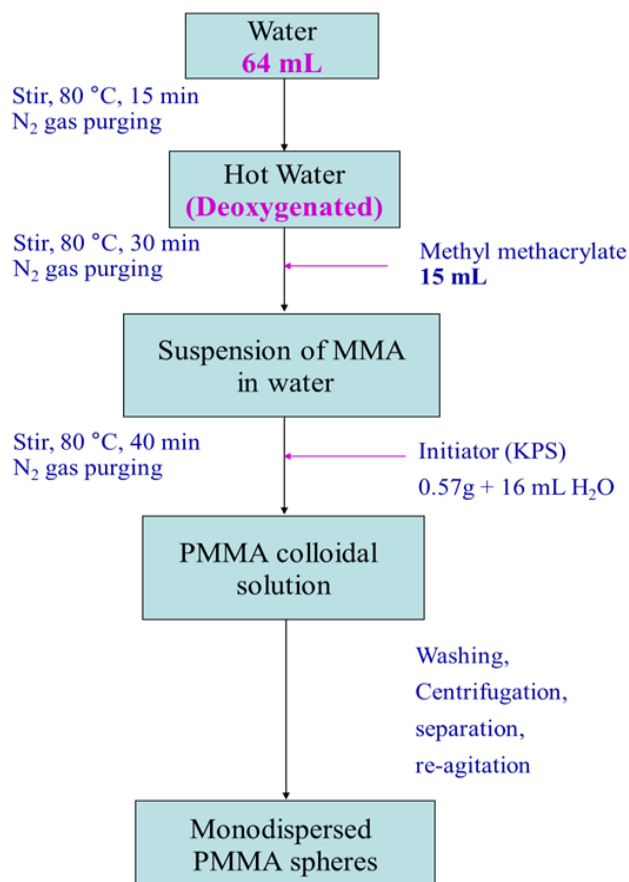


Figure 2.2 A schematic diagram of the process employed in order to synthesis colloidal PMMA

2.3 Substrates Cleaning

All substrates were cleaned with a mixture of water, ammonium hydroxide and hydrogen peroxide with volume ratio 5:1:1 respectively for 1 hour, or by piranha solution (a mixture of sulphuric acid and hydrogen peroxide with volume ratio 3:1) followed by rinsing in pure water and drying under nitrogen. The piranha mixture is a strong oxidizing agent and will remove most organic matter and also hydroxylate most surfaces (add OH groups) making them more hydrophilic.

2.4 Self-Assembly Evaporation Experimental

Since its introduction in 1999 by Jiang *et al.* [1] the controlled evaporation deposition (or vertical deposition or convective assembly) method has become the most widespread self-assembly technique to fabricate opaline 3D photonic crystals. It is based on the convective self-assembly of colloids on a substrate by the action of a moving meniscus.

In a typical experimental set up, a known concentration of PMMA colloidal particles was re-dispersed in water, with varying concentrations from 0.05 to 0.25 volume %, in 24mm diameter vials. Then, a cleaned substrate was settled in the PMMA suspension with a tilt angle of approx. 60° and placed into an oven at 65°C for 2-3 days (Figure 2.3). Solvent flow towards the meniscus region due to evaporation (which is highest in the meniscus region), drags spheres from the suspension and these are incorporated into an ordered face centered cubic (FCC) structure [2, 3]. Therefore the optimal conditions for the growth of a film with good crystalline order include an optimum evaporation rate which allows for good ordering of the particles, as well as the presence of a reservoir of particles in the suspension to be incorporated into the ordered region. All films deposited in this manner exhibited brilliant colours that changed as the angle of observation changed as shown in Figure 2.4.

Other parameters which are known to influence the growth of samples by the vertical deposition method are the diameter and concentration of the colloids, which are known to determine the thickness of the samples, and relative humidity. In general, higher

Chapter 2

concentrations and smaller diameter colloids yield samples with a larger number of layers. It should be noted that these parameters are not independent from one another, and hence optimum values for each parameter may be different for different particle sizes [4].

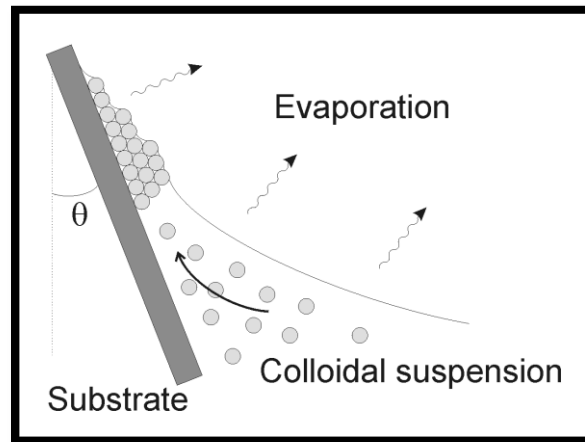


Figure 2.3 A schematic of the vertical deposition method. A substrate is placed in a colloidal suspension. The substrate is inclined at an angle θ . Ordering of the spheres takes place at the meniscus. Taken from [1].

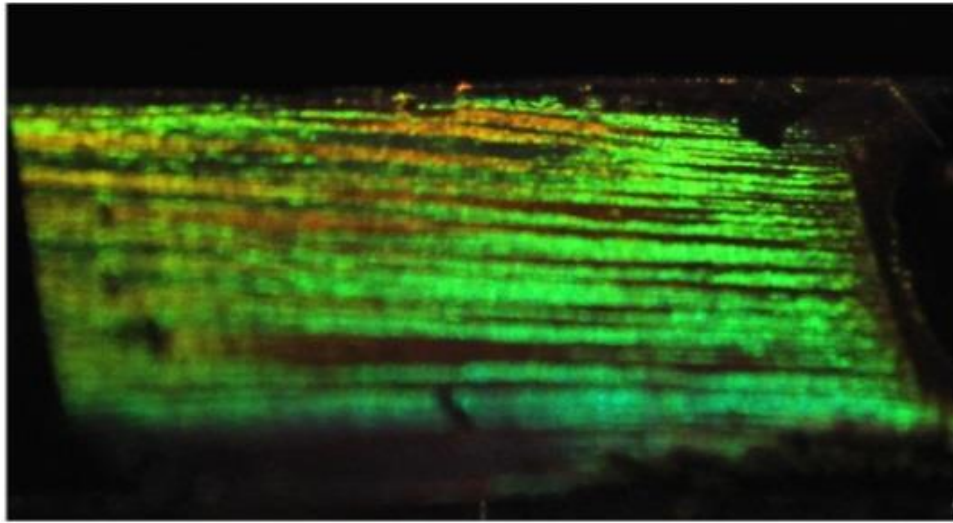


Figure 2.4 A photograph of opaline polymer film formed on a glass substrate (1cm x 2.5cm).

To smooth out temperature fluctuations inside the oven during deposition of the particles, and hence maintain a constant rate of evaporation, an aluminium block was introduced as a dry bath heat sink. The aluminium block was thermally stabilised in the oven for a minimum of 4 hours before deposition samples were inserted into the drilled holes, Figure 2.5.



Figure 2.5 A photograph of the aluminium block used to stabilise sample temperature during controlled evaporation

2.5 Dip Coating

A second method for producing high quality colloidal photonic crystal templates is the dip coating process [5]. A colloidal PMMA suspension was sonicated for 30 minutes in order to break up any agglomerated particles before use. A cleaned glass or ITO/gold substrate (conductive substrate for electrodeposition) was then settled vertically into the PMMA suspension (2%) and slowly drawn out at a rate of 0.1 mm h^{-1} . The prepared template was then heated overnight in the oven at 70°C to enhance the adhesion of particles to substrate before electrodeposition. As reported in the literature [5], it was found that it was possible to control film thickness by either changing the particle concentration or the lifting speed (Figure 2.6).

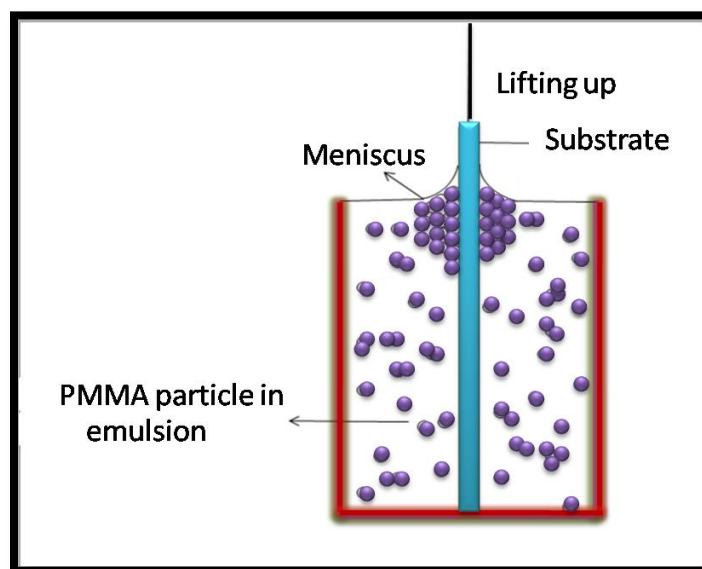


Figure 2.6 A schematic representation of the dip coating process

2.6 Synthesis of PMMA@Au Core-Shell Particles

Au nanoparticles (NP) were incorporated onto the surface of PMMA spheres in the presence of polyethyleneimine (PEI) employed as a linker agent. PMMA spheres were synthesized as described in section 2.3. The synthesized spheres (10 mL of 4% suspension) and 50 mL of PEI were added into 1500 ml ultrapure water and stirred for 1 day. The mixture of PEI-decorated PMMA spheres were then centrifuged and re-dispersed with de-ionized water. This procedure was repeated 5-6 times and finally the particles were again re-dispersed in water and stirred. The Au nanoparticles used for the experiment were prepared separately using a NaBH_4 reduction method. In order to prepare Au nanoparticles, 5 mL trisodium citrate dihydrate ($\text{Na}_3\text{C}_6\text{H}_5\text{O}_7$, TSC), 0.3 mL poly(sodium 4-styrene sulfonate) (PSSS, MW ca. 70, 000 Da) and 0.3 mL NaBH_4 were added into a beaker containing 500 mL ultrapure water. 5 ml HAuCl_4 (50 wt. % in water,

5 mM) was then added into this dropwise at a rate of 2 mlmin^{-1} while stirring. 3 mL TSC was added into the Au nanoparticle sol immediately after the addition of Au precursor and the mixture stirred for 1 min. After 1 min, the PEI-modified PMMA particles were added into the Au sol dropwise under stirring. The colloid was then stirred for further 2 h and then washed and centrifuged at least 5 times.

2.7 Electrochemical Deposition of Gold and Nickel into PMMA Photonic Crystal Templates

Infilling of gold and nickel into a PMMA template was performed electrochemically using a standard 3-electrode cell and a potentiostat (model CHI 660B), respectively [6]. The commercial aqueous gold solution was bought from AMI DODUCO and used as supplied. The aqueous solution used for Ni deposition [6] was composed of NiSO_4 (2.13 M), NiCl_2 (0.35 M) and H_3BO_3 (0.43 M). The working electrode was a conductive ITO substrate (for gold filling) or Au substrate (for nickel filling) with a PMMA colloidal photonic crystal film deposited on it, respectively. A carbon rod and silver/silver chloride were used as the counter and reference electrodes, respectively. The extent of gold and nickel deposition was optimised against the current-time transient in order to obtain gold/nickel deposition into all the available voids. Inverse opals were then prepared by a combination of solvent extraction (acetone) of the PMMA spheres, and calcination (350-400°C).

2.8 Co-Crystallisation of Silica Sol/Au NPs/PMMA and the Subsequent Inverted Structure

The inverse opal MDPC was prepared by the controlled evaporation self-assembly of an aqueous colloidal suspension containing PMMA spheres, partially-hydrolysed silicate precursor – tetraethyl orthosilicate (TEOS) – and Au nanoparticles (NPs) followed by the chemical dissolution of the PMMA template. The PMMA spheres of ~373 nm diameter were synthesized by a surfactant free emulsion reaction as described in section 2.2. The Au NPs were prepared by NaBH₄ reduction in presence of citrate functionality as reported in section 2.6. The citrate functionalization was added in order to make the Au NPs (~14nm) compatible with the colloidal suspension. An acid hydrolysed TEOS solution was then prepared separately and added to the suspension. The addition of TEOS was important as it works as the cementing component that holds the Au NPs to the photonic crystal backbone. The precursor TEOS solution used ethanol:HCl (0.1M):TEOS in a ratio of 8:1:1; respectively. The PMMA photonic crystal templates were removed with acetone, and by further calcining the sample at 350-400°C, in order to form the silica/gold inverse opal.

2.9 Co-Crystallisation of Silica Sol/PMMA and the Subsequent Silica Inverted Structure

Silica inverse opals were prepared as in section 2.9 but without the presence of the Au NPs, for comparison purposes.

2.10 Instrumentation and Characterisation

2.10.1 Optical Characterisation

Optical characterisation was performed using a Mikropack halogen HL2000 white light source, with a focussed spot size at the sample of approx. 1.5mm diameter. The transmitted or reflected light was collected via an optical fibre and directed into an Ocean Optics HR4000 spectrometer equipped with a detector suitable for wavelengths in the UV-visible range (Figure 2.7). Spectral analysis was performed using Ocean Optics software Spectra Suite. For angle resolved reflectance measurements, the sample, the 2nd focussing lens and detector lens were rotated around the axis of the sample to various reflectance angles from a minimum of 10° to a maximum of 80°, while for transmission measurements, only the sample itself was rotated. In both the reflectance (R) and transmittance (T) mode the baseline correction was done with a bare glass substrate to eliminate the effects such as light reflection at the air-glass interface and substrate absorption, if any.

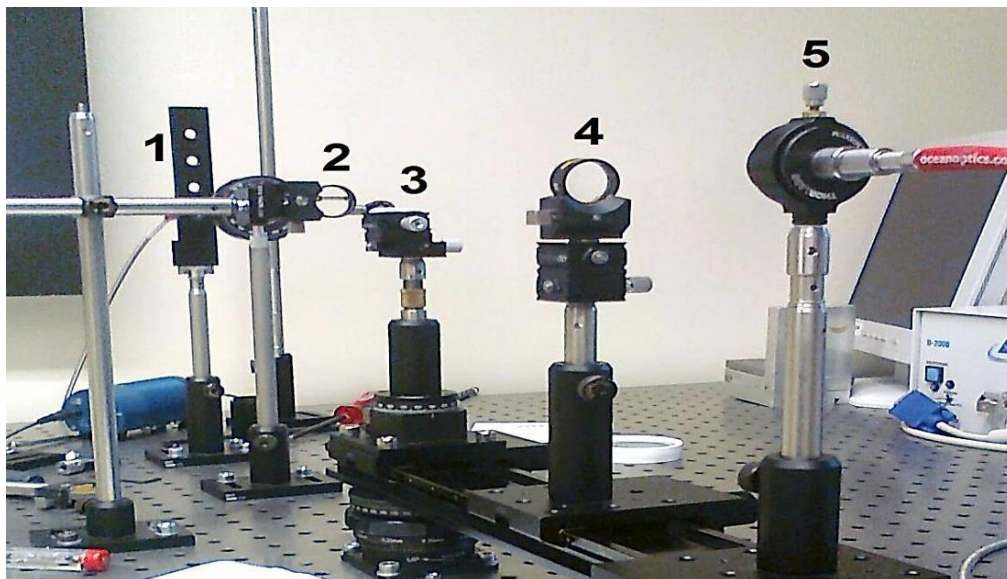


Figure 2.7 A photograph showing the optical set up used for determination of the spectral data; (1) light source, (2) focussing lens, (3) sample holder, (4) 2nd focussing lens, and (5) detector lens.

2.10.2 Scanning Electron Microscope (SEM)

High magnification images were acquired using a high resolution scanning electron microscope (HRSEM, Quanta FEG 650, FEI company). For the SEM investigations, specimens were gold-sputtered prior to examination in order to minimise charging effects.

2.10.3 Transmission Electron Microscope (TEM)

Transmission Electron Microscopy (TEM) images were acquired using a JEOL 2100 electron microscope operating at 200 KV and equipped with a LAB₆ electron source. TEM samples were prepared by depositing a number of aliquots of the silicon

nanocrystal dispersion, 300 μL in total, onto a carbon coated TEM grid. The solvent was allowed to evaporate completely between successive depositions.

2.10.4 UV Visible Absorption Spectroscopy

The UV-visible absorption spectra were measured with an Agilent Technologies 8453 Spectrophotometer using 1 cm path length quartz cells.

2.10.5 Zeta Potential

ζ -potential measurements were performed using a Nano ZS Malvern Zetasizer. ζ -potential is related to the surface charge, a property that all materials possess, or acquire, when suspended in a fluid. It can therefore be used to indicate the stability of colloidal dispersions.

2.10.6 Raman Spectroscopy

The Raman spectra were recorded using an InVia Renishaw Raman microscope operating at room temperature. An argon ion laser operating at 514 nm was used to obtain the Raman spectrum of the metallodielectric photonic crystal, which was then compared to the Raman spectrum from a bare PMMA PhC. Typically the system was operated using a spot size of 1 μm , at a power of 5mW, with signal acquisition times of 30 s.

References

1. Jiang, P., Bertone, J.F., Hwang, K.S., and Colvin, V.L. *Single-crystal colloidal multilayers of controlled thickness*. *Chemistry of Materials*, 1999. **11**: p. 2132-2140.
2. Norris, D.J., Arlinghaus, E.G., Meng, L., Heiny, R. and Scriven, L.E. *Opaline photonic crystals: How does self-assembly work?* *Advanced Materials*, 2004. **16**(16): p. 1393-1399.
3. Brewer, D.D., Allen, J., Miller, M.R., de Santos, J.M., Kumar, S., Norris, D.J., Tsapatsis, M. and Scriven, L.E. *Mechanistic principles of colloidal crystal growth by evaporation-induced convective steering*. *Langmuir*, 2008. **24**(23): p. 13683-13693.
4. Kuai, S.L., Hu, X.F., Hache, A. and Truong, V.V. *High-quality colloidal photonic crystals obtained by optimizing growth parameters in a vertical deposition technique*. *Journal of Crystal Growth*, 2004. **267**(1-2): p. 317-324.
5. Gu, Z.Z., Fujishima, A. and Sato, O. *Rapid synthesis of monodisperse polymer spheres for self-assembled photonic crystals*. *Colloids and Surfaces A: Physicochemical and Engineering Aspects*, 2007. **302**(1-3): p. 312-319.
6. Chung, Y.-W. Ing-Che, L., Jian-hang, L., Jung-Hsien, Y. and Ming-Hsiung, H. *Fabrication of various nickel nanostructures by manipulating the one-step electrodeposition process*. *Journal of The Electrochemical Society*, 2007. **154**(6): p. E77-E83.

Chapter 3: Synthesis of Poly(methyl methacrylate) Spheres

3.1 Introduction

Colloidal crystallisation of monodisperse spherical particles has been widely used in the fabrication of artificial photonic crystals [1]. The monodispersity of the colloidal spheres is important in this research field, as these are the basic elements for the bottom-up construction of PhCs, where the size distribution of the spheres can greatly affect the optical properties [1, 2]. Among the materials used for colloidal crystal, the most widely used are silica and polymers [1, 3-5]. Owing to a higher surface charge to density ratio, polymer particles generally produce high quality PhCs more easily than silica particles [6]. Monodisperse polymer colloids, mainly poly(methyl methacrylate) (PMMA) and polystyrene (PS) microspheres have been prepared by modified emulsion polymerisation [7]. There are many advantages to using polymer colloids as building blocks for the construction of colloidal crystals, including multiple choices of chemical composition, tuneable particle size and low cost [2]. In addition, they are easily removed by solvent

dissolution or thermal calcinations, when acting as templates for macroporous materials and inverse opals. The ease of synthesis of PMMA compared to PS colloids led to their use in this study. Among the advantages for preparing PMMA particles shorter reaction times (40 minutes) and the high degree of monodispersity of the particles which can be obtained.

3.2 Synthesis of Monodisperse PMMA Spheres

In this study, uniformly sized PMMA spheres were prepared by a modified emulsifier-free polymerisation in water, which is more environmental friendly compared to other methods that use solvents such as toluene as the medium of reaction [8]. Several studies have been conducted on the polymerisation of MMA in the absence of an emulsifier agent to produce highly monodisperse particles [1, 7]. This is in contrast to the emulsifier-free polymerisation of styrene, where there is a considerable body of work [3]. Tanniseer *et al.* [9] reported the synthesis of PMMA using potassium persulfate as an initiator and their study on various parameters. In this study they highlight the parameters of interest, such as, reaction temperature, total reaction time, stirring speed, monomer and initiator concentrations. Their polymerisation reaction time took 2 hours to complete, which is three times longer than in this study. Despite a relatively low polydispersity of 1.42%, when we compare their SEM images of PMMA particles (Figure 3.1) to those produced in this study, the particles made by Tanniseer *et al.* do not appear to be as regularly monodisperse as those produced during this study, as shown in Figure 3.6.

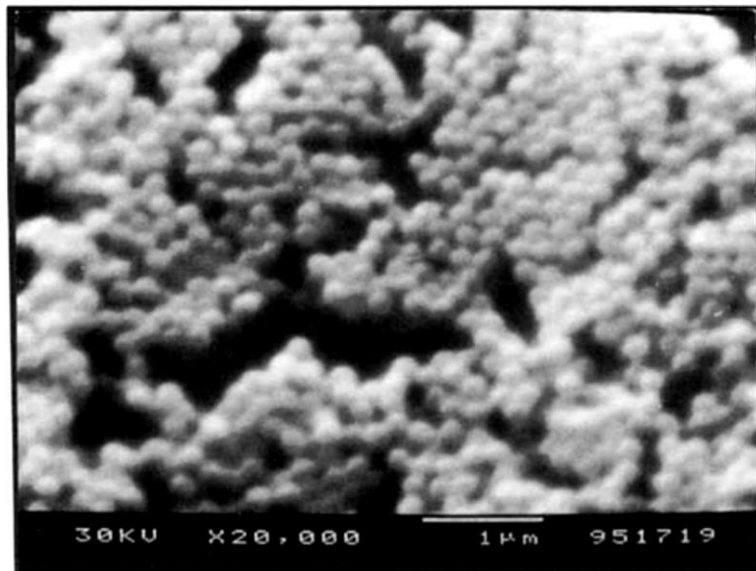
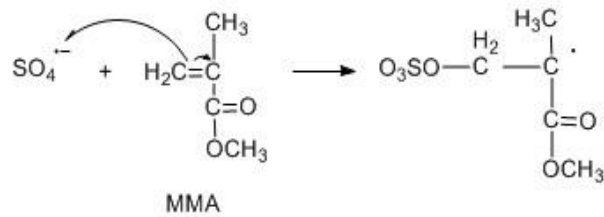


Figure 3.1 PMMA beads prepared by emulsifier-free polymerisation of MMA in the presence of potassium persulfate at 75°C for 2 hours. Taken from [9]

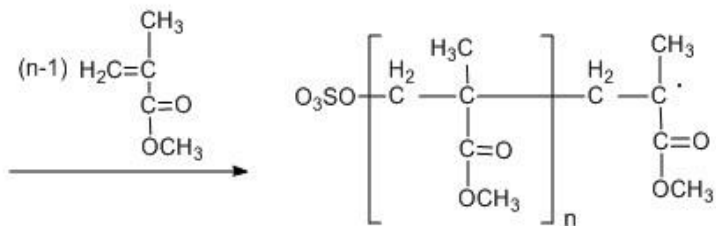
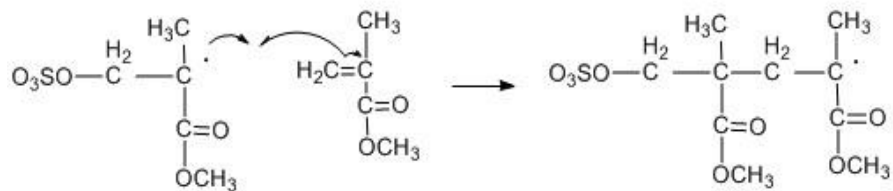
The initiator used in our experiment is potassium persulfate (KPS) which decomposes with heat to produce a free radical initiator for the polymerisation reaction. There are three stages of polymerisation: initiation, propagation and termination. These stages are illustrated in Figure 3.2 for the synthesis of PMMA spheres. In the initiation stage, when an aqueous solution of persulfate is heated, it decomposes to generate sulfate ion radicals, which subsequently add to the double bond of the MMA monomer. Once initiated, successive addition of MMA monomers to the free radical end of the polymer chain causes the chain to grow (propagation stage). In each step the consumption of a free radical is accompanied by the formation of a new, larger free radical. Eventually, in the termination stage, the polymerisation stops by reaction which consumes, but do not form, free radicals, such as the combination of two free radicals.

Chapter 3

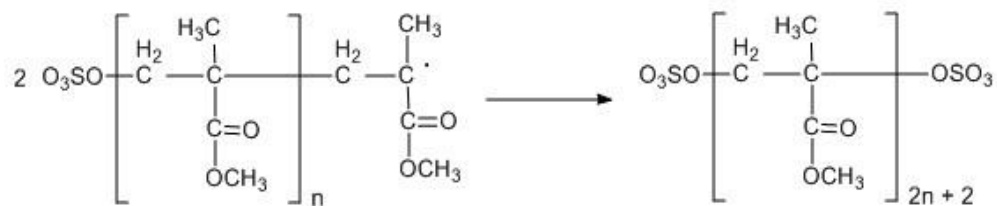
Initiation



Propagation



Termination



PMMA

Figure 3.2 The scheme shows a reaction mechanism of free radical chain-growth polymerisation of MMA using the potassium persulfate including initiation, propagation and termination. (Taken from Ref. [10] which uses different initiator)

Chapter 3

As part of this study we established the optimum conditions for the emulsifier-free polymerisation of MMA. The parameters concerned are similar to those reported previously [1] albeit with slightly different concentrations of initiator and monomer, smaller overall reaction volumes and somewhat higher temperatures. In this synthesis the reaction conditions, monomer and initiator concentrations, and temperature, are key factors influencing sphere size, monodispersity and polymerisation efficiency. In order to synthesise monodisperse spheres with a narrow size dispersity and good repeatability, precise control over all of these conditions is necessary [11]. For the synthesis of monodisperse spheres, the temperature is a critical factor. A uniform reaction temperature throughout the entire process is necessary to ensure spheres are produced with a narrow size distribution. Therefore, a precise temperature controller is generally necessary as a part of the synthesis apparatus. In addition, the solution should be stirred vigorously to ensure the temperature distribution is homogeneous, because the polymerisation is an exothermic reaction, which can raise the localized temperature of the solvent. Another critical component in the polymerisation process is to use an inert atmosphere. Molecular oxygen can capture free radicals during the polymerisation, preventing free-radical chain propagation. Therefore, oxygen needs to be completely removed from the reaction system.

PMMA spheres of a number of different average sizes, from 290 to 763 nm were produced by either changing the monomer concentration (Figure 3.3), or changing the reaction temperature (Figure 3.4). Other parameters, such as amount of initiator, water volume and reaction time were kept constant. In Figure 3.3, smaller spheres were

Chapter 3

obtained by using less MMA. Increasing the amount of monomer MMA from 5 to 25ml, increased the size of the spheres produced. Aggregation of the spheres occurred when the volume of monomer employed exceeded 25ml. This is likely to be due to a viscosity effect, as the volume of water was held constant during these experiments.

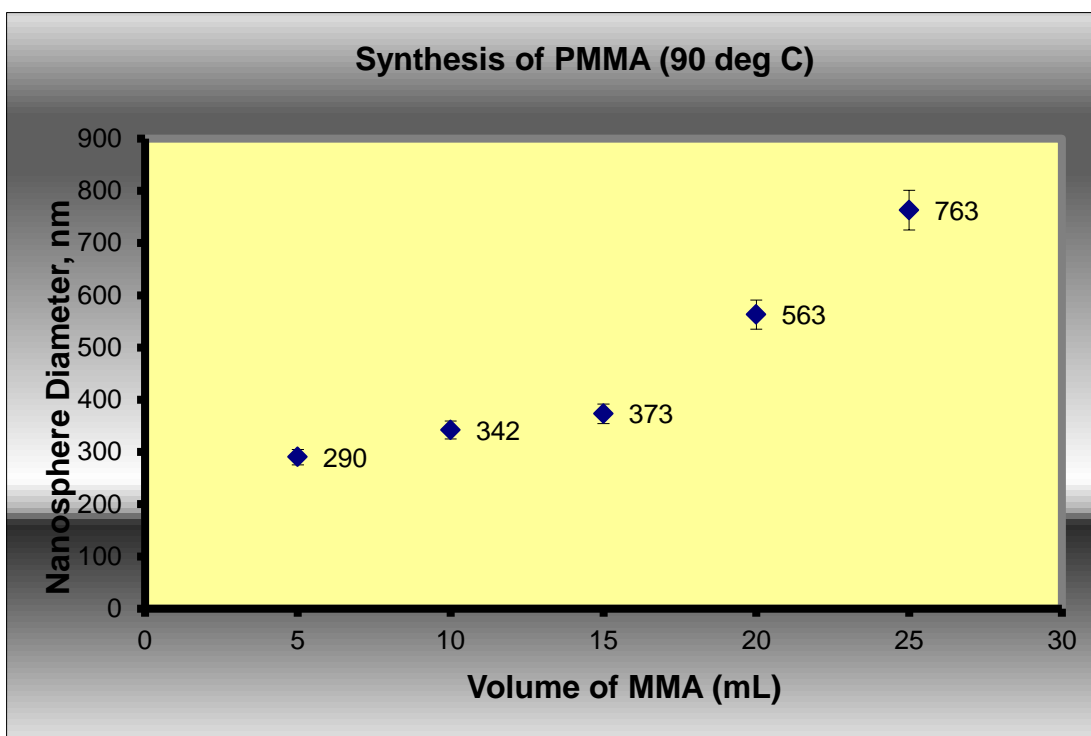


Figure 3.3 Showing varying PMMA sphere sizes with volume addition of MMA monomer at a reaction temperature of 90°C

Spheres produced from 15 ml MMA monomer at 90°C (diameter size 373nm) exhibited the highest uniformity of diameters, as shown in Figure 3.6 compared to the other samples. From this optimum volume addition, the effect of varying reaction temperature on particles size was also investigated. As can be seen in Figure 3.4, a decrease in the

Chapter 3

diameter of the spheres was achieved by increasing the temperature of the system. This effect arises from the fact that higher temperatures enhance the reactivity of the initiator, which simultaneously initiates more polymerisation sites. As a result, there are more nuclei for polymer chain propagation and sphere growth when the synthesis is performed at the higher temperatures. In this case, when the amount of monomer is fixed, the final size of the spheres decreases with the initial number of nuclei. This study confirms the work of Tanriseer *et al.* in 1996 [9] where they expected the initial rate of polymerisation to increase with increasing temperature.

At 70°C it was found that 40 minutes was insufficient time for the reaction to go to completion. Unreacted monomer formed a visible oily residue in the reaction vessel, and it is therefore likely that a longer reaction time is required at this lower temperature.

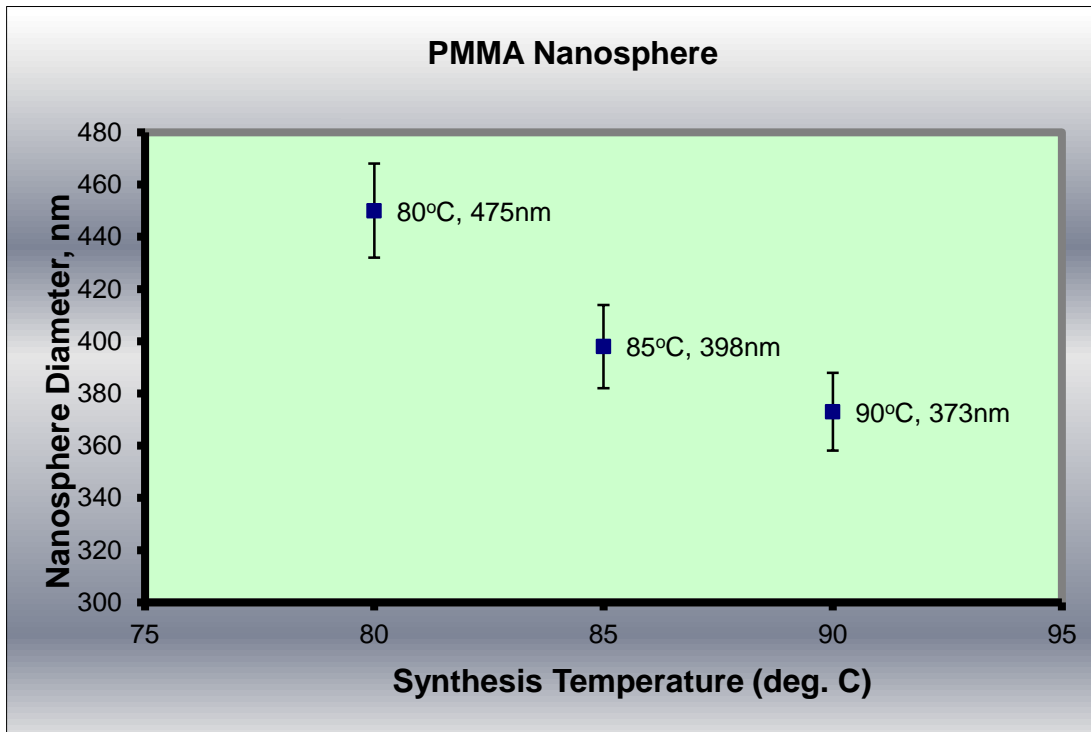


Figure 3.4 Showing varying PMMA sphere sizes with reaction temperature

The Arrhenius equation gives the quantitative basis of the relationship between the activation energy (E_a) and the rate at which a reaction proceeds.

$$\text{Diameter} \equiv 1/\text{Rate of reaction}$$

Which can be rewritten as $1/\text{Diameter} \propto k$

OR as $\ln(1/\text{Diameter}) \propto \ln k$

From the Arrhenius equation, the activation energy can be expressed as:

$$k = Ae^{-E_a/RT}$$

Chapter 3

Then,
$$\ln k = \ln A - \frac{E_a}{RT}$$

By plotting $\ln k$ vs. $\frac{1}{T}$; slope $\approx -\frac{E_a}{R}$

i.e. $\ln(1/\text{Diameter})$ vs. $\frac{1}{T}$

where A is the frequency factor for the reaction, R is the universal gas constant, T is the temperature (in Kelvin), and k is the reaction rate coefficient which can be related to final diameter after a specific growth time. Thus, E_a can be evaluated from the reaction rate coefficient at any temperature (within the validity of the Arrhenius equation).

Summarised data of measurement involved is presented in Table 3.1. By using calculated value $\ln[1/\text{Diameter}]$ versus $1/T$ gives Figure 3.5.

Table 3.1 Diameter size spheres by increasing temperature after 40 minutes growth

Diameter (nm)	$\ln [1/\text{Diameter}]$	T (Kelvin)	$1/T$ (K^{-1})
-	-	343	2.92×10^{-3}
475	-6.16	353	2.83×10^{-3}
398	-5.99	358	2.79×10^{-3}
373	-5.92	363	2.75×10^{-3}

As expected, the E_a as determined from Figure 3.5 is low suggesting that the reaction is occurring rapidly.

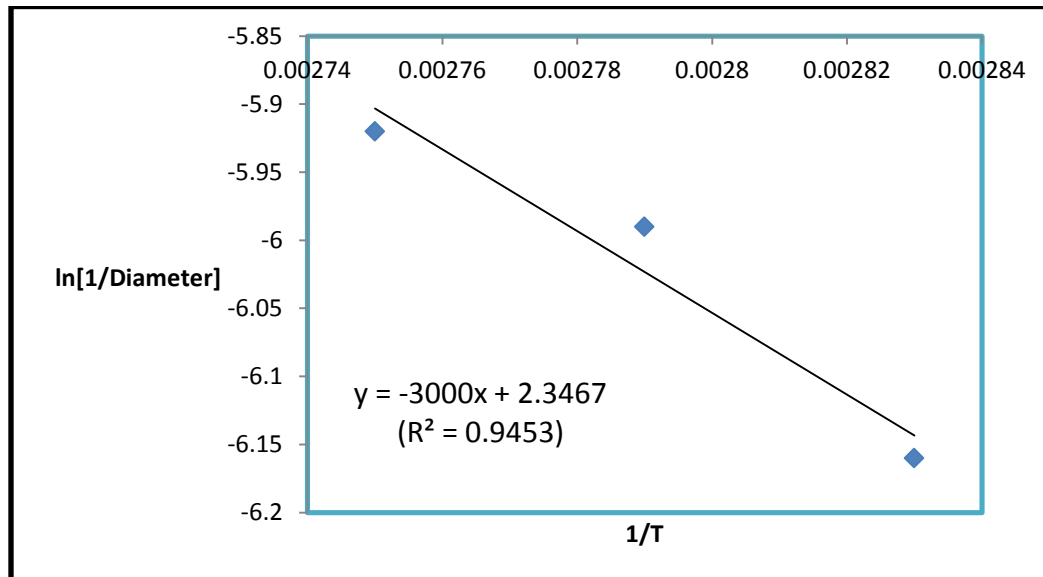


Figure 3.5 Graph showing $\ln [1/\text{diameter}]$ vs. $1/T$ showing the relationship between a measure of the rate of reaction and temperature. From this graph the activation energy for the production of PMMA spheres is estimated to be on the order of 25 kJ mol^{-1} , with the estimate being calculated from the slope which is equal to $-E_a/R$, where R is the gas constant.

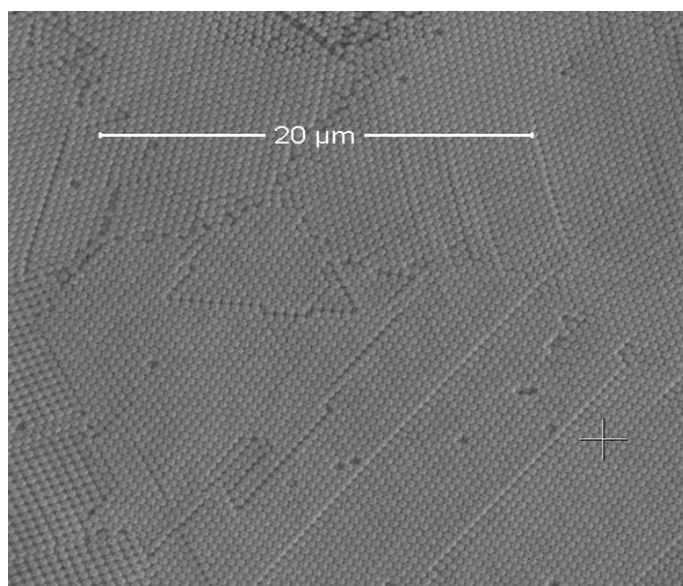


Figure 3.6 SEM image of colloidal PMMA drops on a silicon wafer for sample 373nm, is showing the high level of particle uniformity.

Chapter 3

Average particle sizes were determined by SEM measurements, approximately 60-70 particles were measured as shown in Figure 3.7. The monodispersity of the colloidal particles was determined by calculation of the particle size distribution.

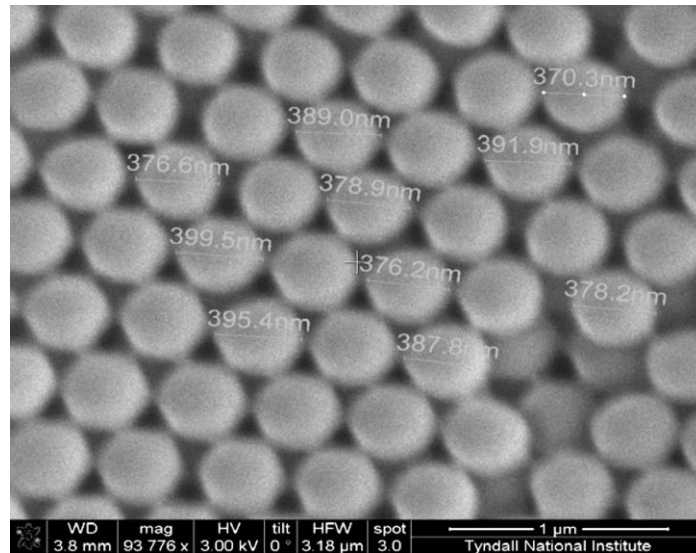


Figure 3.7 SEM image of PMMA particles produced from at 15 mL MMA (Sk25)

Table 3.2 shows the average diameter size of PMMA with varying concentration of monomer and with varying temperature at optimum concentration. Monodispersity needs to be <5% for high quality opal films formation. From the average diameter sizes given in Table 3.2, it is apparent that PMMA preparation at 90°C was not good for particles below 373nm, and at 15ml of MMA monomer achieved <5% in all cases. Experimental parameters at 90°C need to be improved upon to create particles <5% when making particles of <373nm diameter.

Table 3.2 Average diameter size of synthesized PMMA

Temperature	MMA	Avg. Diameter (nm)
90°C	5 ml	290 ± 7%
90°C	10 ml	342 ± 8%
90°C	15 ml	373 ± 5%
90°C	20 ml	563 ± 4%
90°C	25 ml	763 ± 3%
80°C	15 ml	475 ± 5%
85°C	15 ml	398 ± 4%

3.3 Conclusions

The aqueous synthesis of PMMA sub-micron spheres is a simple, cheap and relatively quick preparation, typically 40 minutes to completion due to the higher temperatures used as compared to previous studies in literature, which is capable of producing highly uniform PMMA spheres. Synthesis at higher temperatures speeds up both the chemical reaction and physical diffusion, and as a result shortens the time for the formation of the spheres. This results in the formation of more spheres, with a consequent reduction in particle size. This effect may arise from the fact that at higher temperatures the reactivity of the initiator may be enhanced, such that more polymerisation sites are created. When the amount of MMA monomer increases, the particles size of PMMA also increases.

Chapter 3

Further work is required in order to improve monodispersity at 90°C for particles below 373nm.

References

1. Waterhouse, G.I.N. and Waterland, M.R. *Opal and inverse opal photonic crystals: Fabrication and characterization*. Polyhedron, 2007. **26**(2): p. 356-368.
2. Zhang, J., Sun, Z. and Yang, B. *Self-assembly of photonic crystals from polymer colloids*. Current Opinion in Colloid & Interface Science, 2009. **14**(2): p. 103-114.
3. Liu, Z., Jin, Z., Li, W., Qiu, J, Zhao, J. and Liu, X. *Synthesis of PS colloidal crystal templates and ordered ZnO porous thin films by dip-drawing method*. Applied Surface Science, 2006. **252**(14): p. 5002-5009.
4. Jiang, P., Sun, C.H., Linn, N.C., Ho, B.J. and Venkatesh. *Self-assembled photonic crystals and templated nanomaterials*. Current Nanoscience, 2007. **3**(4): p. 296-305.
5. Paquet, C. and Kumacheva, E. *Nanostructured polymers for photonics*. Materials Today, 2008. **11**(4): p. 48-56.
6. Romanov, S.G., Maka, T., Sotomayor Torres, C.M., Muller, M., Zentel, R., Cassagne, D., Manzanares-Martinez, J. and Jouanin, C. *Diffraction of light from thin-film polymethylmethacrylate opaline photonic crystals*. Physical Review E, 2001. **63**(5): p. 056603.
7. Chiu, T.-P. and Don, T.-M. *Synthesis and Characterization of Poly(methylmethacrylate) Nanoparticles by Emulsifier-Free Emulsion Polymerization with a Redox-Initiated System*. Journal of Applied Polymer Science, 2008. **Vol. 109**: p. 3622-3630

Chapter 3

8. D'Amato, R., Venditti, I., Russo, M.V. and Falconeiri, M. *Growth control and long-range self-assembly of poly(methyl methacrylate) nanospheres*. Journal of Applied Polymer Science, 2006. **102**(5): p. 4493-4499.
9. Tanriseer, T. Okay, O. and Sonmezoclu, I.C. *Kinetics of Emulsifier-Free Emulsion Polymerization of Methyl Methacrylate*. Journal of Applied Polymer Science, 1996. **Vol. 61**: p. 485-493.
10. Schroden, R. and Balakrishnan, N. *Inverse opal photonic crystals a laboratory guide*. 2001, University of Minnesota. p. 1-32.
11. Gu, Z.-Z., Chen, H., Zhang, S., Sun, L., Xie, Z. and Ge, Y. *Rapid synthesis of monodisperse polymer spheres for self-assembled photonic crystals*. Colloids and Surfaces A: Physicochemical and Engineering Aspects, 2007. **302**(1-3): p. 312-319.

Chapter 4: Synthesis of Highly Monodisperse Poly(methyl methacrylate)-Au Core-Shell Particles and their use in the Fabrication of 3-D Metallodielectric Photonic Crystals

4.1 Introduction

Bi-layered and multi-layered structural designs surrounded or covered with metal nanoparticles (NPs) have recently attracted considerable attention owing to their topological complexity and their optical properties, often resulting from the activity of surface plasmon resonances, which originate from the collective oscillations of conduction electrons in reaction to optical excitation. Among these core-shell (CS) structures having particles surrounded with metal nanoparticles (NPs) typically silver or gold are of particular interest, allowing one to manipulate and use the metal NPs in a much easier and convenient way [1-3]. The surface plasmon resonance (SPR) frequency

Chapter 4

depends on the particle size, shape and the surrounding dielectric medium [4]. For example the SPR peak of 13 nm spherical gold colloids is around 520 nm and that of 5-6 nm silver nanoparticles around 400 nm [2]. SPR has been explored for use in fabricating optical filters [5], active surfaces for enhanced Raman spectroscopy [2, 6, 7] fluorescence scattering [8], and chemical and biological sensors [6].

The composite NPs that consist of a dielectric core coated with a few nanometres of metal have shown tremendous promise for systematic engineering of SPR. The SPR of these NPs can be varied over hundreds of nanometres in wavelength, across the visible and into the infrared region of spectrum, by varying the relative dimensions of the core and the shell. In most studies involving surface plasmons, gold and silver are the most often used, because silver produces a sharp resonance, and gold is more stable in air and is generally inert [8].

Synthesis of gold NPs onto both silica (Si) and polystyrene (PS) cores has been reported [9, 10]. The advantage of using polymer colloids instead of silica is that they are easily removed by solvent dissolution or thermal calcination, when acting as templates for macroporous materials or inverse opals. It was reported that silica@Au CS particles were less stable to form a photonic crystals film [3]. The formation of a second silica shell around the metal NPs, often referred to as core-shell-shell (CSS) particles, makes silica@metal CS particles more stable, and easier to use when making photonic crystal films.

4.2 Preparation of Gold Nanoparticles

Many chemical and physical techniques have been developed to prepare metal nanoparticles, such as chemical reduction using a reducing agent [5, 11], electrochemical reduction [12], photochemical reduction [13], and thermal evaporation (including chemical vapour deposition) [14]. Physical methods usually require high temperatures (>1000 °C), vacuum and expensive equipment. However, there are also easy and convenient chemical methods that use dilute aqueous solutions and simple equipment.

In general, chemical reduction reactions involve reducing agents that react with a salt of the metal according to the following chemical equation:

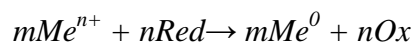


Table 4.1 gives a list of reagents most commonly used in the reduction of gold with the appropriate conditions. Some chemical methods to prepare gold nanoparticles are also described.

Table 4.1 Guidelines for the choice of reducing agents and reaction conditions in the production of Au nanoparticles (adapted from Ref.[15]).

<i>Metal species</i>	<i>E⁰/V</i>	<i>Reducing agent</i>	<i>Conditions</i>	<i>Rate</i>
Au ³⁺	≥ + 0.7	Alcohol, polyols	≥ 70 °C	Slow
		Aldehydes, sugars	< 50 °C	Moderate
		Hydrazine, H ₃ PO ₂	Ambient	Fast
		NaBH ₄ , boranes	Ambient	Very fast
		Citrate	> 70 °C	Moderate

Synthesis of gold nanoparticles by reducing agents such as sodium borohydride[16], ascorbic acid in presence of cetyltrimethylammonium bromide (CTAB) [17], sugars (glucose, fructose and sucrose) [18] have been reported. A common method used to synthesize gold nanoparticles is the reduction of chloroauric acid (HAuCl₄) with tri-sodium citrate, Na₃C₆H₅O₇. Kandimalla [8] reported stability of the nanoparticles can be achieved by the addition of a stabilizing agent like sodium citrate. Citrate-capped nanoparticles are negatively charged and attract positively charged particles from the solution, resulting in the formation of an electrical double layer and repulsive forces between particles, which prevent agglomeration [1, 9, 19, 20].

Chapter 4

Ho Youk [5] describes in-situ anchoring of Au NPs onto the surface of PMMA using surface-grafted poly(allylamine) (PAA). Au NPs were synthesized onto PMMA as shown in Figure 4.1. The concept was to produce PMMA decorated with the Au NPs onto the surface and is similar to this study. However reviewing their image TEM results it can be seen (Figure 4.2) that, the gold NPs coating is not homogeneous and the size of the polymer particles was not uniform. This could be due to the parameters (e.g. temperature, chemical composition, stirring speed etc.) during synthesis of the PMMA/PAA which could be refined to form uniform particles before grafted with Au NPs.

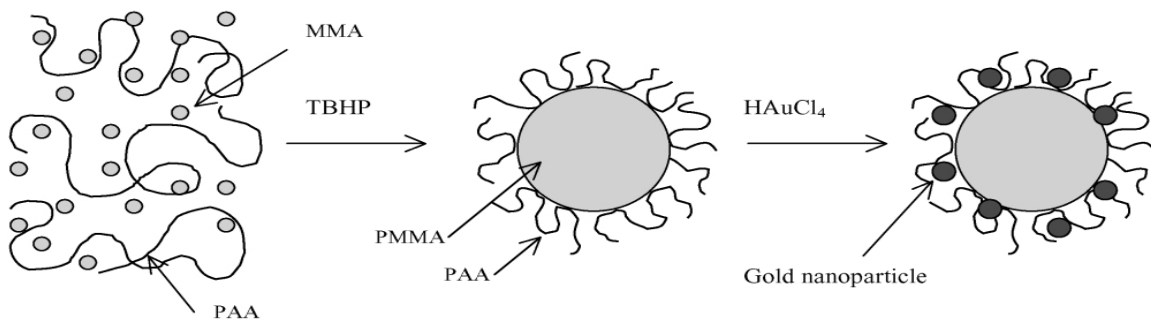


Figure 4.1 Schematic representation of the formation of PMMA/PAA nanosphere and gold nanoparticles (adapted Ref.[5])

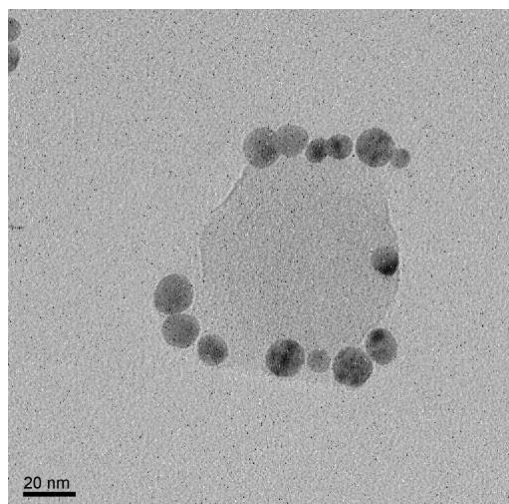


Figure 4.2 TEM micrographs of gold nanoparticles on PAA/PMMA nanospheres (from Ref. [5])

4.3 Synthesis of PMMA@Au Core-Shell Nanoparticles

This study focusses on the synthesis and characterisation of PMMA core particles decorated with gold NPs. To the best of our knowledge there have been no previous literature reports of gold NPs formed onto PMMA spheres using polyethyleneimine (PEI) as a linker. PMMA@Au CS particles were synthesised in order to investigate their usefulness in making photonic crystals and structures for Raman spectroscopy studies. These metallodielectric photonic crystals (MDPCs), which are a relatively novel class of metamaterials, may be prepared from monodisperse CS particles. In this project, a bi-layer technique has been developed to prepare PMMA@Au CS particles using polyethyleneimine (PEI) acting as both a linker between the Au nanoparticles and the PMMA particles, and as a reducing agent in the formation of the Au NPs.

Chapter 4

UV-visible absorption spectroscopy was employed in order to investigate both the gold nanoparticles and the PMMA particles coated with gold in terms of their plasmonic and combined plasmonic/photonic properties respectively. Metal surface plasmons, or more correctly surface plasmon polaritons, arise via the interaction of light with electrons in the surface of the metallic nanoparticle gold [2, 3, 21]. Most commonly observed for gold or silver nanoparticles, at a specific wavelength of light collective oscillations of electrons may be excited via a direct absorption process that often results in the appearance of intense colours. The particular wavelength of light where this occurs is strongly dependant on nanoparticle size and shape. A shift to longer wavelengths of the absorption maximum occurs as the nanoparticle size increases.

Here we focus on the use of gold nanoparticles since as noted earlier, these may be readily prepared and stabilised via surface treatment, while also being relatively inert.

PMMA particles were prepared using the emulsifier-free polymerisation process (as described previously in Chapter 3) targeting sphere diameters of 373 nm. These spheres were then coated with Au nanoparticles (prepared as described in Chapter 2). The specific issue that was addressed in this work concerned the need to prepare an outer shell of gold nanoparticles. This required the identification of suitable chemical linker, in order to attach the Au nanoparticles to the polymer core particles which must be used in conjunction with the capping agent designed to prevent agglomeration.

Polyethylene (PEI) was selected for this purpose. Accordingly a method was devised in which a thin PEI shell was attached to the PMMA particles, which then facilitated attachment of the Au nanoparticles via reaction with the citrate-stabilised Au nanoparticles, as described in Chapter 2.

The overall process is described in Figure 4.3. The electrostatic attraction between the negatively charged (citrate stabilized) Au NPs and the positively charged PEI chains on the surface of PMMA results in a single layer of the Au NPs binding onto the PMMA cores, producing the PMMA@Au CS composite particles. Ho Youk [5] reported that microspheres having a net positive charge after protonation of surface amine groups exhibited excellent adhesion to gold colloids, and this appears to be the case here.

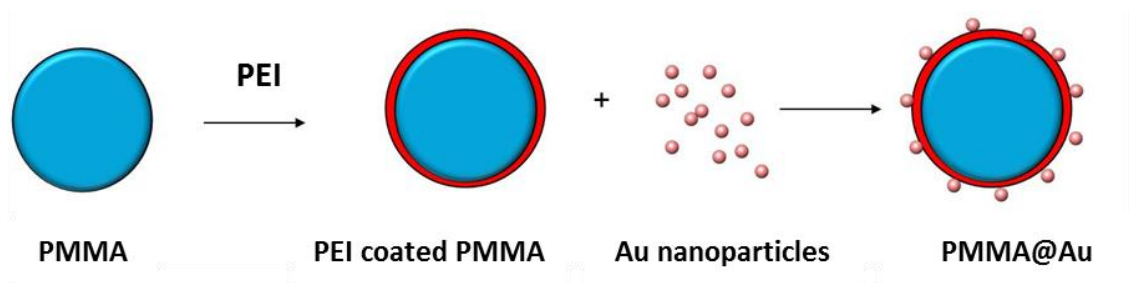


Figure 4.3 Schematic diagram of the synthesis method to produce PMMA@Au core-shell nanoparticles

The advantage of using PEI as compared to the frequently used silane coupling agents was threefold. Firstly the complexity in achieving a uniform surface coverage using silane coupling agents is avoided when using PEI. This is because the branches available from each PEI molecule, with multiple $-NH_2$ end groups, are sufficient to achieve

Chapter 4

complete surface coverage on the PMMA spheres [3]. Secondly the use of PEI as a surface primer results in the PMMA particles being separated electrostatically by a positive surface charge in the aqueous media. This also aids complete coverage of each PMMA particle with the Au NPs. The final advantage of using PEI is that stringent pH control is not required, unlike when using silane coupling agents. Mulvaney and Liz Marzan's [1] group have demonstrated the importance of pH control involved in the silane coupling process, In our experiments, after PEI treatment, the particles were washed at least three times with ultrapure water. At this stage the pH was in the region of 8-9, and at this pH range the PEI modified PMMA particles will be electrostatically separated by their inherent positive charge.

Zeta potential (ζ -potential) is an indicator of the stability of colloidal dispersions. The magnitude of the zeta potential indicates the degree of electrostatic repulsion between adjacent, similarly charged particles in dispersion. For molecules and particles that are small enough, a high zeta potential will confer stability, i.e., the solution or dispersion will resist aggregation. When the potential is small, attractive forces may exceed this repulsion and the dispersion may flocculate. Accordingly, colloids with high zeta potential (negative or positive) are electrically stabilized while colloids with low zeta potentials tend to coagulate or flocculate. Table 4.2 presents the ζ -potentials of the particles employed here at different stages of their preparation. The PMMA surfaces before PEI treatment show a negative ζ -potentials (-52.7 mV) and the PEI modification resulted in a change in its ζ -potentials to +54.5 mV as expected due to the positive charge

arising from the PEI layer. The as-prepared citrate-stabilized Au NPs show a negative ζ -potentials (-34.2 mV), clearly indicating the difference in surface potentials. The PMMA@Au CS particles show a ζ -potentials value of -42.1 mV.

Table 4.2 ζ -potentials data of colloids at various stages in the preparation of PMMA@Au core-shell particles.

<i>Sample</i>	<i>ζ-potentials (mV)</i>
PMMA	-52.7
Au sol	-34.2
PMMA@PEI	+54.5
PMMA@Au	-42.1

The Au nanoparticle shells were studied using TEM, Figure 4.4 clearly confirms the incorporation of Au nanoparticles onto the surfaces of the PMMA particles. An increase in the composite size was also observed. The particles remained spherical, however the surface roughness increased as compared to the PMMA spheres due to the existence of Au nanoparticles on the surface (Figure 4.4). From Figure 4.4 it can be seen that the gold nanoparticles are attached homogeneously onto the surface of all PMMA particles.

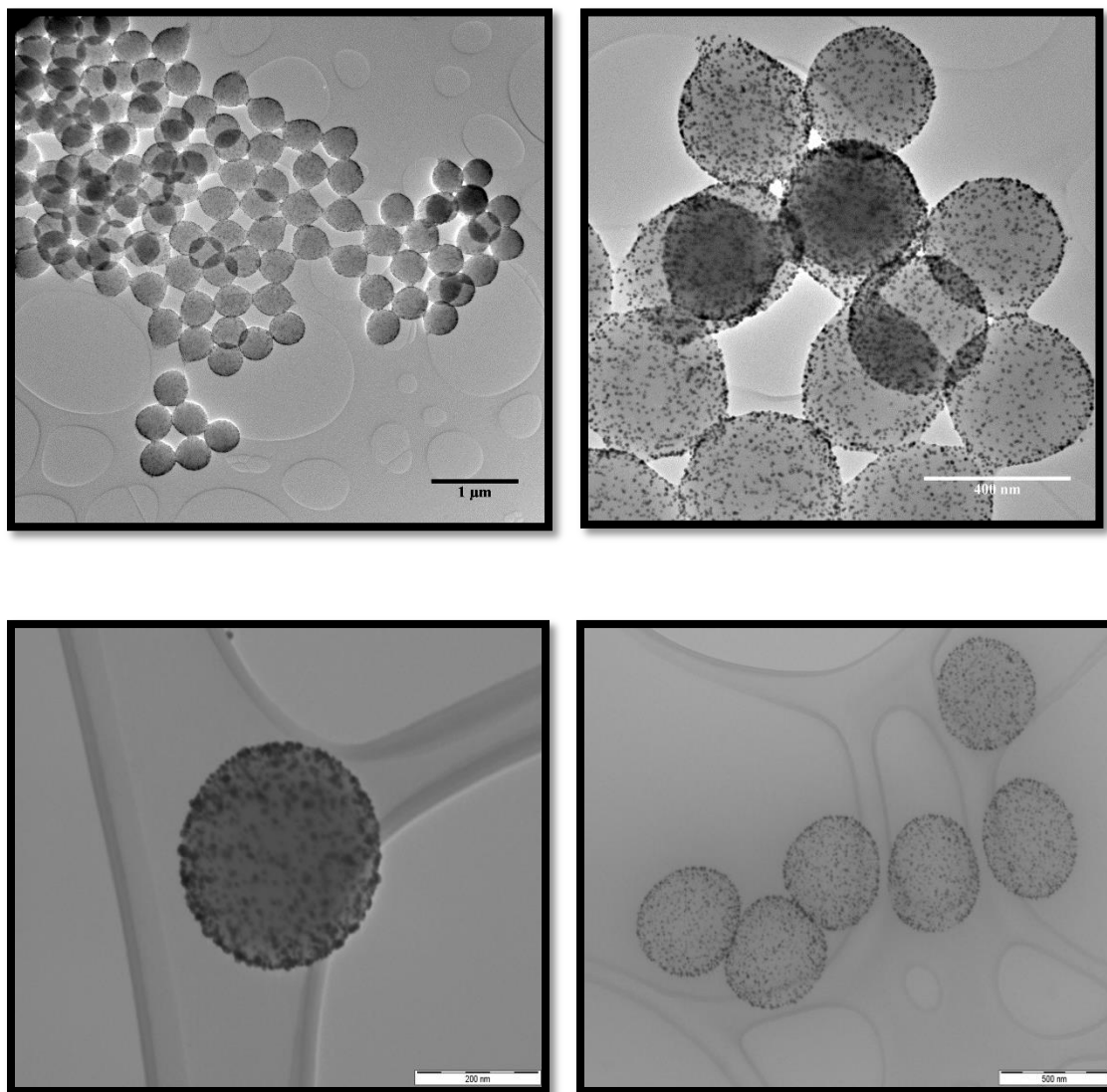


Figure 4.4 TEM images of PMMA@Au core-shell NPs at different magnifications.

Figure 4.5 is a high resolution TEM image of the gold nanoparticles attached to the PMMA sphere, which reveals the presence of lattice fringes indicating that the material is crystalline.

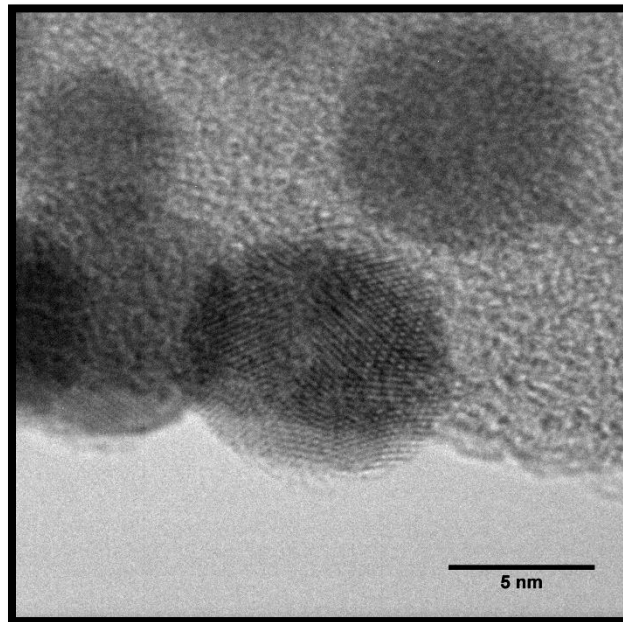


Figure 4.5 A high-resolution TEM image of a PMMA@Au core-shell particle showing crystalline lattice planes in Au NPs

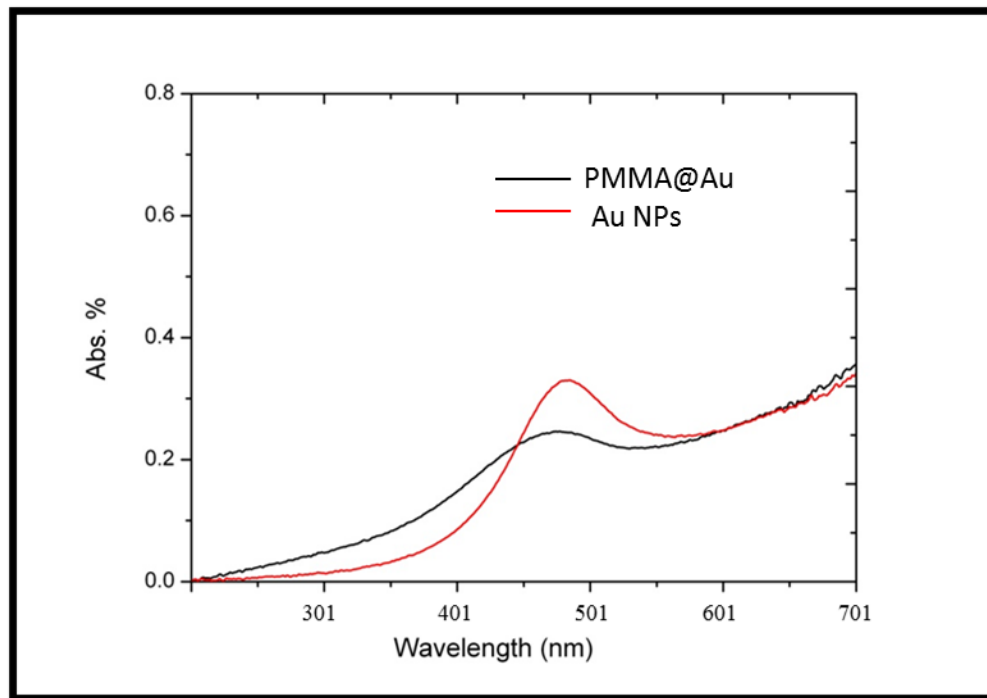


Figure 4.6 Absorption spectra of PMMA@Au core-shell and Au nanoparticles

Figure 4.6 presents UV-visible absorption spectra of PMMA@Au CS and aqueous suspension of Au NPs. In the case of PMMA@Au CS particles, as the attached gold nanoparticles grew and merged, the surface plasmon resonance (SPR) systematically shifted, consistent with previous studies [21]. PMMA spheres decorated with gold NPs show a less intense absorption peak. As the coverage of gold NPs on PMMA increases, the SPR peak shifts to higher wavelengths (red-shift) to approximately ~540 nm. The slight red shift of the plasmonic bands occurring for the core-shell compare to the bare Au NPs may be attributed to the change in the dielectric environment of the Au NPs

Chapter 4

although the possibility that some Au particles are sufficiently close to each other so as to effectively alter their size and hence the position of the SPR, cannot be ruled out.

The selected area (electron) diffraction (SAED) pattern of the PMMA@Au CS NPs is presented in Figure 4.7. The pattern was fitted with powder X-ray diffraction (XRD) pattern of Au (International Centre for Diffraction Data (ICDD) reference code 98-005-1004). This SAED pattern shows the various diffraction spots arising from the gold nanoparticles, which indicate that as expected, the crystallinity of the gold is retained after attachment to the PMMA spheres. The SAED pattern fits well to the database XRD pattern and contains diffraction peaks associated with the (111), (002), (022) (113) and (222) planes. The particles exhibit preferential reflections associated with the (111) and (002) planes.

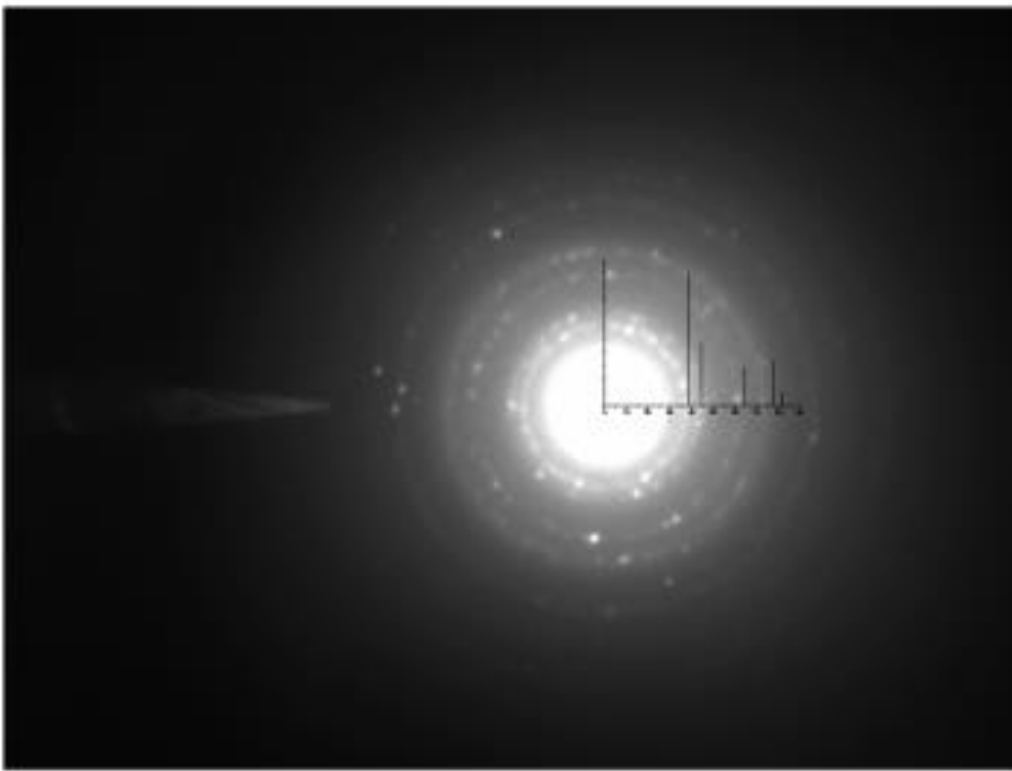


Figure 4.7 SAED image of PMMA@Au core-shell NPs overlaid with the XRD pattern of Au taken from the ICDD database. It may be seen that there is a reasonable alignment of the diffraction rings seen in the SAED pattern with the lines of the reference XRD pattern.

Table 4.3 List of diffraction peaks for the various planes of Au (by measuring the angles, 2θ and intensities) that show a reasonable agreement with the SAED pattern of PMMA@Au core-shell as seen in Figure 4.8

Peak list						
No.	h	k	l	d [Å]	2Theta[deg]	I [%]
1	1	1	1	2.35559	38.175	100.0
2	0	0	2	2.04000	44.370	47.0
3	0	2	2	1.44250	64.553	28.8
4	1	1	3	1.23017	77.537	33.6
5	2	2	2	1.17779	81.691	9.6

4.4 Fabrication of PMMA@Au Photonic Crystal Films

PMMA@Au CS NPs were deposited on the cleaned glass substrate by controlled evaporation at 60°C. As shown in the Figure 4.8, the PMMA@Au CS film exhibited brilliant colours which can be observed by the naked eye and change with the angle of observation as expected.

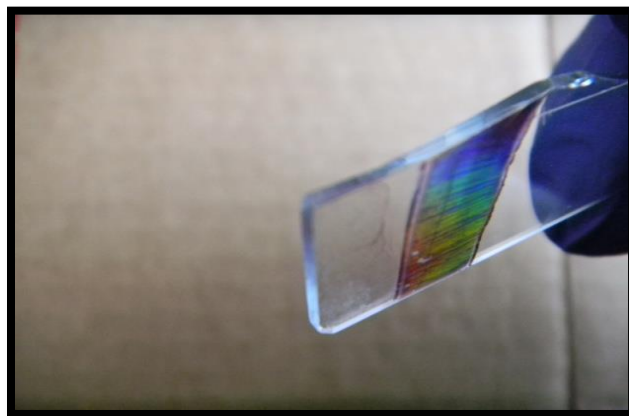


Figure 4.8 PMMA@Au core-shell film showing distinct colour to the naked eye, indicating the quality of the controlled evaporation photonic crystal film.

Figure 4.9 shows the close packed arrangement of the PMMA@Au CS NPs film as revealed by SEM. The Au NPs coating each PMMA particle are again visible and the SEM image again reveals level of Au coating on the PMMA core particles.

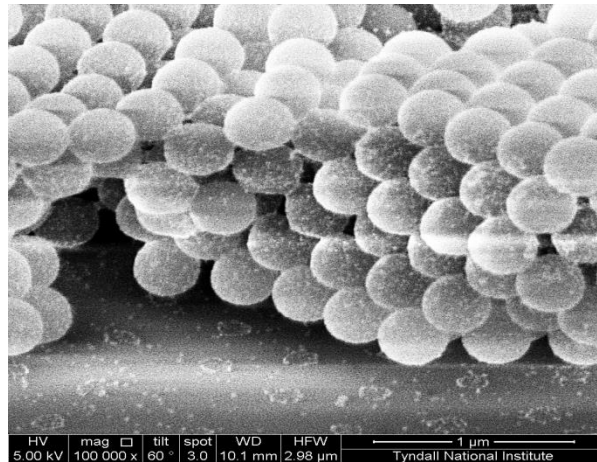


Figure 4.9 Cross section SEM image of PMMA@Au core-shell film.

4.5 Optical Properties of PMMA@Au Core-Shell Photonic Crystal Films

In order to observe the optical properties of PMMA@Au CS films, reflection measurements were carried out using films made from both bare PMMA and Au:PMMA particles. Reflectance measurements were made at various angles of incidence. Figure 4.10 a and b shows normalised reflectance measurements of a PMMA@Au CS photonic crystal film recorded at incidence angles of between 10° to 40° and 45° to 75° , respectively. The reflectance spectrum measured at an incident angle θ of 10° shows a

Chapter 4

broad band centred at 964nm, and shows an angle-dependent blue shift (shifted towards shorter wavelengths) with increasing angle of incidence up to 70° . This observation is consistent with the expected behaviour for a photonic crystal in terms of the Bragg-Snell relationship, see Chapter 1.

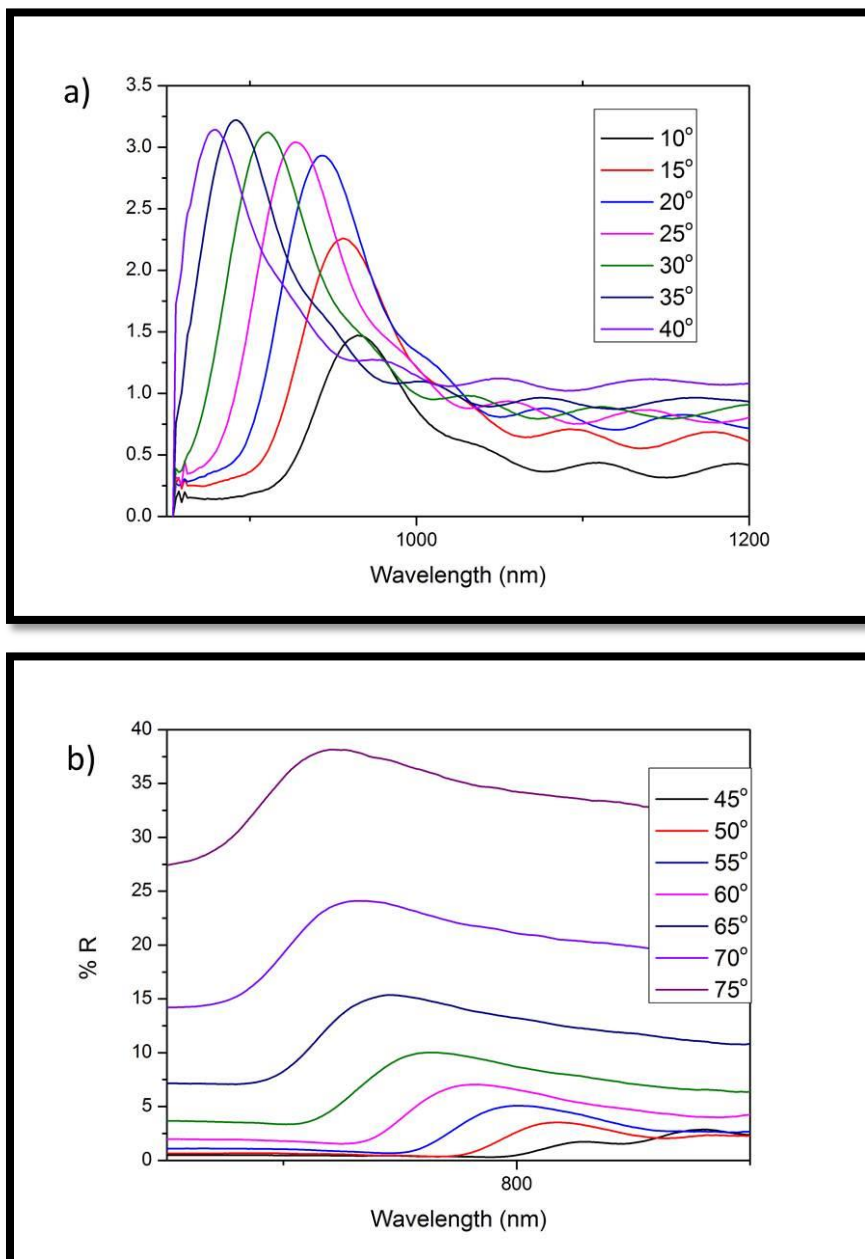


Figure 4.10 Angle-resolved reflectance spectra of PMMA@Au core-shell obtained at incident angles of 10° to 40° (a) and 45° to 75° (b) with respect to the normal to the surface (parallel to substrate surface). Spectra were shifted in the Y axis for clarity.

Chapter 4

The correlation with the Bragg-Snell relationship is further confirmed by fitting the data points obtained to a plot of the square of the wavelength maximum (λ_{\max}^2) for the stop bands recorded at various angles of incidence, θ , against $\sin^2\theta$. The linear fit shown in Figure 4.11 is in complete agreement with the Bragg-Snell relationship. Using the plot shown in Figure 4.11, η_{eff} can be calculated, and was found to have increased from 1.43 to 1.51 due to the decoration of gold NPs. This may be due to a contribution for the refractive index of the Au NPs although analysis of the data also suggests that some shrinkage of the spheres has resulted during the processing, from ca. 415 nm to 393 nm. This shrinkage could result in a slight densification of the PMMA particles, leading to an increase in the refractive index of said particles, and a consequent increase in the effective refractive index.

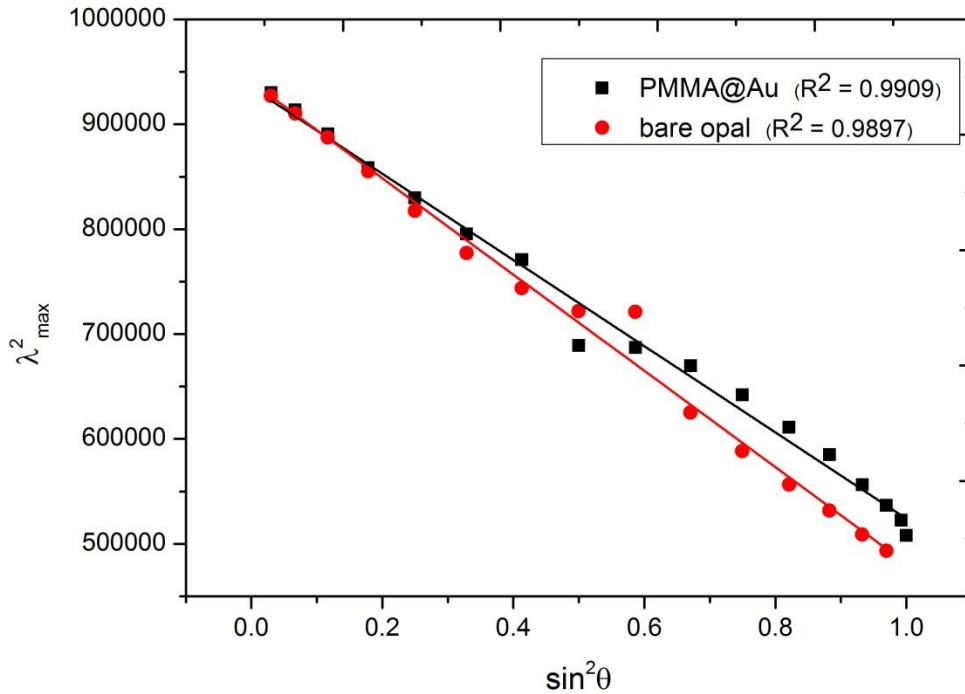


Figure 4.11 Plot of λ_{\max}^2 vs $\sin^2\theta$ showing a linear fit. After being decorated with gold NPs, the effective RI (η_{eff}) of the composite increased from 1.43 to 1.51.

The influence of the Au NPs on the optical properties of the MDPC was then evaluated (Figure 4.12). The obvious changes in the spectra were, (i) a considerable reduction in the reflected spectral intensity, and (ii) the broadening of the stop band as compared to the PhCs made from uncoated PMMA spheres of similar size. Our findings suggest that the reduction in the reflected intensity is attributable to the metal plasmonic absorption and scattering. Figure 4.12 shows the reflection peak of PMMA bare opal and PMMA@Au CS at 10° . The Bragg peak wavelength for PMMA bare opal is located at ~ 964 nm. The

Au loading didn't make any significant change to the Bragg peak wavelength. However, the percentage of reflectance for the PMMA@Au CS film is reduced to <10%, which is due to the voids being partly infilled with gold.

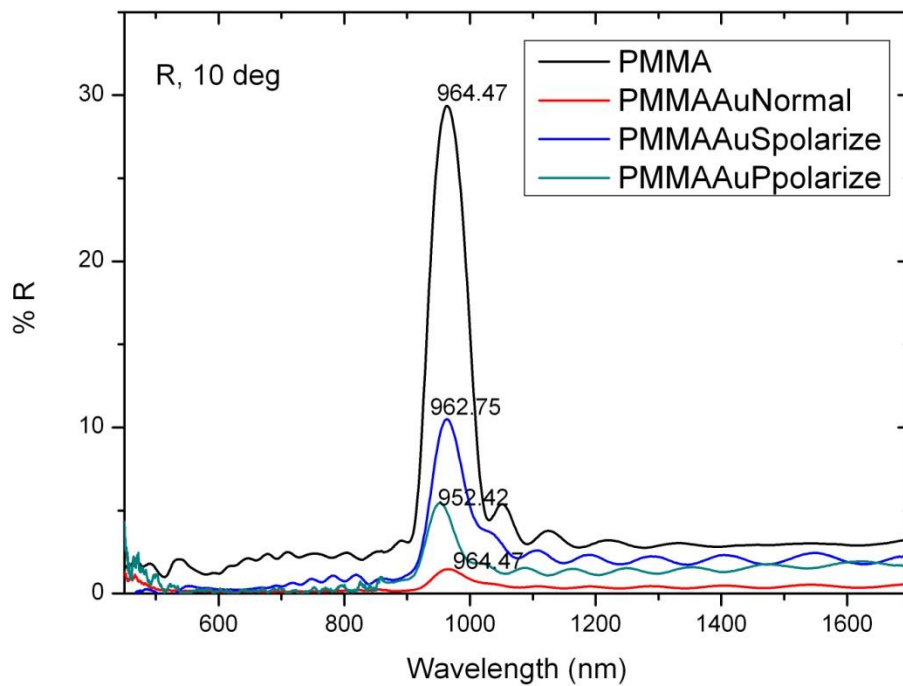


Figure 4.12 Reflection spectra of PMMA bare opal and PMMA@Au core-shell under normal, s-polarised and p-polarised light respectively.

Figure 4.13 shows a comparison of transmission spectra at 10° between a PMMA bare opal and a PMMA@Au CS film. The PMMA@Au sample shows no transmission at 600

nm for all polarisations studied. This is most likely due to the Au nanoparticles absorbing via their SPRs.

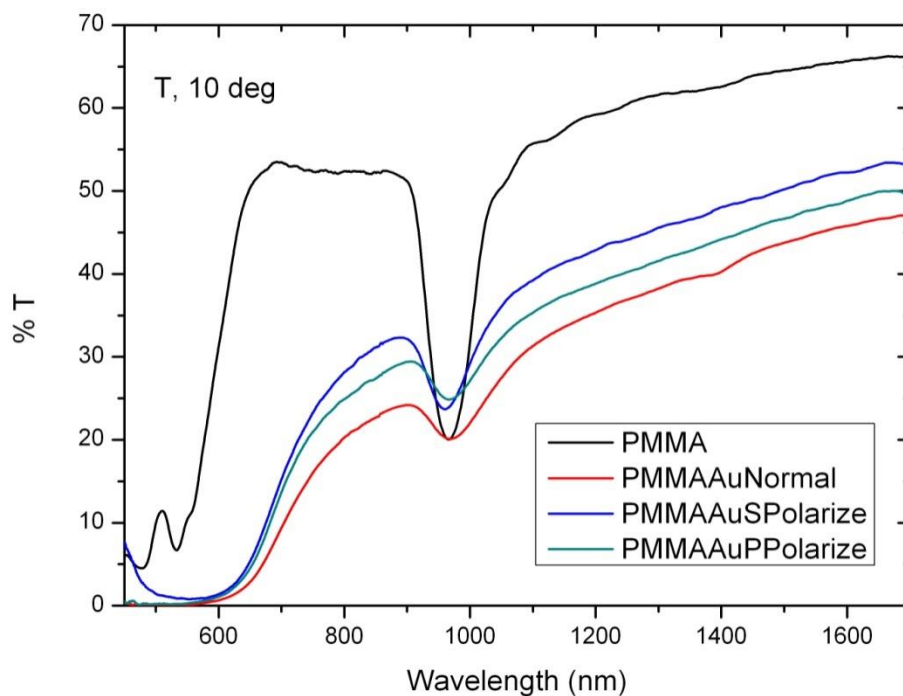


Figure 4.13 Transmission spectra of PMMA bare opal and PMMA@Au core-shell under normal, s-polarised and p-polarised light respectively.

4.6 Conclusions

We have established a simple reproducible method for the synthesis of highly monodisperse PMMA@Au CS particles using a linker agent which has not been

previously employed for PMMA particle decoration. We were able to use these particles to assemble into a reasonably high quality photonic crystal films.

Optical data reveal a slight increase in effective refractive index along with a decrease of the particles size in the composite material. The refractive index acquires an imaginary component due to the presence of Au NPs and the SPR associated with these NPs dominate part of the transmission spectrum. The angle resolved optical reflectance spectra of this material built by assembling dielectric@metal core-shell particles show good agreement with the Bragg–Snell correlation.

SPRs associated with Au NPs find use in many different sensing applications. It is quite possible that the added functionality associated with the photonic band gap which is also present in the composite material may enhance and improve such devices. A very preliminary study of the use of such materials for surface-enhanced Raman spectroscopy is given in Appendix A.

References

1. Liz-Marzán, L.M., Giersig, M. and Mulvaney, P. *Synthesis of nanosized gold–silica core–shell particles*. *Langmuir*, 1996. **12**(18): p. 4329-4335.
2. Yong, K.-T., Sahoo, Y., Swihart, M.T. and Prasad, P.N. *Synthesis and plasmonic properties of silver and gold nanoshells on polystyrene cores of different size and of gold–silver core–shell nanostructures*. *Colloids and Surfaces A: Physicochemical and Engineering Aspects*, 2006. **290**(1–3): p. 89-105.
3. Padmanabhan, S.C., McGrath, J., Bardosova, M. and Pemble, M.E. *A facile method for the synthesis of highly monodisperse silica@gold@silica core-shell-shell particles and their use in the fabrication of three-dimensional metallodielectric photonic crystals*. *Journal of Materials Chemistry*, 2012. **22**(24): p. 11978-11987.
4. Kelly, K.L., Coronado, E., Zhao, L.L. and Schatz, G.C. *The optical properties of metal nanoparticles: the influence of size, shape, and dielectric environment*. *The Journal of Physical Chemistry B*, 2002. **107**(3): p. 668-677.
5. Ho Youk, J. *Preparation of gold nanoparticles on poly(methyl methacrylate) nanospheres with surface-grafted poly(allylamine)*. *Polymer*, 2003. **44**(18): p. 5053-5056.

Chapter 4

6. Willets, K.A. and Van Duyne, R.P. *Localized surface plasmon resonance spectroscopy and sensing*. 2007, Annual Review of Physical Chemistry. p. 267-297.
7. Tessier, P., Velev, O., Kalambur, A., Rabolt, J., Lenhoff, A. and Kaler, E. *Assembly of gold nanostructured films templated by colloidal crystals and use in surface-enhanced Raman spectroscopy*. J. Am. Chem. Soc., 2000. **122**(39): p. 9554-9555.
8. Kandimalla, V.K., *Influence of Metal Nanoparticles on Fluorescence Properties*, in *Department of Chemistry*. 2010, Eastern Michigan University: Ypsilanti, Michigan.
9. Zhou, J., Ren, F., Wu, W., Zhang, S., Xiao, X, Xu, J. and Jiang, C. *Controllable synthesis and catalysis application of hierarchical PS/Au core-shell nanocomposites*. Journal of Colloid and Interface Science, 2012. **387**(1): p. 47-55.
10. Xie, Y., Chen, T., Cheng, Y., Wang, H., Qian, H. and Yao, W. *SiO₂@Au nanoshells-based SERS method for detection of sunset yellow and chrysoidine*. Spectrochimica Acta Part A: Molecular and Biomolecular Spectroscopy, 2014. **132**(0): p. 355-360.
11. Kuroda, K., Ishida, T. and Haruta, M. *Reduction of 4-nitrophenol to 4-aminophenol over Au nanoparticles deposited on PMMA*. Journal of Molecular Catalysis A: Chemical, 2009. **298**(1-2): p. 7-11.

12. Zhang, D.-W., Chen, C.H., Zhang, J. and Ren, F. *Fabrication of nanosized metallic copper by electrochemical milling process*. Journal of Materials Science, 2008. **43**(4): p. 1492-1496.
13. Maillard, M., Huang, P. and Brus, L. *Silver nanodisk growth by surface plasmon enhanced photoreduction of adsorbed [Ag⁺]*. Nano Letters, 2003. **3**(11): p. 1611-1615.
14. Bae, C.H., Nam, S.H. and Park, S.M. *Formation of silver nanoparticles by laser ablation of a silver target in NaCl solution*. Applied Surface Science, 2002. **197–198**(0): p. 628-634.
15. Goia, D.V. and Matijevic, E. *Preparation of monodispersed metal particles*. New Journal of Chemistry, 1998: p. 1203-1215.
16. Wagner, J., Tshikhudo, T.R. and Köhler, J.M. *Microfluidic generation of metal nanoparticles by borohydride reduction*. Chemical Engineering Journal, 2008. **135**, Supplement 1(0): p. S104-S109.
17. Cao, C., Park, S. and Sim, S.J. *Seedless synthesis of octahedral gold nanoparticles in condensed surfactant phase*. Journal of Colloid and Interface Science, 2008. **322**(1): p. 152-157.
18. Panigrahi, S., Kundu, S., Ghosh, S., Nath, S. and Pal, T. *General method of synthesis for metal nanoparticles*. Journal of Nanoparticle Research, 2004. **6**(4): p. 411-414.

Chapter 4

19. Amendola, V. *Synthesis for gold and silver nanoparticles for photonic applications*. PhD Thesis 2008.
20. Amendola, V. and Meneghetti, M. *Laser ablation synthesis in solution and size manipulation of noble metal nanoparticles*. *Phys Chem Chem Phys*, 2009. **11**(20): p. 3805-21.
21. Romanov, S.G., Susa, A., Sotomayor Torres, C.M., Liang, Z. and Caruso, F. *Surface plasmon resonance in gold nanoparticle infiltrated dielectric opals*. *Journal of Applied Physics*, 2005. **97**(8): p. 086103-3.

Chapter 5: Preparation of Gold and Nickel Metallodielectric Photonic Crystals (MDPCs) using PMMA Spheres via Electrodeposition

This chapter is based on the publication: *Syara Kassim, Siby C. Padmanabhan, Mathieu Salaun, and Martyn E. Pemble, ‘PMMA Gold Metallodielectric Photonic Crystals and Inverse Opals: Preparation and Optical Properties’* AIP Conference Proceedings, 2011. **1391(1)**: p. 263-265.

Contributions:

Syara Kassim	Prepared PMMA spheres, deposited metals by electrodeposition, produced inverse opals and wrote the paper
Siby Padmanabhan	Suggested corrections on the paper, performed SEM
Mathieu Salaun	Performed optical characterisations
Martyn Pemble	Suggested corrections on the paper

Chapter 5: Preparation of Gold and Nickel Metallodielectric Photonic Crystals (MDPCs) using PMMA Spheres via Electrodeposition

5.1 Introduction

The concept of incorporation of metal nanoparticles into PhCs has attracted interest ever-since such composite systems were theoretically predicted to have potential in opening up the PBGs [1]. Photonic crystals that also contain metals, metallodielectric materials, are of additional interest because of the possible influence of the metal plasmonic resonances on the photonic band gap properties [2]. Coupling of metal plasmonic resonance excitation with the PBG of the host opal structure in these structures could lead to a wide range of new or improved devices including decorative coatings, sensors, surface-enhanced Raman spectroscopy (SERS), photovoltaics, solar concentrators, passive optical components (filters, splitters), negative refractive index

Chapter 5

media devices such as cloaking devices, perfect (aberration free) lenses and optical interconnect technologies.

One of the bottlenecks that hinders the experimental demonstration of the optical properties of such MDPC structures is the attenuation of the incident light in the structure due to the high absorbance of the metal scatterers distributed in the voids of 3D PhCs structures. Preparation of their inverted structures has therefore been envisaged as an alternative way to investigate the optical properties of such 3D structures. Unfortunately successful experimental investigations of MDPC inverted structures are also hampered due to the difficulty in manufacturing robust 3D inverted MDPC structures with long range order.

The methods currently being investigated for the incorporation of metals in PhCs are chemical vapour deposition [3], dipping process [4] and chemical infiltration [5]. However these methods have their own limitations, the preliminary infiltrated layer of metal nanoparticles form a barrier to further deposition, thus preventing complete metal infiltration. Electrodeposition is a potential alternative approach where the barrier formation can be avoided by depositing the particles from the bottom to top.

In this study, infilling metals such as gold and nickel with three dimensional (3D) well-ordered macroporous structures has been achieved via an electrodeposition process. Gold substrates, with a gold thickness of 50 nm on glass slides from PHASIS, were used for nickel infiltration, and indium tin oxide (ITO) substrates were used for gold infiltration, due to their transparency. Completely infilled MDPC allows for the

manufacture of robust inverse opal structures by removal of the crystal template. The morphological and optical properties of these structures are discussed.

5.2 Preparation of Gold Infiltrated Opals and Inverse Opal

5.2.1 Gold Infiltration

The advantages of utilizing electrodeposition process is that the blocking of template surfaces can be avoided because gold is filling the nanochannels from bottom to top as shown in Figure 5. 2.

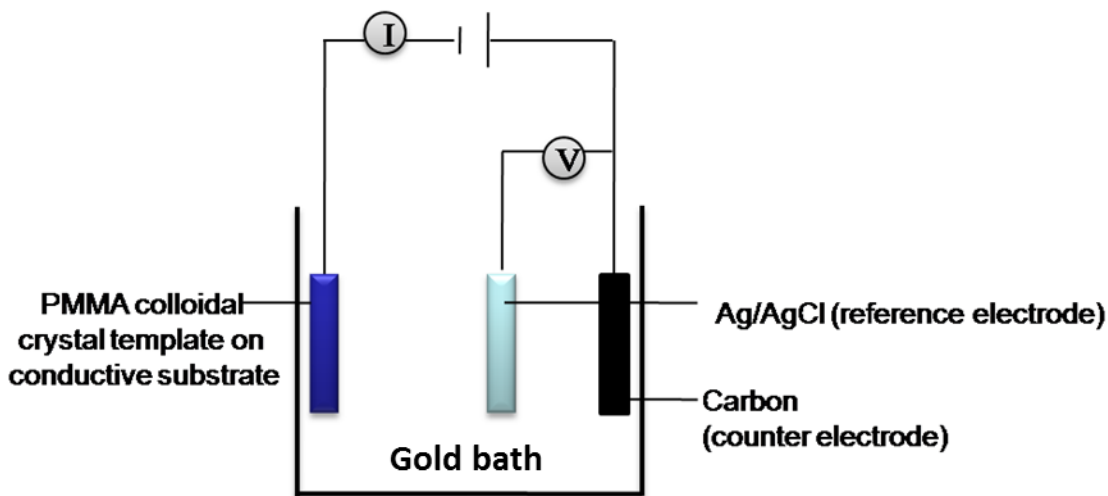


Figure 5.1 A schematic of the electrode arrangement for the deposition of gold into a PMMA colloidal crystal template

In this process, gold ions from a gold bath are electrochemically deposited onto PMMA colloidal crystal template at -1.0 V (Ag/AgCl), toward complete impregnation of interstitial channels. The filling behaviour is in correlation with the current-time transient

for gold deposition into the colloidal crystal template with 373 nm PMMA sphere size. By increasing the time of the electrodeposition, the level of gold-infilling can be controlled until it reaches the surface of the PMMA colloidal crystal template. In the event of increased electrodeposition time, overfilling above the top surface of the PMMA opal can occur.

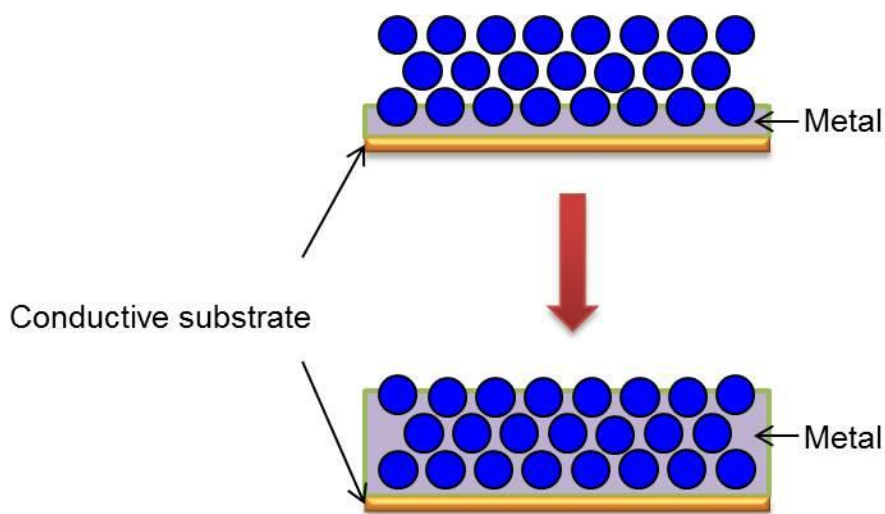


Figure 5.2 A schematic diagram of metal infiltration into colloidal crystal templates

5.2.2 Inverted Structure of Gold

Well-ordered gold metal macroporous structures were formed on the conductive substrate, which exhibited strong opalescence under light illumination, confirming the success of the inversion procedure. Figure 5.3 shows SEM images of the top surface of an inverted gold structure on the ITO substrate produced using an electron potential of -1.0 V (Ag/AgCl), for 1000s. During this process, gold ions in the electroplating solution

Chapter 5

are induced to migrate by the applied potential and accumulate onto the working electrode (substrate) in 1000s. In this case 1000s was insufficient to completely infill the crystal template. From these surface views, the symmetry of the spherical holes in the crystal can be observed along the [111] direction. Typically within an FCC structure each cavity formed by the PMMA particles has three dark spots corresponding to the contact points with three particles in the layer below.

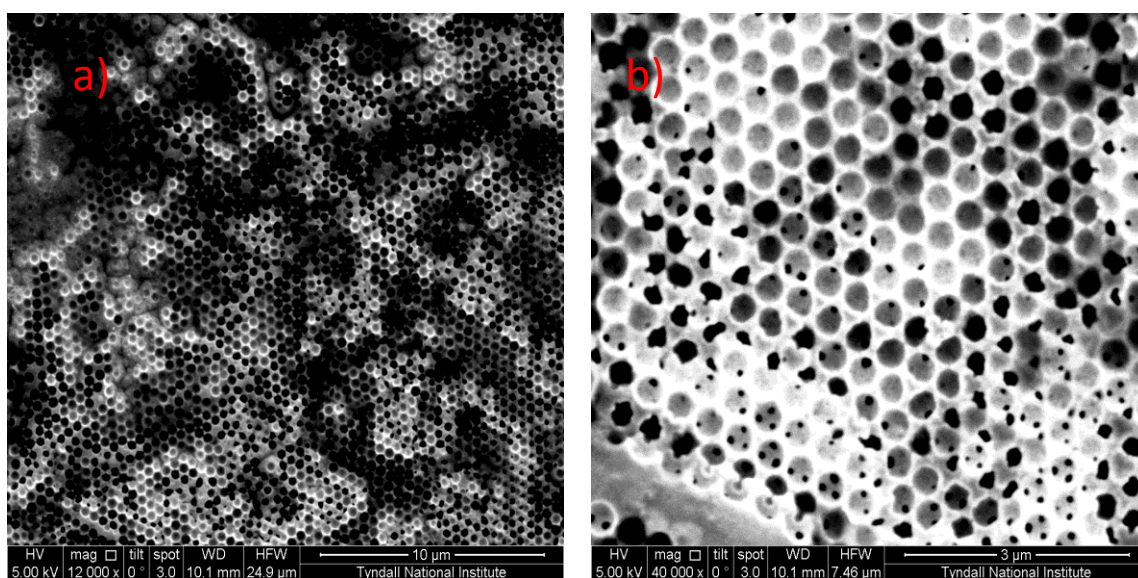


Figure 5.3 SEM images of the upper surface of an inverted gold film on ITO substrate prepared at an electron potential of -1.0 V (Ag/AgCl) for 1000 s. Magnifications a) 12,000x b) 40,000x

Figure 5.4 shows a cross sectional SEM image of a 3D ordered inverted gold structure produced using an electron potential of -1.0 V (Ag/AgCl) for 1500 s. It shows how increasing electrodeposition time to 1500s resulted in the formation of a gold over-

layer above the template. In general, the height of gold-filling into the PMMA colloidal crystal template increases with increasing electrodeposition time.

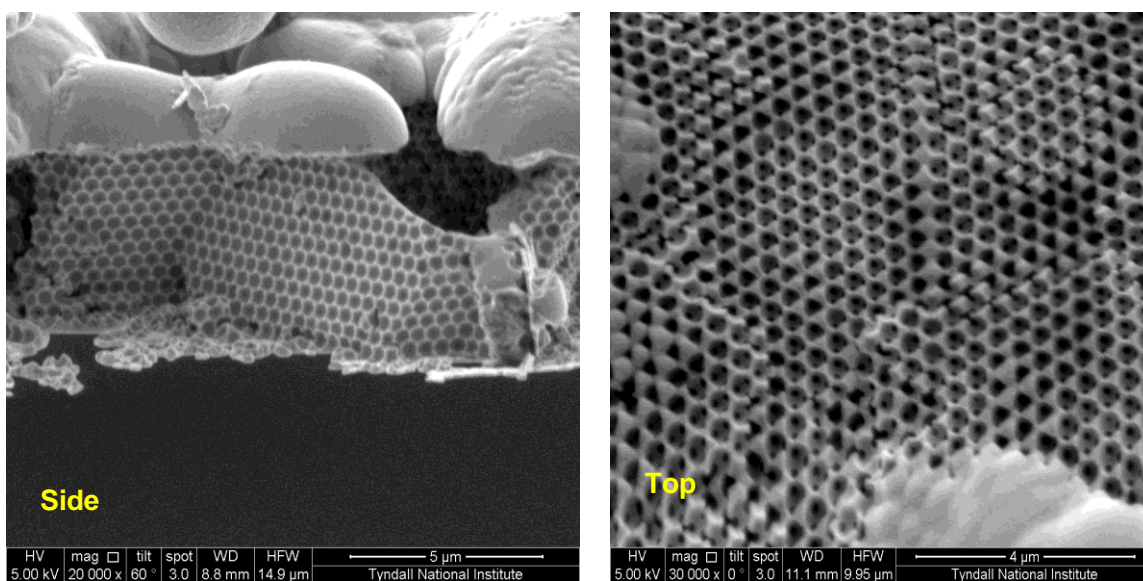


Figure 5.4 SEM images of a side view and surface of an inverted gold film on ITO substrate prepared at an electron potential of -1.0 V (Ag/AgCl) for 1500s, including gold over filling layer.

5.3 Preparation of Nickel Infiltrated Opal and Inverse Opal

5.3.1 Nickel Infiltration

The experiment set up was the same as shown in Figure 5.1, but replacing the gold solution with a nickel solution previously described in Chapter 2.

5.3.2 Inverted Nickel

After the nickel electrodeposition process, the PMMA colloidal crystal template was removed by acetone, followed by calcination at 400°C. Finally, well-ordered nickel

Chapter 5

macroporous structures with hollow sphere arrays were formed on the conductive substrate. All samples exhibited strong opalescence under light illumination, confirming the success of the inversion procedure. Figure 5.5 shows a monolayer of inverted nickel structure on the gold substrate was produced via electrodeposition process at -1.0 V (Ag/AgCl), for 100s. During this process, nickel ions in the electroplating solution are induced to migrate by the applied potential and accumulate onto the working electrode (substrate) in 100s. To produce thicker nickel inverted films, longer electrodeposition times were required.

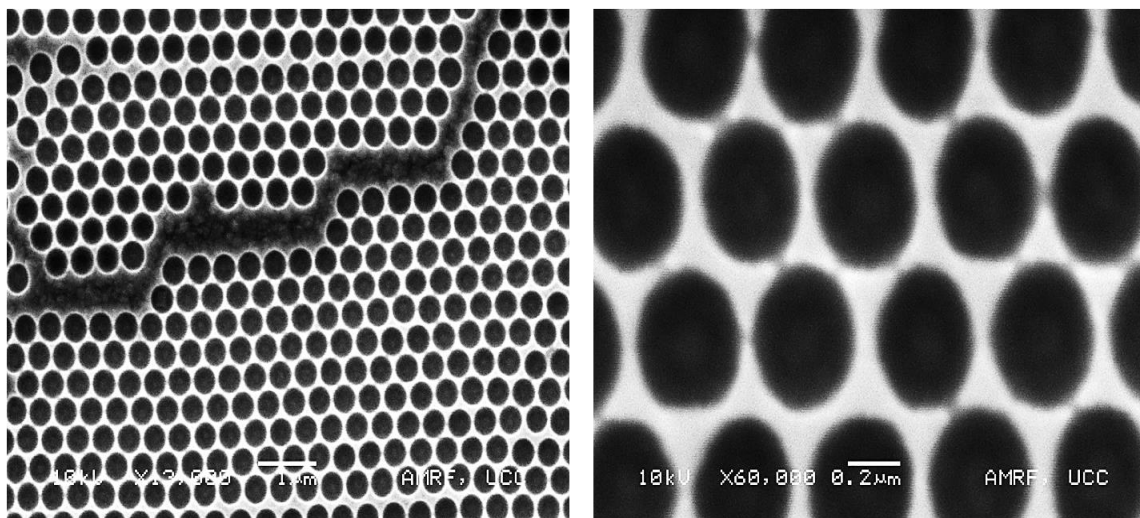


Figure 5.5 SEM surface images of an inverted nickel film on a gold substrate

Figure 5.6 shows SEM images of the surface of a 3D ordered nickel structure formed by depositing at -1.0 V for 1000s, into a PMMA colloidal crystal template with diameter 373 nm colloidal particles using a gold substrate. From the top view, the symmetry of the spherical holes which are located above three neighbouring hollow sites

Chapter 5

in the crystal can be observed along the [111] direction. Each cavity formed by the PMMA particles has three dark spots corresponding to the contact points with the three particles in the layer below.

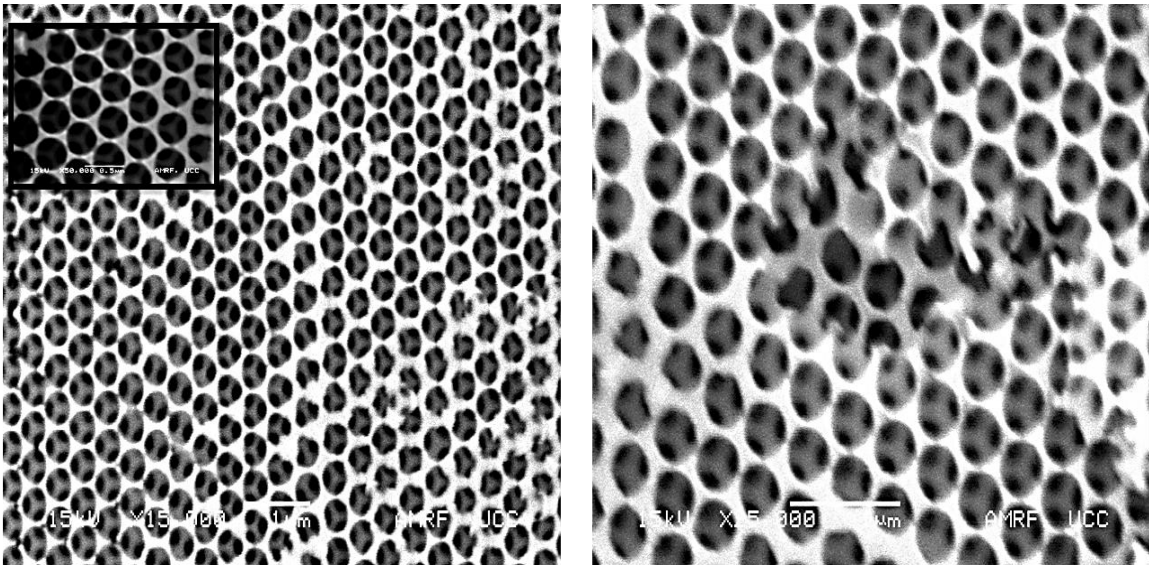


Figure 5.6 SEM images of the surface of a 3D ordered nickel macroporous structure

Side views of the same 3D macroporous structure, consisting of several spherical void layers are shown in Figure 5.7. Each air hole is surrounded by six spherical voids showing a hexagonal close-packed network of circular holes. In general, the height of nickel-filling into the PMMA colloidal crystal template increases with increasing electrodeposition time.

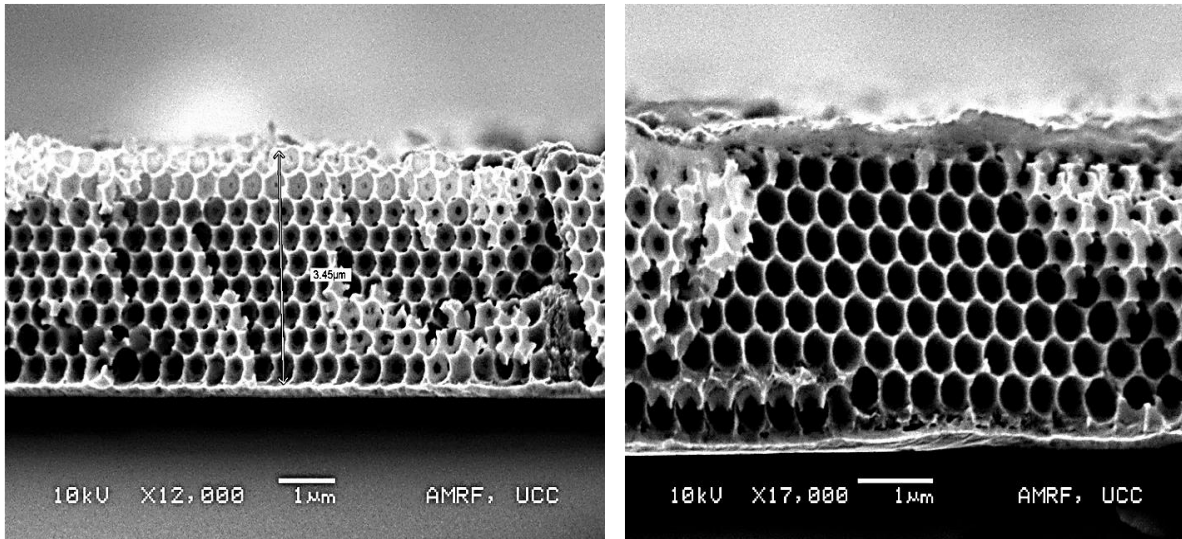


Figure 5.7 SEM images of the cross section of a 3D ordered nickel macroporous structure

5.4 Optical Properties

Figure 5.8 presents the transmittance and reflectance spectra of three types of opal structures prepared. The behaviour of light in the gold infiltrated opal structure, and the inverted opal with air spheres surrounded by gold network is completely different compared to that of the original PMMA opal template. The PMMA template shows a definite PBG (transmittance minimum at 978 nm at normal incidence) corresponding to the first order (111) Bragg reflection. The infiltration of gold suppresses the Bragg reflections as compared to the bare template structure, possibly as a result of coupling to the gold plasmon resonances, although specific features that might be directly assigned to the plasmons are not obvious. It is possible that light may be emerging in directions that were not accessible using our normal sampling geometry. Only reflectance features could

Chapter 5

be measured as a result of this, which shows only diminished diffraction resonance features compared to the template structure (Figure 5.8b) [6].

The gold inverse opal structure shows diminished but broad spectral bands spanning between 545 – 875 nm. The spectrum measured at 10° incidence shows a broad band with two maxima at 715 nm and 640 nm (Figure 5.8c), which on increasing the incidence angle first shifts to lower wavelengths (until 35°) and then shifts to longer wavelengths. We believe this feature may be an indication of coupling of plasmonic resonances with the air opal photonic band gap. The band diminishes on increasing the angle of incidence and becomes almost unobservable above 55° . This is because the light is required to travel a longer path through the structure at the higher angles which results in more attenuation with the longer distances compared to the lower angles of incidence.

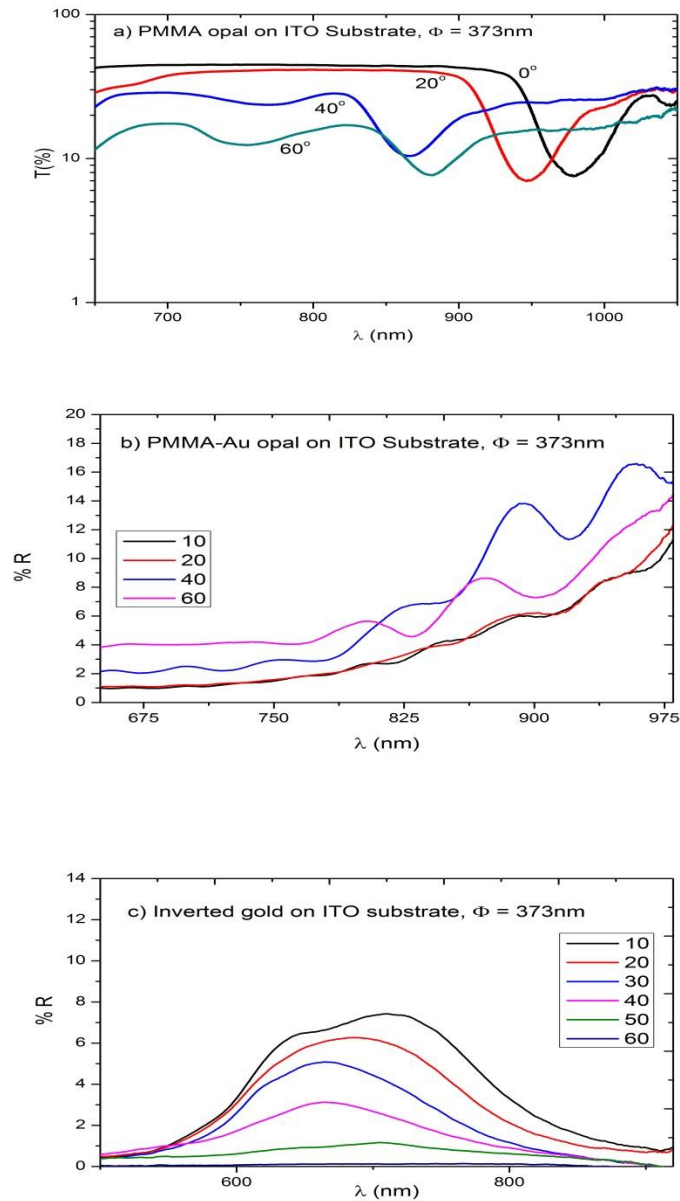


Figure 5.8 Angle-resolved spectra from (a) transmittance through the PMMA template on the ITO substrate, (b) reflectance from the gold infiltrated PMMA opal and (c) reflectance from the gold inverse opal.

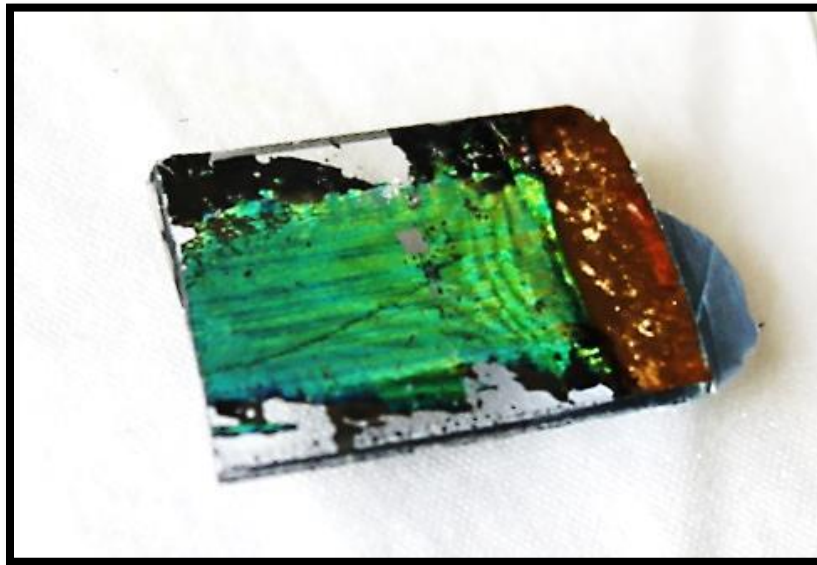


Figure 5.9 Nickel inverted structure film on gold substrate

Figure 5.9 shows an inverted nickel structure on a gold substrate. Opalescent colours are seen which is crucial to the applications of these materials. However, it proved very difficult to obtain the optical response from this nickel inverted film even though the opalescent colours are observable to the naked eye.

5.5 Conclusions and Future Work

In summary, we have prepared PMMA-gold MDPC structures with a continuous dielectric-metal interface throughout the 3D structure by an optimized electrodeposition process. While proving the effectiveness of the described method for the preparation of completely infilled 3D MDPCs, these robust MDPC structures present interesting

prototype structures for fundamental optical investigations. The optical properties, though not fully understood at this point of time, should be explored in more detail in any future work.

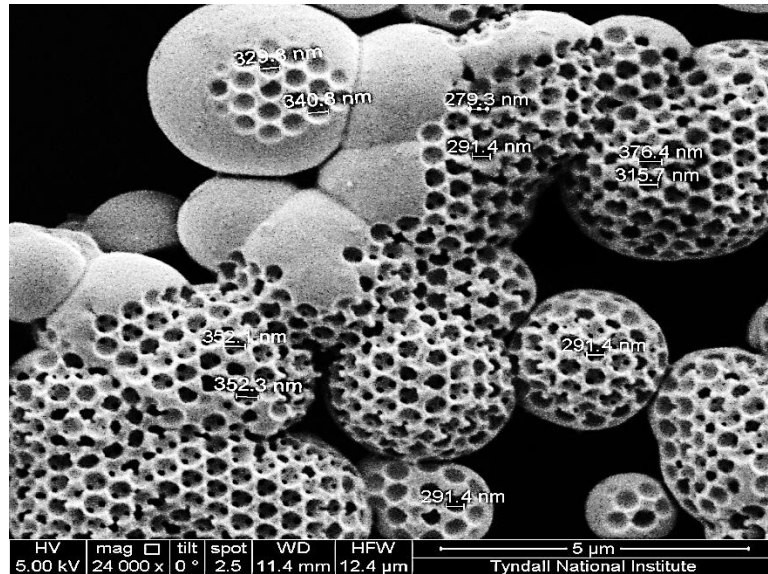


Figure 5.10 SEM image of the unique morphology of gold inverse opal

One of the main problems faced during gold electrodeposition was that the films easily peeled from the substrate, and that in some cases the gold inverted structure showed a unique morphology, the gold tending to form ‘florets’, seemingly pulling the PMMA crystal template into these shapes during the electrodeposition process (Figure 5.10). The origins of these structures are not clear. It may be that they arise from geometrical factors associated with the shape presented by the template or that the growth process is somehow influenced by factors such as gas evolution. The gold films tended

to curl upon peeling from the ITO substrate, to the extent that opalescence was no longer visible. This effect has recently been described by Xu *et al.* [7] who concluded that it could be due to the greater malleability of gold relative to that nickel. Jiang *et al.* [8] reported the same situation in films made with an electroless method. Nickel in particular makes tough and sturdy free-standing films, while the gold films often curled and fragmented into smaller pieces. Alternatively, in order to fabricate high quality inverted gold structures focus could follow co-crystallisation processes. Co-crystallisation is a simple process whereby mixing Au NPs, hydrolysed TEOS and PMMA spheres co-crystallise via evaporation deposition which is able to produce high quality long range ordered structures with greater strength. Removal of the PMMA template would produce robust silica - Au NPs inverse structure. As a result, peeling from the substrate could be avoided compared to the electrochemical process presented here. Co-crystallisation would make a different material to the electrodeposition process, which is an inverted gold structure, whereas co-crystallisation is an inverted gold-silica structure, which is discussed in more detail in Chapter 6.

FUTURE WORK

Electrodeposition of gold onto gold substrates should be investigated. This would remove the ITO-Au interface and may help in preventing peeling of the deposited gold structures.

Chapter 5

It might be of interest to grow gold inverse opal florets, and try to establish a growth mechanism whereby these structures are formed.

A more complete study of the rate of electrodeposition should be undertaken to establish accurate timescales for electrodeposition into PMMA opals film (before overfilling occurs)

References

1. Moroz, A., *Three-Dimensional Complete Photonic-Band-gap Structures in the Visible*. Physical Review Letters, 1999. **83**(25): p. 5274.
2. Zhang, J., Sun, Z. and Yang, B. *Self-assembly of photonic crystals from polymer colloids*. Current Opinion in Colloid & Interface Science, 2009. **14**(2): p. 103-114.
3. Zakhidov, A.A., Baughman, R.H., Iqbal, Z., Cui, C., Khayrullin, I., Dantas, S.O., Marti, J. and Ralchenko, V.G. *Carbon Structures with Three-Dimensional Periodicity at Optical Wavelengths*. Science, 1998. **282**(5390): p. 897-901.
4. Kamaev, V. *Optical Studies of Metallo-dielectric Photonic Crystals*. PhD Thesis. The University of Utah. 2007.
5. Shimmin, R.G., Vajtai, R., Siegel, R.W. and Braun, P.V. *Room-temperature assembly of germanium photonic crystals through colloidal crystal templating*. Chemistry of Materials, 2007. **19**: p. 2102-2107.
6. Miclea, T. P., Romanov, S.G., Torres, C.M., Liang, Z., Susa, A. and Caruso, F. *Towards 3D metal-dielectric photonic crystal. Optical characterization*. Mol. Cryst. Liq. Cryst., 2004. **415**: p. 211-219.
7. Xu, L., Zhou, W.L., Frommen, C., Baughman, R.H., Zakhidov, A.A., Malkinski, L., Wang, J.-Q. and Wiley, J.B. *Electrodeposited nickel and gold nanoscale metal meshes with potentially interesting photonic properties*. Chemical Communications, 2000. (12): p. 997-998.

Chapter 5

8. Jiang, P., Cizeron, J., Bertone, J.F. and Colvin, V.L. *Preparation of macroporous metal films from colloidal crystals*. Journal-American Chemical Society, 1999. **121**: p. 7957-7958.

Chapter 6: Colloidal Co-Crystallisation: A New Route to the Production of Three-Dimensional Metallodielectric Photonic Crystals

6.1 Introduction

Bottom-up colloidal crystallisation is a cost effective alternative for the fabrication of sub-micrometre 3D PhCs [1-4]. Most of the sub-micrometric 3D metallodielectric photonic crystals (MDPCs) that have been reported thus far have been produced by depositing the metallic component into the voids of self-assembled opal templates by means of methods such as chemical infiltration [5], atomic layer deposition (ALD) [6], chemical vapour deposition (CVD) [7] or by electrodeposition [8]. These methods have allowed the experimental validation of some of the unique optical properties of MDPC. Chemical infiltration and CVD methods, however impose a geometrical limitation for a complete metal infiltration. The templates almost always seemed to develop a metallic skin on the (111) surface closing the pores and inhibiting

further metal infiltration. While the electrodeposition method described in Chapter 5 allowed for the near-complete void filling and formation of inverse metallic opals, the optical properties, the reflectance/transmittance features, were almost completely dampened due to the optical properties of the extensive metallic structure that resulted, potentially limiting the studies of such materials to either 2D monolayers or just a few layers [8, 9].

In this chapter we show how 3D MDPC can be fabricated, with plasmonic functionalities, by a bottom-up co-crystallisation method. In particular, we report the fabrication of inverse MDPC by self-assembling metal and dielectric components from a single suspension followed by selective removal of the sacrificial template and we describe their enhanced PBG properties. The advantage of these integrated plasmonic-photonic materials stems from their novel optical functionalities that could be realized from the fundamental optical interactions between the photonic bands and the localized plasmonic resonances in the PhCs, which cannot otherwise be achieved by any natural/bulk systems [10]. We propose the use of a colloidal crystal matrix, with randomly distributed gold nanoparticles as an effective model for investigating the interesting fundamental optical properties of 3D MDPC. Of particular importance to this chapter is the tuning of PBG properties by the integrated plasmonic functionality. We show that the observed PBG features are derived from the coupling between the photonic bands and plasmonic resonance features of the metal inclusions. The effective integration of plasmonic functionalities could also pave the way to the fabrication of novel/improved

surface-enhanced Raman scattering (SERS) [11], sensing [12], enhanced photovoltaic and energy harvesting modules, [13, 14] to list but a few applications.

The inverse MDPC was prepared by controlled evaporation from an aqueous colloidal suspension containing the three components poly(methyl methacrylate) (PMMA) spheres, acid-hydrolysed tetraethylorthosilicate (TEOS) solution and pre-formed Au nanoparticles, followed by the removal of the PMMA template to form an inverted opal structure. The PMMA spheres ~373 nm were synthesized as reported in Chapter 3. The Au NPs were prepared by NaBH₄ reduction in the presence of citrate functionality as reported in Chapter 4. The citrate functionalisation was used to make the Au NPs (~20 nm) compatible with the colloidal suspension. The addition of TEOS produces the cementing component that holds the Au NPs together in the PhC backbone. This method could be extended to prepare almost any 3D composite PhCs that are active in the desired frequency window, provided the compatibility and size of the components are sufficiently controlled. The significance of the method is its ability to form robust MDPC structures over relatively large areas via a single self-assembly step.

6.2 SEM of Silica-PMMA Composite, Silica Inverse Opal and Metallo-dielectric Inverse Opal

SEM images of the fabricated 3D silica-PMMA composite and silica inverse opal are presented in Figure 6.1, while images of the MDPC are presented in Figure 6.2. The SEM images reveal the consistency of the inverse opal formed over large domain sizes,

Chapter 6

and the cross sectional image (see Figure 6.2) shows the 3D connectivity of the photonic crystal backbone. Embedding PMMA spheres with hydrolysed TEOS prevents cracking within the film, as the deposited silica cements the structure together. Hatton *et al.* [15] noted that cracking did begin to occur in these structures at approximately 20 layers thickness. By borrowing from this idea we have devised a new route for making MDPC by inclusion Au NPs into the TEOS sol as shown in Figure 6.2.

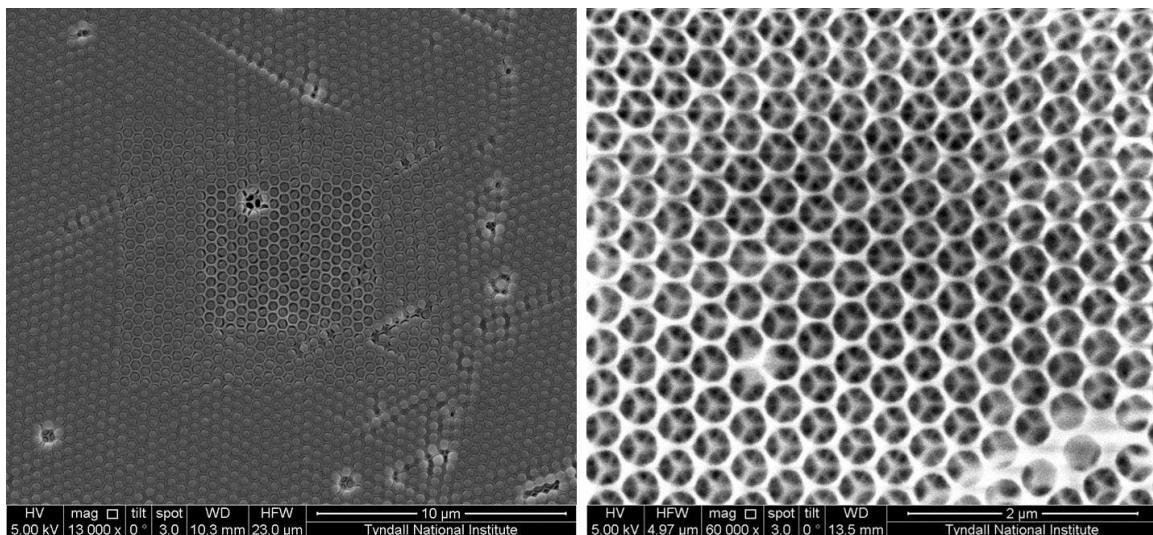


Figure 6.1 SEM images of surface views of large domain silica-PMMA composite (left) and silica inverse opal structure (right)

There are some areas that are cracked within these MDPCs, as shown in Figure 6.2 (left). This may be due to the inclusion of the Au NPs into PC backbone or because of the overall thickness [15].

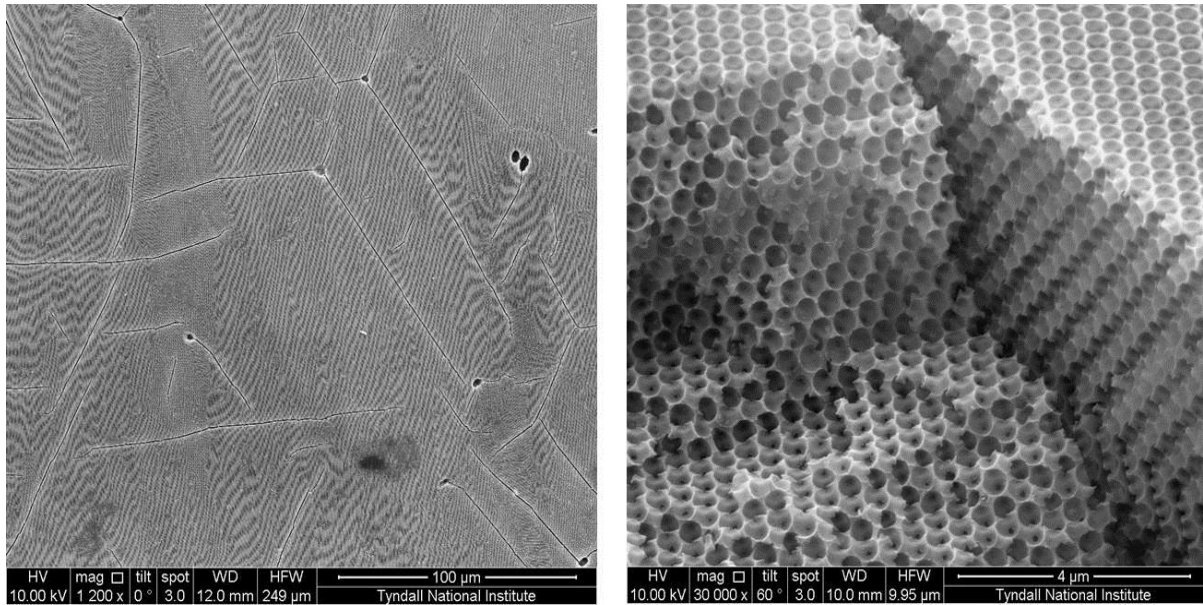


Figure 6.2 Top view of metallodielectric photonic crystal with 100 μm scale bar (left) and side view of the cross section MDPC with 4 μm scale bar.

Figure 6.3 shows a cross-sectional TEM image. The presence of gold nanoparticles can be seen randomly scattered throughout the skeleton of the MDPC.

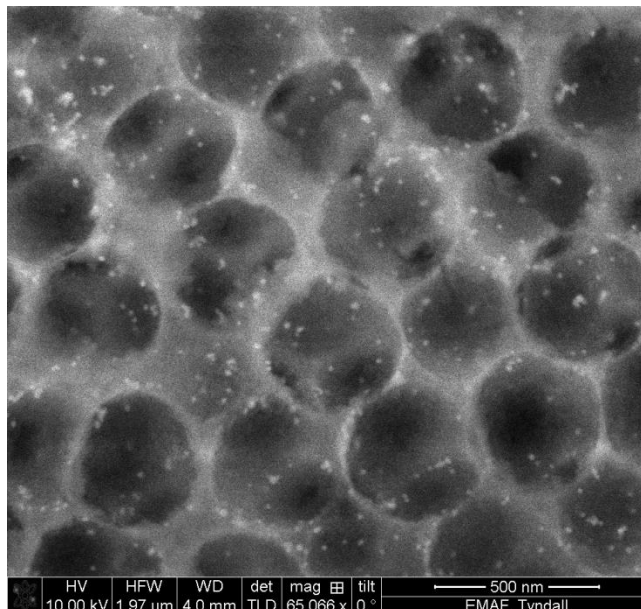


Figure 6.3 A TEM image of cross section of MDPC where the Au nanoparticles can clearly be seen.

6.3 Optical Properties

The optical properties of the 3D silica inverse opal were measured using an optical bench set-up for wavelengths ranging from 450 to 1100 nm. Figure 6.4 shows the anticipated shift in the Bragg peak that accompanies the increase in refractive index contrast upon inversion. The absolute reflectance and transmission spectrum of the metallodielectric inverted opal is presented in Figure 6.5 which shows the spectral data from two silica-Au inverse opal films (the second containing double the Au concentration of the first). The presence of a reflection band and corresponding transmission dip centred at 749 nm (less Au) is shifted to longer wavelengths, 779 nm for the higher gold concentration sample.

Chapter 6

The reflection and transmission spectra of a bare PMMA opal (control sample) made of 373 nm diameter spheres and the corresponding silica inverse opal (without Au NPs) are also presented for comparison. The bare PMMA opal shows a PBG centred at 964 nm and the silica inverse opal exhibits a stop band at 757 nm. While the PBG of silica inverse opal shifts to a shorter wavelength by 207 nm compared to the bare opal, the MDPC with less Au content shows a shift of 215 nm, while the higher gold concentration sample shows a shift of just 185. However, the silica inverse opal and MDPC both show an increase in the d spacing as compared to the PMMA bare opal with only 339 nm. This value is calculated from Figure 6.6 and given in Table 6.2. This is attributed to the co-crystallisation of the silica backbone (and Au NPs). A slight blue shift occurs with the inclusion of Au NPs into the silica backbone, of about 8 nm, as compared to silica inverse opal without gold. This is possibly due to the action of the imaginary component of the metal refractive index in this spectral region. A red shift ($\Delta 30\text{nm}$) was observed for the PBG for the MDPC with double the gold content (compared to the lesser gold addition MDPC) is therefore attributable to the increase in the lattice spacing as a result of the integration of Au NPs in the silica backbone.

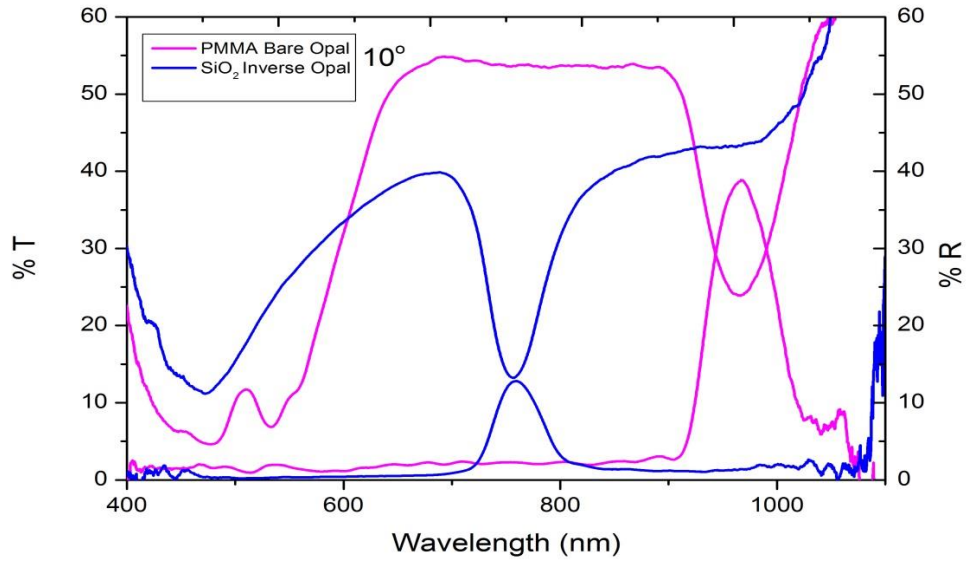


Figure 6.4 Reflectance and transmission peaks of a bare opal and silica inverse opal

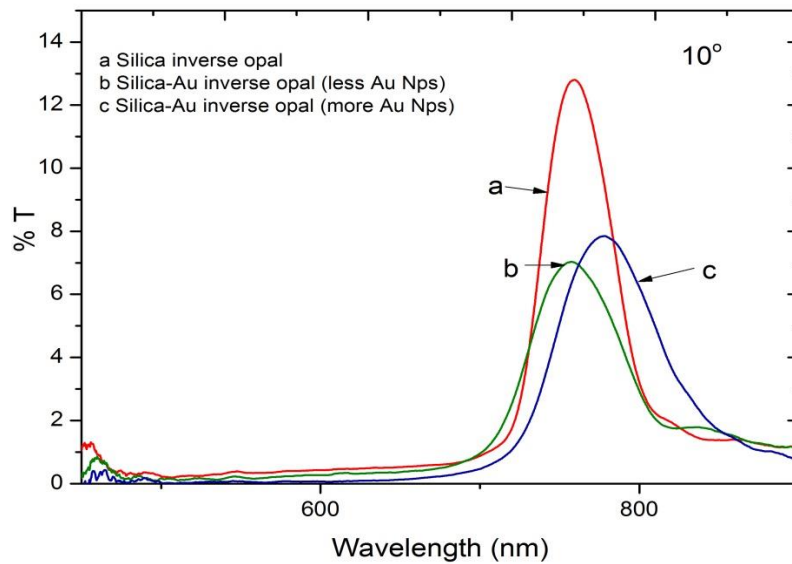


Figure 6.5 Reflectance peaks of a silica inverse opal and MDPCs.

Chapter 6

Table 6.1 Wavelength maximum value from Bragg peak, difference wavelength from bare opal and inverse SiO₂

Samples	λ_{\max} measured from Bragg peak $\theta = 10^\circ$	$\Delta\lambda$ Change from bare opal	$\Delta\lambda$ Change from inverse SiO₂
PMMA bare opal	964	-	-
Silica inverse opal	757	207	-
Silica-Au inverse opal (less Au)	749	215	-8
Silica-Au inverse opal (More Au)	779	185	+22

Chapter 6

Table 6.2 Calculated lattice d-spacings, diameters, D and η_{eff} from plotted angle-resolved optical spectra

Samples	d_{111} calculated graph plotted (λ^2 vs $\text{Sin}^2\theta$) (nm)	D *Calculated (nm)	D SEM (nm)	η_{eff} calculated	Diameter calculated from Bragg peak & η_{eff} value
PMMA bare opal	339	415	373	1.43	415
Silica inverse opal	356	437	428	1.07	439
Silica-Au inverse opal (less Au)	343	420	470	1.12	414
Silica-Au inverse opal (More Au)	348	427	444	1.13	427

*Diameter D is calculated from $d_{111} = D\sqrt{2/3}$; the calculated D of the PMMA spheres is larger than the diameter obtained from SEM measurements. This is probably due to shrinkage of the PMMA spheres under the electron beam.

Other notable features of the reflectance spectra are the difference in intensities amongst the samples. Comparing the 4 samples, the PMMA bare opal showed the most intense band of ~35% reflectance. In comparison the silica inverse opal had ~18% reflectance, and for the two MDPCs samples the reflectance values were both approximately ~8-9%.

Chapter 6

It is known that the intensity of the Bragg reflection from a PhC depends directly on the structural ordering as well as the thickness (number of layers). The bare PMMA, silica inverse opal and MDPCs films were made with different thicknesses, 15-18 layers (calculated from Fabry-Perot fringes of the bare PMMA spectra, while the others were measured from SEM images). The relatively low reflection intensity of ca. 18% for the silica inverse opal illustrates the ability of the co-crystallisation process to prepare samples which display an easily observable Bragg peak, although the quality of the sample is far below that which can be achieved for other types of photonic crystal. Subsequently the incorporation of Au NPs appears to further degrade the quality of the structure and perhaps introduces a certain amount of disorder during the co-crystallisation. The emphasis of this work was on the fabrication of MDPCs by a co-crystallisation method, with incorporated nanoparticles. Pre-hydrolysed TEOS, in the colloidal suspension, does not significantly modify the crystallisation process, but enables the effective integration of the Au NPs into the photonic crystal backbone. This use of TEOS was examined by attempting to prepare photonic crystals without pre-hydrolysed TEOS (keeping all other parameters the same). We could not produce a robust 3D structure with significant ordering when assembling without the TEOS precursor solution. The role of the silica network in cementing the metal NPs also makes this method versatile since the process is more dependent on the thermodynamics of the particles in suspension rather than on their physiochemical properties allowing it to be a general strategy for making multifunctional interconnected porous structures.

Chapter 6

Interestingly, approx. 8% reflectance was exhibited by the MDPC formed with 18 layers thickness (measured from SEM images). This is consistent with the argument given above since it further suggests increased disorder in structures that contain the Au NPs as compared to the bare PMMA opal or the silica inverted structure. Structures possessing fewer layers would be expected to show lower reflectivity [16] but this is not the case here, as 18 layers should be more than enough for the completion of the photonic band structure. This considerable decrease in reflectance compared to the inverse opal may be attributed to Au NPs absorbing a part of the light. Metals are very absorptive, especially at optical frequencies. That is why the most early proposed metallic PhCs operated at microwave frequencies where absorption is smaller [17, 18]. This situation can be supported when characterising the MDPC sample with the addition greater gold content, the reflected light was difficult to observe during sample measurement. The reduction in intensity for the MDPC from that of silica inverse opal may be attributed to the presence of inherent disorder and Au plasmonic absorption. This leads us to hypothesize that the Au NPs may be distributed randomly throughout the photonic crystal backbone allowing the development of band gap in these structures, while also enabling possible weak plasmonic coupling between them. The TEM image presented in Figure 6.3 appears to confirm this hypothesis, although some aggregation of the Au NPs cannot be ruled out.

The evolution of the PBG developed in the silica-Au inverse MDPC seems to be determined by the interplay between the plasmonic absorption, scattering and the

plasmonic-coupling by the Au NPs distributed randomly throughout the structure, although clearly more work is required in order to confirm or deny this rather general statement.

The reflectance of the PMMA opal, silica inverse opal and the MDPC measured at an incident angle, θ , of 10° show an angle-dependent shift towards shorter wavelengths with increasing angle, to 90° . This observation is consistent with the expected behaviour for a photonic crystal in terms of the Bragg-Snell relationship. By altering the angle of incidence (θ), the effective refractive index (η_{eff}) and the inter planar spacing (d) can be determined as described in previous chapters [19, 20].

The correlation with the Bragg-Snell relationship is further confirmed by fitting the data points obtained to a plot of the square of the wavelength maximum (λ_{max}^2) for the stop bands recorded at varying angle of incidence angle, θ , against $\sin^2\theta$ (Figure 6.6). The linear fit shown in Figure 6.6 is in agreement with the Bragg-Snell relationship. Using the plot shown in Figure 6.6, η_{eff} can be calculated, and the silica inverse opal was found to have a reduced η_{eff} compared to PMMA opal, from 1.43 to 1.07. For the MDPC this was less reduced, to 1.12 most likely due to the presence of the Au NPs. However, a note of caution must be introduced here. While the plots appear to be linear, they are certainly not as linear as others obtained from simpler PhC systems. The R^2 values for the lines are shown in Figure 6.6. These demonstrate a degree of departure from the Bragg-Snell law that needs further clarification via future studies.

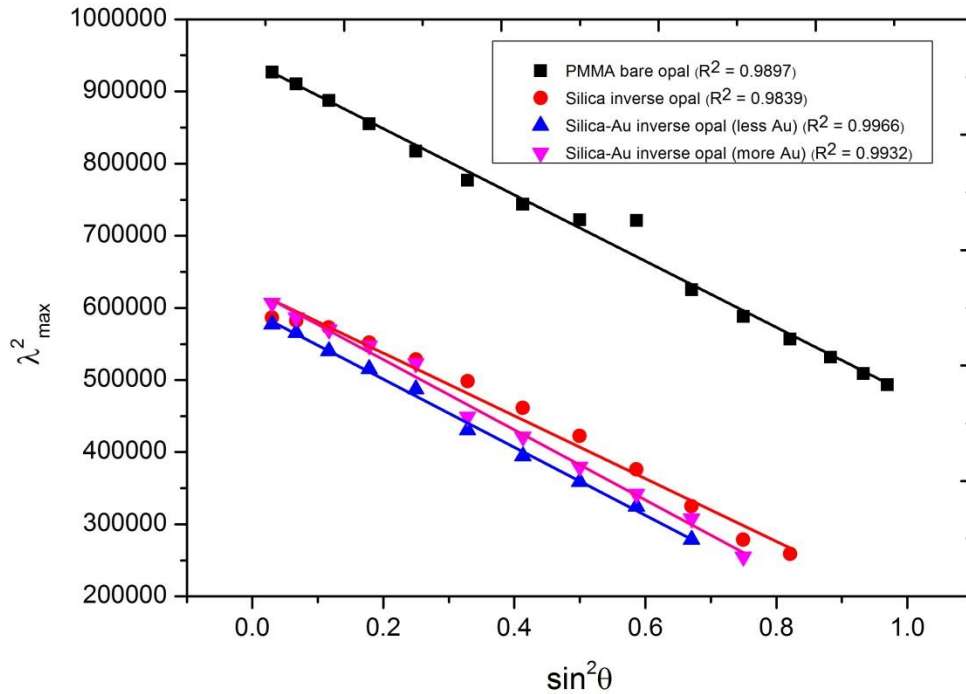


Figure 6.6 Plot of λ_{\max}^2 vs $\sin^2\theta$ showing the roughly linear fits based on PMMA bare opal, silica inverse opal and MDPC reflectance measurements, respectively. A degree of departure from the Bragg-Snell law is implied from these data.

6.4 Conclusions

We have developed a simple method capable of producing MDPC structures via a co-crystallisation deposition method. We have shown via preliminary experiments that different optical properties can be developed by tuning the concentration of Au NPs, where higher Au loading suppresses transmission dip and shifts the Bragg peak to higher wavelengths. Future work should also focus on the use of different metal nanoparticles to

Chapter 6

suit the desired applications. This method is also used as a route to produce large crack-free areas within these films (below a thickness level of approximately 20 deposition layers). Some degree of departure from the Bragg-Snell law is implied from the data presented which should be examined in more detail in the future.

References

1. López, C. *Materials aspects of photonic crystals*. Advanced Materials, 2003. **15**: p. 1679-1704.
2. Jiang, P., Bertone, J.F., Hwang, K.S. and Colvin, V.L. *Single-crystal colloidal multilayers of controlled thickness*. Chem. Mater., 1999. **11**: p. 2132-2140.
3. Philipse, A.P. *Solid opaline packings of colloidal silica spheres*. J. Mater. Sci. Lett, 1989. **8**: p. 1371.
4. Van Blaaderen, A., Ruel, R. and Wiltzius, P. *Template directed colloidal Crystallization*. Nature, 1997. **385**: p. 321.
5. Shimmin, R.G., Vajtai, R., Siegel, R.W. and Braun, P.V. *Room-temperature assembly of germanium photonic crystals through colloidal crystal templating*. Chemistry of Materials, 2007. **19**: p. 2102-2107.
6. Povey, I.M., Whitehead, D., Thomas, K., Pemble, M.E., Bardosova, M. and Renard, J. *Photonic crystal thin films of GaAs prepared by atomic layer deposition*. Applied Physics Letters, 2006. **89**(10): p. 104103-3.
7. Ibisate, M., Golmayo, D. and López, C. *Silicon direct opals*. Advanced Materials, 2009. **21**(28): p. 2899-2902.
8. Kassim, S., Padmanabhan, S.C., Salaun, M. and Pemble, M.E. *PMMA-gold metallodielectric photonic crystals and inverse opals: preparation and optical properties*. AIP Conference Proceedings, 2011. **1391**(1): p. 263-265.

Chapter 6

9. Kuzmiak, V., Maradudin, A.A. and Pincemin, F. *Photonic band structures of two-dimensional systems containing metallic components*. Phys. Rev. B, 1994. **50**: p. 16835-16844.
10. Ward, A.J., Pendry, J.B. and Stewart, W.J. *Photonic dispersion surfaces*. J. Phys.: Condens. Matter, 1995. **7**: p. 2217-2224.
11. Jackson, J.B. and Halas, N.J. *Surface-enhanced Raman scattering on tunable plasmonic nanoparticle substrates*. Proceedings of the National Academy of Sciences, 2004. **101**(52): p. 17930-17935.
12. Tessier, P.M., Velev, O.D., Kalambur, A.T., Lenhoff, A.M., Rabolt, J.F. and Kaler, A.W. *Structured metallic films for optical and spectroscopic applications via colloidal crystal templating*. Advanced Materials, 2001. **13**(6): p. 396-400.
13. Ho, K.M., Chan, C.T. and Soukoulis, C.M. *Existence of a photonic gap in periodic dielectric structures*. Physical Review Letters, 1990. **65**(25): p. 3152-3155.
14. Zhao, Y., Zhang, X.J., Ye, J., Chen, L.-M., Lau, S.-P., Zhang, W.-J. and Lee, S.-T. *Metallo-dielectric photonic crystals for surface-enhanced Raman scattering*. ACS Nano, 2011. **5**(4): p. 3027-3033.
15. Hatton, B., Mishchenko, L., Davis, S., Sandhage, K.H. and Aizenberg, J. *Assembly of large-area, highly ordered, crack-free inverse opal films*. Proceedings of the National Academy of Sciences of the United States of America, 2010. **107**(23): p. 10354-10359.

16. Bertone, J.F., Jiang, P., Hwang, K.S., Mittleman, D.M. and Colvin, V.L. *Thickness dependence of the optical properties of ordered silica-air and air-polymer photonic crystals*. Physical Review Letters, 1999. **83**(2): p. 300-303.
17. Ozbay, E., Temelkuran, B., Sigalas, M., Tuttle, G., Soukoulis, C.M. and Ho, K.M. *Defect structures in metallic photonic crystals*. Applied Physics Letters, 1996. **69**(25): p. 3797-3799.
18. Brown, E.R. and McMahon, O.B. *Large electromagnetic stop bands in metallodielectric photonic crystals*. Applied Physics Letters, 1995. **67**(15): p. 2138-2140.
19. Waterhouse, G.I.N. and Waterland, M.R. *Opal and inverse opal photonic crystals: Fabrication and characterization*. Polyhedron, 2007. **26**(2): p. 356-368.
20. Schrodin, R. and Balakrishnan, N. *Inverse opal photonic crystals a laboratory guide*. 2001, University of Minnesota. p. 1-32.

Chapter 7: A Bottom-Up Fabrication Method for the Production of Visible Light Active Photonic Crystals

(Sibu C. Padmanabhan, Keith Linehan, Shane O'Brien, Syara Kassim, Hugh Doyle, Ian M. Povey, Martyn E. Pemble, "A bottom-up fabrication method for the production of visible light active photonic crystals", J. Mater. Chem. C, 2014, 2(9): p. 1675-1682)

Figures 1 (f) & (h) are shown enlarged for clarity in Appendix C.

Contributions:

Syara Kassim	Prepared PMMA spheres and contribute the idea to fabricate silica inverse opals
Keith Linehan	Prepared silicon nanocrystals and characterized them
Shane O'Brien	Deposited Si nanocrystals by AACVD
Ian Povey, Martyn Pemble & Hugh Doyle	Suggested corrections on the paper
Michael Schmidt	Did characterisation on high resolution transmission electron microscope (HRTEM) and focus ion beam (FIB)
Sibu Padmanabhan	Conceived the idea, prepared inverse opals, SEM and wrote the paper

A bottom-up fabrication method for the production of visible light active photonic crystals†

Cite this: DOI: 10.1039/c3tc31994f

Sibu C. Padmanabhan,^{*ab} Keith Linehan,^a Shane O'Brien,^a Syara Kassim,^{ac} Hugh Doyle,^a Ian M. Povey,^a Michael Schmidt^a and Martyn E. Pemble^{*ab}

A method which combines polymer particle assembly, chemical infiltration and etching with an aerosol assisted deposition process is described for the fabrication of 3D inverse opal (IO) structures with sub-micron periodicity and precision. This procedure not only overcomes limitations associated with slow, expensive micro-fabrication methods but also permits the tuning of refractive index contrast *via* the direct incorporation of photonically-active, preformed, tailored silicon nanostructures. It is demonstrated that this approach can be used to modify the photonic band gap (PBG) by effectively depositing/patterning optically active silicon nanocrystals (ncSi) onto the pore walls of a 3D inverse opal structure. This simple, yet effective method for preparing functional complex 3D structures has the potential to be used generically to fabricate a variety of functional porous 3D structures that could find application not only in new or improved photonic crystal (PC) devices but also in areas such as catalysis, separation, fuel cells technology, microelectronics and optoelectronics.

Received 9th October 2013
Accepted 27th December 2013

DOI: 10.1039/c3tc31994f

www.rsc.org/MaterialsC

Introduction

Colloidal PCs, often also referred to as synthetic opals due to their resemblance to natural opal gemstones in certain cases, are periodic dielectric structures that possess photonic stop-bands which arise by virtue of their dielectric periodicity.^{1–7} Depending on the frequency range where the stop-band is formed, photonic crystals can control the propagation of relevant photons. While the propagation of photons of frequency within the stop-band is forbidden, all other photons are allowed to propagate.^{8–13} In an ideal case, the lattice spacing, and the dielectric contrast of the composite determine the photonic stop-band properties.^{14–16} Tuning of these parameters has been shown to improve the stop-band properties to the extent to which the stop-band formed is able to restrict photon propagation within the whole of the optical Brillouin zone, *i.e.* irrespective of the propagation direction. Such a stop-band is also known as full PBG in contrast to the more directional pseudogaps which are often observed for lower refractive index contrast media.^{17–20} Although periodic structures with full PBGs have been realized at the longer wavelength region (above near-infrared) of the electromagnetic spectrum using 3D PC

structures,^{21–25} the realization of full PBGs at the visible light frequencies still remains a challenge. The major bottlenecks hindering its successful realization are (i), the inherent limitation and high costs associated with the use of top-down micro-fabrication approaches in creating 3D structures with precise sub-micron periodicity and (ii), the unavailability of suitable high dielectric materials having negligible absorption in the visible frequency range.

The generic aim of most photonic crystals research is to achieve control over the manipulation and utilization of photons in order to enable novel technological platforms.^{26–34} While control over spontaneous emission is at the heart of many potential photonic crystal-based technologies,^{3,25,35–37} more and more exciting avenues are driving the research into new application areas.^{27,38–40} For example the use of photonic crystals in solar cells and sensors, and also the effective utilization of diffuse scattering by photonic crystals to enhance LED lighting efficiency. This latter application is one example of this technology where the formation of a complete PBG is not a specific requirement.^{33,41}

Of direct relevance to this type of application we show here how the two-in-one functional properties of pre-formed silicon nanocrystals – namely their high refractive index and tuneable photoluminescence (PL) emission, can be effectively utilized to improve first the visible light PBG properties as evidenced by the broadening of the stop-band and the overlap of specific features in the reflectance spectra and then to demonstrate the modification of PL emission in the presence of the altered PBG. The method presented here is straightforward and potentially scalable to large area fabrication of robust 3D inverse opal

^aTyndall National Institute, University College Cork, Lee Maltings, Cork, Ireland. E-mail: martyn.pemble@tyndall.ie; Fax: +353 214904467; Tel: +353 214906456

^bDepartment of Chemistry, University College Cork, College Road, Cork, Ireland

^cUniversiti Malaysia Terengganu, Kuala Terengganu, Terengganu, Malaysia

† Electronic supplementary information (ESI) available: SEM images of ncSi-SiO₂, large area SEM image of SiO₂, reflection/transmission spectra of ncSi-SiO₂ at 60° incidence and the UV-Vis absorbance spectrum of ncSi solution. See DOI: 10.1039/c3tc31994f

structures. Importantly, the method described^{42,43} does not require the use of any complicated deposition, annealing⁴³ and etching processes.

Experimental

Synthesis of PMMA colloidal particles

Methyl methacrylate (MMA) and potassium persulfate were purchased from Aldrich. Millipore water (18.2 MΩ cm) was used as the medium of reaction. The PMMA colloid of mean particle size 290 nm (relative standard deviation < 5%) was prepared by an emulsifier-free emulsion polymerization in water in the presence of the initiator potassium persulfate at a reaction temperature of 80 °C. The reaction mixture was kept stirring throughout the reaction at a speed of 500 RPM. Millipore water was first bubbled with nitrogen gas for 20 minutes. After this, 15 mL of MMA was added under nitrogen atmosphere followed by 0.19 g of potassium persulfate. The solution was then heated to 80 °C and maintained at this temperature for 40 minutes for the completion of the polymerization. After the polymerization reaction, the colloid was centrifuged and washed 5–6 times using Millipore water and used.

Preparation of silica inverse opal (SIO) templates

The SIO templates were prepared by a controlled evaporation self-assembly method, slightly modified from the previous reports^{44,45} in order to combat the PMMA swelling issue, from a colloidal dispersion containing PMMA particles and pre-hydrolyzed tetraethyl orthosilicate (TEOS), onto a clean glass substrate placed in a slanted position in a glass vial. Precisely, 0.1 V% (8 mL) of PMMA particles of mean particle size 290 nm was allowed to evaporate at a temperature of 65 °C in presence of 0.16 mL of pre-hydrolyzed TEOS precursor solution prepared by mixing acetic acid, TEOS and Millipore water in the volume ratio (1 : 1 : 8). Acetic acid here plays a dual role as chelating agent and acid catalyst for the polymeric hydrolysis of the TEOS precursor to form a homogeneous silica sol.^{46,47} The use of acetic acid also helps to avoid the use of ethanol which induces swelling of the PMMA particles. The formed opal is then immersed in acetone for 2 h with changing the solution a couple of times for a complete dissolution of the PMMA template to obtain the inverse opals.

The opal templates were then characterized using a Perkin-Elmer Lambda 950 spectrophotometer for their PBG properties. Angle-resolved reflection spectra of the samples were acquired at varying angles of incidence, θ , with respect to the (111) surface normal from 8° to 65° for the wavelength range of 200–2000 nm. For that, the samples were illuminated by a collimated beam of UV/Vis/NIR light with a spot diameter of 5 mm × 5 mm obtained from pre-aligned tungsten-halogen and deuterium sources. A combination of high performance Peltier-cooled InGaAs and PbS detectors were used for signal detection.

Chemical synthesis and purification of silicon nanocrystals

The synthesis of the Si nanocrystals is adapted from the method reported by Tilley and co-workers.⁴⁸ All reagents and solvents

were purchased from Sigma-Aldrich Ltd. and used as received. In nitrogen filled glove-box, 0.00274 mol of tetraoctylammonium bromide (TOAB) was dissolved in 100 mL anhydrous toluene. 1.0 mL (0.0087 mol) SiCl₄ was added to the above solution and the mixture was left to stir for 30 min. Si nanocrystals were then formed by the drop wise addition of 6 mL of 1 M lithium aluminium hydride in THF over a period of 2 min. The solution was then left to react for 2.5 h. The excess reducing agent was then quenched with the addition of 60 mL methanol, upon which the dispersion became transparent. At this stage of the reaction, the silicon nanocrystals are terminated by hydrogen and encapsulated in a TOAB micelle. Chemically passivated nanocrystals were then formed by modifying the silicon-hydrogen bonds at the surface through addition of 200 μL of a 0.1 M H₂PtCl₆ in isopropyl alcohol as a catalyst followed by 6 mL of allylamine. After stirring for 2.5 h, the Si nanocrystals were removed from the glove box and the organic solvent was removed by rotary evaporation. The resulting dry powder (consisting mainly of surfactant) was then redispersed in 50 mL of distilled water and sonicated for 30 min. To remove the surfactant, the solution was first filtered twice using PVDF membrane filters (MILLEX-HV, Millipore 0.22 μm), after which the doubly filtered solution was concentrated down to 1 mL and purified *via* column chromatography using Sephadex gel LH-20 as the stationary phase. Fractions were collected every 50 drops at a flow rate of a drop every 5 s. A hand held UV lamp (365 nm) was used to check each fraction for Si nanocrystal luminescence. The fractions were then combined and reduced to a total volume of 20 mL.

Characterisation of silicon nanocrystals

PL spectra with an excitation wavelength of 325 nm were recorded on a Perkin Elmer LS 50 luminescence spectrophotometer equipped with a pulsed Xenon discharge lamp and Monk-Gillieson monochromators. PL spectra of the silicon nanocrystal dispersions were recorded at room temperature using a quartz cuvette (1 cm), while spectra of the SIO and ncSi-SIO samples were recorded using a custom-built front face illumination insert. For that the opal sample was held at an angle of 22.5 degrees with respect to the excitation beam. The excitation and detection pathways were kept at standard 90 degree angle. Transmission Electron Microscopy (TEM) images were recorded using a JEOL 2100 electron microscope operating at 200 kV and equipped with a LAB₆ electron source. TEM samples were prepared by depositing evaporating aliquots of the silicon nanocrystal dispersion onto a carbon coated TEM grid.

Aerosol-assisted infiltration of silicon nanocrystals

A modified aerosol-assisted chemical vapour deposition (AACVD)⁴⁹ system consisting of a tubular quartz reactor containing a graphite susceptor was used for nanocrystal infiltration. 10 mL of nanocrystal solution (ncSis in water with a concentration of *ca.* 30 × 10⁻⁶ M L⁻¹ (30 micromolar)) was held in a container above the metal diaphragm of a modified commercially available ultrasonic humidifier to form an aerosol. The aerosol generated was swept into the reaction zone

using a nitrogen carrier gas (1.58 L min^{-1}) metered from a mass flow controller. The sample was maintained at $200 \text{ }^\circ\text{C}$ during exposure to the aerosol. The exposure time of the opal sample to the aerosol was 45 minutes. This sample was named as ncSi-SIO-1 and the sample prepared with double its concentration ($60 \text{ } \mu\text{M}$) ncSi as ncSi-SIO-2 in the following discussions.

Electron microscopy analysis of the opals

The top-view and cross-sectional scanning electron microscope (SEM) images of the IOs before and after ncSi deposition are obtained using a FEI Quanta 650 FEG High Resolution SEM. TEM cross section sample was prepared using Focused Ion Beam (FIB) (FEI DualBeam FIB Helios Nanolab 600i). At first, the top of the opal sample was deposited/protected with layers of carbon and platinum by electron beam induced deposition (EBID) method. After depositing a thicker ion beam induced (IBID) protection layer of platinum the lamellae is cut out and attached to a TEM grid. Then the lamellae are thinned down to approx. $300\text{--}500 \text{ nm}$ using the FIB at 30 kV . The final polishing is done with 2 kV in order to minimize the FIB induced damage to 2 nm per side. The targeted final thickness is in the range of $200\text{--}400 \text{ nm}$ to represent one opal layer thick sample. The cross sections are analyzed at 200 kV with JEOL JEM-2100 TEM with Oxford Inca EDX.

Results and discussion

In order to probe the structural periodicity as well as the extent and consistency of the opal structures; and to compare the micro structural change occurred for the IO before and after silicon nanocrystal incorporation, SEM top-view and cross-

sectional images were obtained. The SEM images are taken from the same opal sample before and after silicon nanocrystal incorporation for an unambiguous comparison. Fig. 1 shows SEM top-view and cross-section images of the SIOs before (Fig. 1a and b) and after nanocrystal incorporation (Fig. 1c and d). As the SEM of the opal before nanocrystal incorporation was recorded without the use of gold/palladium sputtering designed to reduce charging effects, the image quality is a little compromised as a result of charging effects. However, the SEM images show the extensive 3D connectivity in the SIO structure. The high quality of the inverse opal template can be appreciated from the fact that the three-coordinate interconnects from the second, third and the subsequent layers underneath can be observed. The incorporation of ncSis can be appreciated from the difference in surface texture of the silica skeleton (walls) supporting the air spheres. While the SIO shows smooth silica walls, nanocrystal incorporation made the walls thicker and rougher. A corresponding reduction in the air sphere diameter is also observed, where the air sphere diameter reduced from 295 nm for the SIO to 281 nm for the ncSi-SIO-2. The presence of nanocrystals in the structure is further confirmed by TEM analysis from a cross-section obtained by FIB slicing. The TEM cross-section image presented in Fig. 1e, the selected area electron diffraction (SAED) pattern obtained from the area highlighted by a rectangular box in Fig. 1e (Fig. 1f) and the SAED pattern of the pre-formed silicon nanocrystals (Fig. 1h) all confirm the nature and presence of the nanocrystals in the structure. The SAED patterns show the presence of $\{331\}$ and $\{113\}$ planes of silicon. The diffuse nature of the ring patterns indicates that the nanocrystal surfaces may be partially oxidized, which is not surprising. The TEM image of the pre-formed nanocrystals is presented in Fig. 1g. The particle size

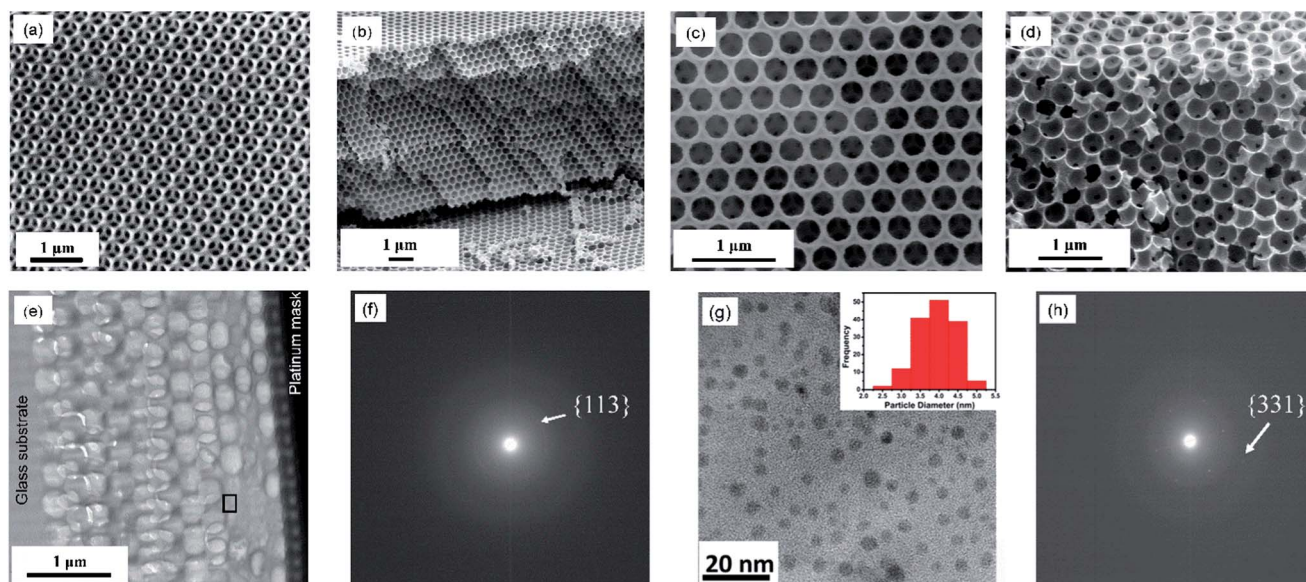


Fig. 1 SEM top view image of SIO (a), and cross-section image of the same opal template (b). SEM top view image of opal infiltrated with silicon nanocrystals (ncSi-SIO-2) (c), and cross-section image of the same sample (d). (e) TEM cross-section image of ncSi-SIO-2 prepared by FIB milling. (f) SAED pattern from the area highlighted by a black rectangular box in image (e). (g) HRTEM image of ncSis used for deposition with its histogram representing particle size distribution in the inset. (h) SAED pattern of preformed ncSi shown in image (g). The rings represent the $\{113\}$ and $\{331\}$ planes of silicon.

distribution tabulated from the TEM image (inset of Fig. 1g) shows that ncSi particles are formed in the size range 2.5–5 nm by the described method.

The robustness of the structure can be appreciated from the fact that the 12 layer thick composite SIO structure remained intact against collapsing even after FIB slicing to just a thin cross-section (Fig. 1e). This thin slice could withstand the pressure applied from the protective carbon/platinum plating employed prior to the FIB milling. We believe that the deformation of the top four layers of the template from spherical 'holes' towards a more egg-like shape is due to the pressure induced on from the platinum/carbon plating. The presence of platinum can be observed as a black infiltrate at the top layer (on the right hand side) of the composite SIO. Furthermore, the ability of the method to prepare robust large area, large domain size composite SIOs and SIO opals can be appreciated from the large area SEM images presented in the (ESI 1†).

The stop-gap properties of the samples were evaluated by recording the reflection spectra of samples at varying incidence angles, θ , 8° to 65° to the surface normal using a Perkin-Elmer Lambda 950 spectrophotometer in the wavelength range 200–2000 nm. The reflection spectra were recorded from the same SIO sample from almost the same spot before and after silicon nanocrystal incorporation. Fig. 2a shows the optical reflection spectra of SIO, modified ncSi-SIO-1 (deposited from 10 mL of silicon nanocrystal solution of concentration *ca.* 30×10^{-6} M L^{-1}) and modified ncSi-SIO-2 (deposited from a 10 mL silicon nanocrystal solution having twice the amount of silicon nanocrystals) samples recorded at 8° incidence. Fig. 2b–d show the optical reflection spectra of SIO, ncSi-SIO-1 and ncSi-SIO-2

samples recorded at incidence angles 8° to 30° to the opal surface normal.

As may be seen the incorporation of silicon nanocrystals resulted in a 44 nm red-shift of the stop-band for ncSi-SIO-2 (λ_{\max} , 672 nm) and a 32 nm red-shift for the stop-band of ncSi-SIO-1 (λ_{\max} , 660 nm) as compared to the bare SIO (λ_{\max} , 628 nm). In addition to the red-shift, both the first order and second order stop-bands of ncSi-SIO-2 (672 nm and 371 nm respectively) show significant band broadening compared to the bare SIO (628 nm and 324 nm respectively). In contrast the reduced level of silicon nanocrystal incorporation *via* infiltration from the more dilute solution (ncSi-SIO-1) resulted in only a moderate band broadening for the ncSi-SIO-1 sample. As a result, the gap-to-mid-gap ratio ($\Delta\lambda/\lambda$), which also represents the strength of the PBG, has increased from $\sim 6.6\%$ for SIO to $\sim 7.3\%$ for ncSi-SIO-1 and to $\sim 18.0\%$ for ncSi-SIO-2 samples in the incidence angle range 8° to 30° . The band broadening in turn resulted in an enhanced spectral overlapping for the ncSi-SIO-2 (Fig. 2d), for incidence angles 8° to 30° , as compared to the more dispersive stop-bands for the bare SIO (Fig. 2b) and ncSi-SIO-1 samples.

This result demonstrates the efficacy and tuneability of the aerosol-assisted infiltration method for the incorporation of silicon nanocrystals into the SIO template. The effect of nanocrystal incorporation can also be evidenced from the modification of the effective refractive indices (n_{eff}) for the ncSi-SIO-1 and ncSi-SIO-2 samples as compared to the bare SIO, as calculated from the plot of $\sin^2 \theta$ vs. λ_{\max}^2 (Fig. 2e). The n_{eff} is increased to 1.22 for ncSi-SIO-1 and further to 1.40 for ncSi-SIO-2 from that of 1.12 for the bare SIO. The refractive indices of the

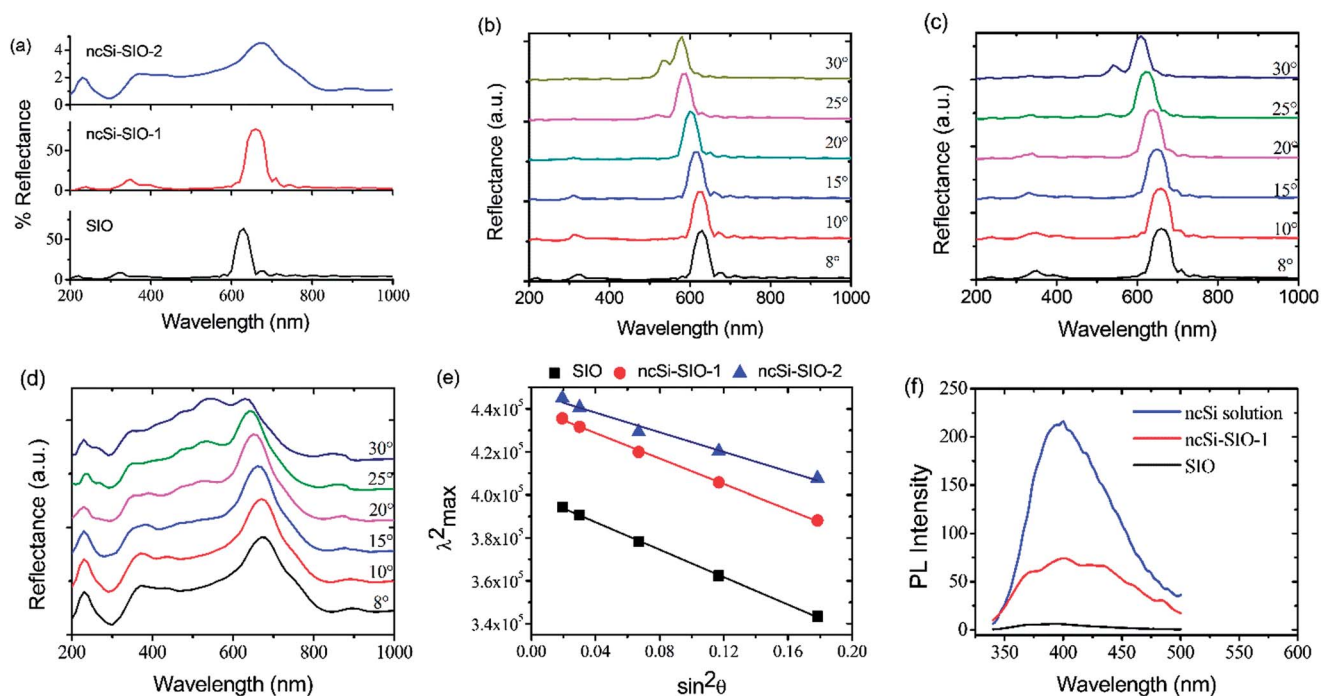


Fig. 2 (a) Reflection spectra of SIO, ncSi-SIO-1 and ncSi-SIO-2 samples recorded at an incidence angle of 8° to the opal surface normal. (b) Angle-resolved reflection spectra of SIO (c) ncSi-SIO-1 and (d) ncSi-SIO-2 samples recorded at incidence angles 8° to 30° . (e) Plot of $\sin^2 \theta$ vs. λ_{\max}^2 of the three opals. (f) PL emission spectra of ncSi-SIO-1, SIO (both collected at 60° angle to the opal surface normal) and ncSi solution.

composite silicon nanocrystal/silica backbone have increased to 1.69 and 2.16 for ncSi-SIO-1 and ncSi-SIO-2 samples respectively from that of 1.40 for bare silica backbone of SIO. All of these data were obtained from the optical data by solving the Bragg–Snell relation for photonic crystals: $\lambda_{\text{max}}^2 = 4d^2(n_{\text{eff}}^2 - \sin^2 \theta)$; where λ_{max} is the wavelength maximum of the reflectance band, d is the lattice spacing, n_{eff} is the effective refractive index of the photonic crystal, and θ is the angle of incidence of the impinging electromagnetic radiation to the photonic crystal surface normal.^{50,51}

Furthermore, above 30° incidence, the simultaneous multiple Bragg diffraction-induced multiple Bragg-wave coupling from the (111) and (200) planes of the inverse opal resulted in the modification of the stop-bands⁵² (not shown here). As a result the $\Delta\lambda/\lambda$ further increased to >12% and >30% for ncSi-SIO-1 and ncSi-SIO-2 respectively from that of ~8% for SIO. In addition, a less intense, almost non-dispersive band is observed at the high frequency region (~230 nm) for the modified SIO samples (Fig. 2a). This feature is assigned to be due to the Van Hove singularities indicating the presence of good periodicity in the 3D IO structure.^{53–55}

Despite resulting in band broadening and some spectral overlap, silicon nanocrystal incorporation has resulted in enhanced stop-bands for the nanocrystal composite ncSi-SIO samples as compared to the bare SIO, as evidenced from the increase in the gap to mid-gap ratio. However the reflectance properties of ncSi-SIO sample is reduced over an order of magnitude due to the loss mechanisms as discussed in the following discussion.

The increase in refractive index contrast is modest – and not as large as that which has been achieved previously in all silicon inverse opals prepared by other methods.⁵⁶ However, the significant red-shift (44 nm) in the stop-band as well as its reduced dispersion, which reflects its tendency to form a complete PBG, as compared to the SIO sample, indicates the clear influence of the formation of a thin layer of silicon nanocrystals on the SIO walls for the composite SIO samples. Although the near non-dispersive nature of the stop-bands of composite SIO samples theoretically suggests that nanocrystal infiltration is isotropic and occurs on all exposed walls of the SIO structure, it is possible that the diminished stop-bands arise from enhanced scattering effects and/or possible interference from the organics used for ncSi synthesis and functionalization⁵⁷ – in other words such effects may arise because the nanocrystalline silicon may contain lower refractive index contamination.

The realization of ncSi patterning onto the walls of SIO structure was further examined by PL emission studies. In principle, the light emitted from the semiconductor ncSis should be modified in presence of the dielectric periodicity of the ncSi-SIO structure.^{29,30,58–65} Fig. 2f shows the PL spectra of ncSi prior to deposition (blue line), SIO (black line) and ncSi-SIO-1 (red line). Since in the PL measurements, the emitted light is collected at 60° angle with respect to the opal surface normal, the reflection and transmission spectra of ncSi-SIO-1 sample measured at 60° incidence is also recorded and presented in ESI 2.† The ncSi solution used here is characterized with a broad emission centred at ~400 nm,⁶⁶ possibly resulting from factors such as (i), the

excitonic emission of nanocrystals of diameter <5 nm^{67–70} (ii), the modification of said emission by the amine surface passivation employed and (iii), possible charge carrier recombination at the oxidised surfaces.^{71,72} The modified emission of ncSis when integrated into the SIO-1 structure shows almost similar spectral features but with a comparatively lower intensity. The SIO sample prior to deposition on the other hand exhibits a negligible background emission. The fact that the PL emission does not fall in the band-edge wavelength of the ncSi-SIO opal theoretically rules out the enhancement of PL emission. The slightly attenuated/diminished PL emission in this case may be attributed to the effect of the diffuse scattering resulting from the presence of disorder (dislocations, point defects and line defects) inherent to the SIO structure, to possible absorption losses due to the ncSis, as well as to a possible interference from the roughened interfaces of the ncSi-SIO structure, which happens to be higher at the higher energy region of the stop-band.⁷³ Overall, the observation of much of the ncSi PL emission spectrum despite the presence of various loss mechanisms underlines the efficacy of 3D patterning by the method presented here.

The method described here is significant considering its ability to integrate functional materials into complex 3D structures by a simple process. Furthermore the preparation of integrated-silicon inverse opals as described here may have potential technological implications in view of the ability of silicon to be integrated with many existing industrial processes. For example as noted earlier silicon has already been identified as one ideal material for the development of complete PBGs in 3D photonic crystals^{22,54,55,74,75} although germanium has also been used due to its similarities in properties to silicon.^{20,76–79}

Concerning the specific topic of optimising the PBG properties in silicon based photonic crystals previous reports have focused on the fabrication of silicon inverse opals by means of colloidal crystal templating,⁸⁰ *i.e.* by first depositing crystalline silicon into a silica photonic crystal template using chemical vapour deposition of a suitable precursor⁷⁵ followed by removal of the silica template by chemical dissolution.⁵⁴ However, the complexity of the method, involving as it does many intricate fabrication steps, and in particular the harsh HF chemical dissolution step, may pose serious limitations when it comes to maintaining the robustness of the structure and the reproducibility and scale up of the process.

To the best of our knowledge, all previous silicon based methods have demonstrated mostly near-infrared to infrared PBG properties. The effective integration of silicon into the photonic crystal template without compromising its structural periodicity and robustness has been a challenge for the development of visible light responsive photonic crystals. The method presented here is simple, straightforward and clearly addresses many of the limitations of the previously reported methods. Firstly, the large area, robust SIOs can be prepared by a mild chemical leaching method, just by immersing the PC in acetone, which avoids the harsh HF etching processes as has been used by the previously reported methods. The use of a sacrificial PMMA template is hence very significant in this method, because of its complete leachability in acetone.

Secondly, the use of SiO₂ as template allows an effective and straightforward deposition of ncSi due to its highly accessible interconnected larger spherical air spaces than just the narrow and small void spaces in 3D PCs. The successful realization of the 3D patterning of ncSi here is achieved by combining these two straightforward processes, hence making it simple yet scalable.

In addition previous methods adopted for the preparation of sub-micrometric 3D inverse opals were based on the deposition of the required dielectric/functional material into the voids of self-assembled opal templates by means of chemical infiltration followed by reduction,^{78,81,82} electrodeposition,^{38,83–86} atomic layer deposition (ALD)^{87–90} or by CVD.^{22,39,54,91} Although these methods have enabled the experimental validation of some of the unique optical properties of high dielectric contrast PCs, the extensive use of them may be limited due to a number of factors such as the complexity of the steps involved, the structural fragility of the opals prepared, as well as their limitations in achieving a uniform infiltration/deposition. Although ALD enables an atomic level conformal deposition of functional materials into the template void spaces,⁹² the lengthy cycles (time and cost) needed is a matter of concern in many application fields.

Conclusions

In conclusion, we have presented a simplified fabrication of 'tunable'⁹³ silicon-silica inverse opals using a colloidal crystal templating method combined with aerosol-assisted nanocrystal infiltration within the inverse opal. This method enables the 3D patterning of ncSis into robust silicon-silica inverse opals of larger areas and domain sizes. The highly accessible and robust 3D air spheres facilitated an effective deposition of ncSis onto all the available 3D silica walls in the structure. The method offers a significant advancement on the effective integration of functional/high dielectric materials into complex 3D structures. While the effective integration of ncSis facilitates photonic stop-band broadening and subsequent spectral overlap in the visible light frequency region, the flexibility of tuning the ncSi PL emission by a pre-deposition step should enable an effective control of light emitting features with respect to the PBG, thus offering great promise for future photonic technologies. Currently we are in the process of tuning the template photonic stop-gap frequencies and ncSi PL emission for the enhancement of the efficiencies of LED devices. Finally we note that the method of introducing the ncSi is quite generic and could also be used to incorporate other nanostructured materials including plasmonically active metal particles, biologically active nanoparticles or particles having tailored catalytic activity.

Acknowledgements

The work was supported by the Science Foundation Ireland (SFI PI 07/IN.1/1787). We thank EMAX, Tyndall for providing the microscopy facilities. We also thank the University of Malaysia Terengganu for a PhD studentship for Ms Kassim.

Notes and references

- 1 V. N. Bogomolov, S. V. Gaponenko, I. N. Germanenko, A. M. Kapitonov, E. P. Petrov, N. V. Gaponenko, A. V. Prokofiev, A. N. Ponyavina, N. I. Silvanovich and S. M. Samoilovich, *Phys. Rev. E: Stat. Phys., Plasmas, Fluids, Relat. Interdiscip. Top.*, 1997, **55**, 7619.
- 2 S. John, *Phys. Rev. Lett.*, 1987, **58**, 2486.
- 3 E. Yablonovitch, *Phys. Rev. Lett.*, 1987, **58**, 2059.
- 4 H. Kosaka, T. Kawashima, A. Tomita, M. Notomi, T. Tamamura, T. Sato and S. Kawakami, *Phys. Rev. B: Condens. Matter*, 1998, **58**, 10096.
- 5 J. D. Joannopoulos, P. R. Villeneuve and S. Fan, *Nature*, 1997, **386**, 143.
- 6 S. Ogawa, M. Imada, S. Yoshimoto, M. Okano and S. Noda, *Science*, 2004, **305**, 227.
- 7 Y. N. Xia, B. Gates, Y. D. Yin and Y. Lu, *Adv. Mater.*, 2000, **12**, 693.
- 8 K. M. Ho, C. T. Chan, C. M. Soukoulis, R. M. Biswas and M. Sigalas, *Solid State Commun.*, 1994, **89**, 413.
- 9 K. Busch and S. John, *Phys. Rev. E: Stat. Phys., Plasmas, Fluids, Relat. Interdiscip. Top.*, 1998, **58**, 3896.
- 10 A. Moroz, *Europhys. Lett.*, 2000, **50**, 466.
- 11 C. Lopez, *Adv. Mater.*, 2003, **15**, 1679.
- 12 A.-P. Hynninen, J. H. J. Thijssen, E. C. M. Vermolen, M. Dijkstra and A. V. Blaaderen, *Nat. Mater.*, 2007, **6**, 202.
- 13 J. D. Joannopoulos, S. G. Johnson, J. N. Winn and R. D. Meade, *Photonic Crystals: Molding the Flow of Light*, Princeton University Press, 2nd edn, 2008.
- 14 I. I. Tarhan and G. H. Watson, *Phys. Rev. Lett.*, 1996, **76**, 315.
- 15 P. L. Gourley, J. R. Wendt, G. A. Vawter, T. M. Brennan and B. E. Hammons, *Appl. Phys. Lett.*, 1994, **64**, 687.
- 16 H. Míguez, C. Lopez, F. Meseguer, A. Blanco, L. Vazquez, R. Mayoral, M. Ocana, V. Fornes and A. Mifsud, *Appl. Phys. Lett.*, 1997, **71**, 1148.
- 17 F. Garcia-Santamaria, C. Lopez, F. Meseguer, F. Lopez-Tejeira, J. Sanchez-Dehesa and H. T. Miyazaki, *Appl. Phys. Lett.*, 2001, **79**, 2309.
- 18 H. S. Sözüer, J. W. Haus and R. Inguva, *Phys. Rev. B: Condens. Matter*, 1993, **45**, 13962.
- 19 Y. A. Vlasov, X.-Z. Bo, J. C. Sturm and D. J. Norris, *Nature*, 2001, **414**, 289.
- 20 F. Garcia-Santamaria, M. Ibisate, I. Rodriguez, F. Meseguer and C. Lopez, *Adv. Mater.*, 2003, **15**, 788.
- 21 Y.-J. Li, K. Xie, J. Xu and P.-P. Du, *Appl. Phys. A: Mater. Sci. Process.*, 2010, **99**, 117.
- 22 A. Blanco, E. Chomski, S. Grabtchak, M. Ibisate, S. John, S. W. Leonard, C. Lopez, F. Meseguer, H. Míguez, J. P. Mondia, G. A. Ozin, O. Toader and H. M. V. Driel, *Nature*, 2000, **405**, 437.
- 23 S. Noda, K. Tomoda, N. Yamamoto and A. Chutinan, *Science*, 2000, **289**, 604.
- 24 E. Palacios-Lidón, A. Blanco, M. Ibisate, F. Meseguer, C. Lopez and J. Sanchez-Dehesa, *Appl. Phys. Lett.*, 2002, **81**, 4925.

- 25 N. Tetreault, H. Miguez and G. A. Ozin, *Adv. Mater.*, 2004, **16**, 1471.
- 26 S. Noda, *MRS Bull.*, 2009, **34**, 751.
- 27 S. A. Rinne, F. Garcia-Santamaria and P. V. Braun, *Nat. Photonics*, 2008, **2**, 52.
- 28 A. Kress, F. Hofbauer, N. Reinelt, M. Kaniber, H. J. Krenner, R. Meyer, G. Bohm and J. J. Finley, *Phys. Rev. B: Condens. Matter*, 2005, **71**, 241304.
- 29 P. Lodahl, A. F. van Driel, I. S. Nikolaev, A. Irman, K. Overgaag, D. Vanmaekelbergh and W. L. Vos, *Nature*, 2004, **430**, 654.
- 30 S. G. Romanov, A. V. Fokin and R. M. De La Rue, *Appl. Phys. Lett.*, 1999, **74**, 1821.
- 31 T. Suezaki, H. Yano, T. Hatayama, G. A. Ozin and T. Fuyuki, *Appl. Phys. Lett.*, 2011, **98**, 072106.
- 32 T. G. Euser, H. Wei, J. Kalkman, Y. Jun, A. Polman, D. J. Norris and W. L. Vos, *J. Appl. Phys.*, 2007, **102**, 053111.
- 33 J. F. Galisteo-Lopez, M. Ibisate, R. Sapienza, L. S. Froufe-Perez, A. Blanco and C. Lopez, *Adv. Mater.*, 2011, **23**, 30.
- 34 T. Suezaki, P. G. O'Brien, J. I. L. Chen, E. Loso, N. P. Kherani and G. A. Ozin, *Adv. Mater.*, 2009, **21**, 559.
- 35 P. Jiang, J. F. Bertone, K. S. Hwang and V. L. Colvin, *Chem. Mater.*, 1999, **11**, 2132.
- 36 P. M. Johnson, A. F. Koenderink and W. L. Vos, *Phys. Rev. B: Condens. Matter*, 2002, **66**, 081102.
- 37 M. Lopez-Garcia, J. F. Galisteo-Lopez, A. Blanco, J. Sanchez-Marcos, C. Lopez and A. Garcia-Martin, *Small*, 2010, **6**, 1757.
- 38 K. A. Arpin, A. Mihi, H. T. Johnson, A. J. Baca, J. A. Rogers, J. A. Lewis and P. V. Braun, *Adv. Mater.*, 2010, **22**, 1084.
- 39 H. Ning, A. Mihi, J. B. Geddes III, M. Miyake and P. V. Braun, *Adv. Mater.*, 2012, **24**, OP153.
- 40 C.-H. Sun and P. Jiang, *Nat. Photonics*, 2008, **2**, 9.
- 41 F. Gallego-Gomez, M. Ibisate, D. Golmayo, F. J. Palomares, M. Herrera, J. Hernandez, S. I. Molina, A. Blanco and C. Lopez, *Adv. Mater.*, 2011, **23**, 5219.
- 42 A. vanBlaaderen, R. Ruel and P. Wiltzius, *Nature*, 1997, **385**, 321.
- 43 O. D. Velev, T. A. Jede, R. F. Lobo and A. M. Lenhoff, *Nature*, 1997, **389**, 447.
- 44 Z. C. Zhou and X. S. Zhao, *Langmuir*, 2005, **21**, 4717.
- 45 B. Hatton, L. Mishchenko, S. Davis, K. H. Sandhage and J. Aizenberg, *PNAS*, 2010, **23**, 10354.
- 46 C. P. Sibu, S. R. Kumar, P. Mukundan and K. G. K. Warriar, *Chem. Mater.*, 2002, **14**, 2876.
- 47 C. J. Brinker and G. W. Scherer, *Sol-Gel Science*, Academic Press, New York, 1990
- 48 A. Shiohara, S. Hanada, S. Prabakar, K. Fujioka, T. H. Lim, K. Yamamoto, P. T. Northcote and R. D. Tilley, *J. Am. Chem. Soc.*, 2010, **132**, 248.
- 49 M. Numata and Y. Koide, *Beilstein J. Nanotechnol.*, 2010, **1**, 71.
- 50 P. T. Miclea, A. S. Susha, Z. Liang, F. Caruso, C. M. S. Torres and S. G. Romanov, *Appl. Phys. Lett.*, 2004, **84**, 3960.
- 51 S. C. Padmanabhan, J. McGrath, M. Bardosova and M. E. Pemble, *J. Mater. Chem.*, 2012, **22**, 11978.
- 52 H. M. V. Driel and W. L. Vos, *Phys. Rev. B: Condens. Matter*, 2000, **62**, 9872.
- 53 R. V. Nair and R. Vijaya, *Phys. Rev. A*, 2007, **76**, 053805.
- 54 A. Blanco and C. López, *Adv. Mater.*, 2006, **18**, 1593.
- 55 N. Tetreault, H. Miguez, V. Kitaev, S. M. Yang and G. A. Ozin, *Adv. Mater.*, 2003, **15**, 1167.
- 56 A. Blanco, E. Chomski, S. Grabtchak, M. Ibisate, S. John, S. W. Leonard, C. Lopez, F. Meseguer, H. Miguez, J. P. Mondia, G. A. Ozin, O. Toader and H. M. van Driel, *Nature*, 2000, **405**, 437.
- 57 D. Y. Wang, J. S. Li, C. T. Chan, V. Sagueirino-Maceira, L. M. Liz-Marzan, S. Romanov and F. Caruso, *Small*, 2005, **1**, 122.
- 58 P. Lambropoulos, G. M. Nikolopoulos, T. R. Nielsen and S. Bay, *Rep. Prog. Phys.*, 2000, **63**, 455.
- 59 S. John and T. Quang, *Phys. Rev. A*, 1994, **50**, 1764.
- 60 S. P. Ogawa, M. Imada, S. Yoshimoto, M. Okano and S. Noda, *Science*, 2004, **305**, 227.
- 61 T. Yamasaki and T. Tsutsui, *Appl. Phys. Lett.*, 1998, **72**, 1957.
- 62 E. P. Petrov, V. N. Bogomolov, I. I. Kalosha and S. V. Gaponenko, *Phys. Rev. Lett.*, 1998, **81**, 77.
- 63 S. G. Romanov, A. V. Fokin, V. I. Alperovich, N. P. Johnson and R. M. De La Rue, *Phys. Status Solidi A*, 1997, **164**, 169.
- 64 Y. A. Vlasov, M. Deutsch and D. J. Norris, *Appl. Phys. Lett.*, 2000, **76**, 1627.
- 65 J. Valenta, J. Linnros, R. Juhasz, J. L. Rehspringer, F. Huber, C. Hirlimann, S. Cheylan and R. G. Elliman, *J. Appl. Phys.*, 2003, **93**, 4471.
- 66 J. H. Warner, A. Hoshino, K. Yamamoto and R. D. Tilley, *Angew. Chem., Int. Ed.*, 2005, **44**, 4550.
- 67 G. Ledoux, O. Guillois, D. Porterat, C. Reynaud, F. Huisken, B. Kohn and V. Paillard, *Phys. Rev. B: Condens. Matter*, 2000, **62**, 15942.
- 68 W. D. A. M. D. Boer, D. Timmerman, K. Dohnalova, I. N. Yassievich, H. Zhang, W. J. Buma and T. Gregorkiewicz, *Nat. Nanotechnol.*, 2010, **5**, 878.
- 69 M. V. Wolkin, J. Jorne, P. Fauchet, G. Allan and C. Delerue, *Phys. Rev. Lett.*, 1999, **82**, 197.
- 70 F. Gallego-Gómez, M. Ibisate, D. Golmayo, F. J. Palomares, M. Herrera, J. Hernández, S. I. Molina, Á. Blanco and C. López, *Adv. Mater.*, 2011, **23**, 5219.
- 71 M. J. Sailor and E. C. Wu, *Adv. Funct. Mater.*, 2009, **19**, 3195.
- 72 S. Godefroo, M. Hayne, M. Jivanescu, A. Stesmans, M. Zacharias, O. I. Lebedev, G. V. Tendeloo and V. V. Moshchalkov, *Nat. Nanotechnol.*, 2008, **3**, 174.
- 73 J. Ma, B. R. Parajuli, M. G. Ghossoub, A. Mihi, J. Sadhu, P. V. Braun and S. Sinha, *Nano Lett.*, 2013, **13**, 618.
- 74 A. Birner, R. B. Wehrspohn, U. M. Gösele and K. Busch, *Small*, 2001, **6**, 377.
- 75 M. Ibisate, D. Golmayo and C. Lopez, *Adv. Mater.*, 2009, **21**, 2899.
- 76 H. Miguez, F. Meseguer, C. López, M. Holgado, G. Andreassen, A. Mifsud and V. Fornés, *Langmuir*, 2000, **16**, 4405.
- 77 H. Miguez, E. Chomski, F. García-Santamaría, M. Ibisate, S. John, C. López, F. Meseguer, J. P. Mondia, G. A. Ozin, O. Toader and H. M. V. Driel, *Adv. Mater.*, 2001, **13**, 1634.

- 78 R. G. Shimmin, R. Vajtai, R. W. Siegel and P. V. Braun, *Chem. Mater.*, 2007, **19**, 2112.
- 79 M. Seino, E. J. Henderson, D. P. Puzzo, N. Kadota and G. A. Ozin, *J. Mater. Chem.*, 2011, **21**, 15895.
- 80 D. J. Norris and Y. A. Vlasov, *Adv. Mater.*, 2001, **13**, 371.
- 81 H. Yan, C. F. Blanford, B. T. Holland, M. Parent, W. H. Smyrl and A. Stein, *Adv. Mater.*, 1999, **11**, 1003.
- 82 K. M. Kulinowski, P. Jiang, H. Vaswani and V. L. Colvin, *Adv. Mater.*, 2000, **12**, 833.
- 83 J. E. G. J. Wijnhoven, S. J. M. Zevenhuizen, M. A. Hendriks, D. Vanmaekelbergh, J. J. Kelly and W. L. Vos, *Adv. Mater.*, 2000, **2**, 888.
- 84 P. N. Bartlett, J. J. Baumberg, P. R. Birkin, M. A. Ghanem and M. C. Netti, *Chem. Mater.*, 2002, **14**, 2199.
- 85 M. Fu, J. Zhou, Q. Xiao, B. Li, R. Zong, W. Chen and J. Zhang, *Adv. Mater.*, 2006, **18**, 1001.
- 86 S. Kassim, S. C. Padmanabhan, M. Salaun and M. E. Pemble, *AIP Conf. Proc.*, 2011, **1391**, 263.
- 87 A. Ruge, J. Becker, R. G. Gordon and S. H. Tolbert, *Nano Lett.*, 2003, **3**, 1293.
- 88 J. S. King, E. Graugnard and C. J. Summers, *Adv. Mater.*, 2005, **17**, 1010.
- 89 I. M. Povey, D. Whitehead, K. Thomas, M. E. Pemble, M. Bardosova and J. Renard, *Appl. Phys. Lett.*, 2006, **89**, 104103.
- 90 E. Graugnard, V. Chawla, D. Lorang and C. J. Summers, *Appl. Phys. Lett.*, 2006, **89**, 211102.
- 91 N. J. Trujillo, S. H. Baxamusa and K. K. Gleason, *Chem. Mater.*, 2009, **21**, 742.
- 92 D. P. Gaillot and C. J. Summers, *J. Appl. Phys.*, 2006, **100**, 113118.
- 93 One can tune the size of ncSis as they are prepared prior to deposition process.

Chapter 8: Summary, Conclusions and Suggestions for Future Work

8.1 Summary and Conclusions

A modified method for the synthesis of colloidal PMMA particles having a high degree of monodispersity (<5% PD) has been developed. This method has been used in the fabrication of high-quality PMMA-based photonic crystals using dip coating and controlled evaporation methods.

Inverse metallic (Ni and Au) PhCs with near 100% void filling have been fabricated via an electrodeposition process. Increased metal deposition was achieved by increasing the electrodeposition time.

Pre-formed Au nanoparticles having well-defined plasmon resonances have been successfully incorporated onto the surfaces PMMA spheres by the use of a PEI primer method. This is an improved coating method as compared to those previously described in the literature.

PMMA@Au core-shell particle PhC films were successfully prepared, without the need of a secondary shell, by controlled evaporation deposition. Films produced show photonic band gap effects. A study of the optical properties of the bare PMMA structure and the PMMA@Au structure reveals that the Au appears to effectively suppress much of the Bragg reflection seen for the bare sample. The angle resolved optical reflectance spectra of materials constructed by assembling dielectric@metal core-shell particles, silica-Au NPs and nanocrystalline silicon-silica inverse opal show good agreement with the Bragg–Snell correlation respectively.

Co-crystallisation has been shown to be a simple and efficient method for making added-value metallodielectric photonic crystals

A new method for the fabrication of inverted opals containing pre-formed silicon nanoparticles using aerosol assisted CVD was successfully achieved.

In conclusion, this work has studied a number of different PMMA- based colloidal photonic band gap systems and has demonstrated simple chemical procedures by which bare polymer materials may be enhanced either by subsequent processing or via the use of methods which induce changes during fabrication. The materials produced are of interest not only from the perspective of being templates for the formation of inverted, higher refractive index contrast materials, but also in their own right as materials which

can utilise the properties of pre-formed nanoparticles. These latter materials may find application in a range of devices including photovoltaics, filters and waveguides.

8.2 Suggestions for Future Work

There are several possibilities for future work based on an extension of the work presented in this thesis. Most of these would impact in terms of real, practical applications, which have really only been touched upon in this thesis. Some of them are outlined below:

- A more detailed quantitative analysis on the effect of plasmonic–photonic mode-coupling on the band gap properties should be studied in the future. In addition, the possible use of such structures for surface-enhanced Raman spectroscopy should be explored, see Appendix A.
- The process of co-crystallisation, whereby added functionality is introduced into the photonic crystal during the assembly process has yet to be fully exploited. Typical additional applications of this approach could include the development of light-induced drug release materials possibly in the form of skin patches, novel photo-catalysts for air and water purification that display an advantage over conventional materials such as TiO_2 particles in that the efficiency of light coupling to the photocatalyst may be enhanced, novel sensor-based devices that exploit the optical properties of immobilised

nanoparticles and, as noted at various points in the thesis, improved photovoltaic devices possibly involving sensitisation using nanoparticles.

- Plasmon-photonic band gap coupling effects implied by certain measurements made in this work should be the subject of a much more detailed analysis in order to verify or deny their existence. Such coupling provides a potential route to the directional extraction of light trapped within a photonic crystal, which may have many different applications if only it could be reproducibly controlled.
- Finally, the use of roll-to-roll assembly methods for PMMA-based photonic crystals and the co-crystallised materials should be explored, since this could provide a means of fabricating large-area, high-volume based materials which would be cheaper and which would permit the development of a range of innovative new products. At the time of writing it is known that such experiments are underway in our laboratories.

Appendix A: Preliminary Studies of the use of Metallo-dielectric Photonic Crystals as Substrates for Surface-Enhanced Raman Spectroscopy

A.1 Introduction

Metal nanoparticles are well-known to possess interesting and useful electronic, magnetic, optical and catalytic properties which are different from those of their bulk counterparts. Nanoparticles of the noble metals (silver and gold) offer broad absorption bands in the visible region of the electromagnetic spectrum, and their solutions possess very intense colours which are absent in the bulk material [1]. This behaviour is attributed to the collective oscillation of the free conduction electrons when they are resonant with an applied electromagnetic field and these metals possess localized surface plasmon resonance (LSPR) properties. The LSPR frequency of the nanoparticles is a function of their shape and of the surrounding medium [2]. The unique characteristics of LSPR form the basis of a plethora of applications in diverse fields ranging from electronics and photonics [3], sensing and catalysis, [4, 5] to biology and medicine [6, 7]. Furthermore, LSPR is also responsible for the electromagnetic field enhancements that

Appendix A

lead to surface-enhanced Raman spectroscopy (SERS) and other surface-enhanced spectroscopic processes [8].

It is well established that molecules adsorbed at certain (rough) metal surfaces and nanoparticles show strong SERS, a phenomenon which was discovered by Fleischmann *et al.* in 1974 [9]. This effect was observed whilst using Raman scattering to probe the electrochemical reaction of pyridine at roughened silver (Ag) electrodes, and is responsible for an enhancement of up to 10^{16} fold in Raman scattering from the adsorbed molecules. There are two sources of the SERS effect: electromagnetic and chemical. The latter is considered to arise from the effect of the metal on the bonding in molecules adsorbed at the metal surface. The electromagnetic SERS phenomenon is observed when incident light excites localized plasmons of the metal, increasing the electromagnetic field near the metallic surface and resulting in an enhancement of the Raman signal of nearby molecules by many orders of magnitude [10]. Because each molecule has a distinct vibrational spectrum, exploitation of the SERS effect allows molecules upon noble metal nanoparticles to be uniquely identified by Raman spectroscopy [11, 12].

Baumberg *et al.* have clearly demonstrated [13] the resonant plasmon enhancement of the SERS signal by using nanostructured metal surfaces. Sharp enhancements occur when the laser is scanned through a plasmon resonance (ingoing) and also when individual Raman scattered lines coincide with plasmon resonances (outgoing). Mahajan *et al.* have presented [14] the fabrication of sphere segment void (SSV) substrates by colloidal crystal-templated electrodeposition in surface-enhanced Raman spectroscopy (SERS)

Appendix A

applications. SSV substrates support a variety of plasmon modes which scale with cavity dimensions and give rise to SERS enhancements of 10^6 or greater.

Gold (Au NPs) and silver nanoparticles (Ag NPs) have most notably been used in SERS applications because their plasmon resonance frequencies fall within the visible and near-infra red regions of the electromagnetic spectrum, and are thus ideal to excite Raman modes. It is well known that Ag NPs possess an intense SERS enhancement; however, these species are prone to oxidation. Consequently, Au NPs are used in SERS applications on account of their stability, biocompatibility and scope for surface chemistry, although their SERS enhancements are not as significant as with Ag [11].

In this Appendix, the work on our Au NPs described in previous chapters has been used in a series of preliminary studies aimed at identifying potential SERS-active structures.

The essential proposition that is explored concerns (i), the possible enhancement of scattering intensity resulting from the Au NPs employed as part of the architecture of the materials and (ii), the possible use of the photonic band gap to capture Raman light scattered over 4π steradians and channel this light towards the detector.

Although these initial experiments have not been entirely successful, they have revealed a possible SERS effect for one type of material produced here which may be accounted for using conventional SERS theory. The work also reveals which issues need to be resolved if such materials are ever to be used as cheap, reproducible substrates for SERS experiments.

A.2 Results and Discussion

A.2.1 Optical Absorption from PMMA: Au Nanoparticle Composite Films

Au NPs were utilized in this work since as shown in Chapter 4 they could be added to the surface of PMMA particles of diameter 373 nm to form a so-called core-shell system. This work was extended in Chapter 6 in order to fabricate silica-Au inverse opals.

UV/Vis absorption spectra were recorded from both of these materials and are shown in Figures A.1 and A.2. From Figures A.1 and A.2 it may be seen that the surface plasmon resonance (SPR) bands of the PMMA@Au core-shell material and the silica-Au inverse opal film appear at ca. 540 nm and 562 nm, respectively. The plasmon is much more clearly defined for the inverted sample as evidenced by the presence of a well-defined peak, as compared to the broad, weak feature seen for the core-shell sample.

Possible reasons for the differences in the absorption spectra for the two types of samples are:

- (i) The inverted structure contains much more Au than the core-shell system, while the Au deposit in the inverted samples is also more random, consisting of more isolated nanoparticles as described in Chapter 6, suggesting that a degree of roughness comparable with the diameter of the NPs is preserved upon infiltration with the gold NPs.

Appendix A

- (ii) The differences may arise from the change in composite dielectric function. It is well-known [11] that the increase in the refractive index of the surrounding medium and the decrease in the inter-particle distance between neighbouring metal nanoparticles influence the spectral features of samples containing dispersed metal nanoparticles.

From the point of view of a possible resonance effect arising from such materials, both samples would have some degree of overlap between the wavelength of the plasmon related feature and the laser line used to generate Raman spectra (514 nm) see next section.

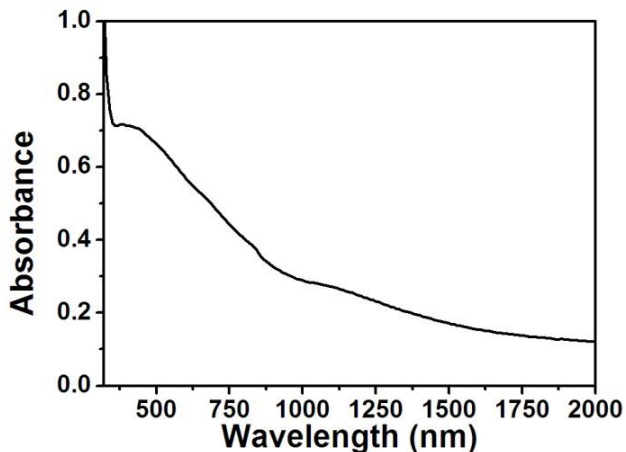


Figure A.1 Absorbance spectrum from a PMMA@Au film.

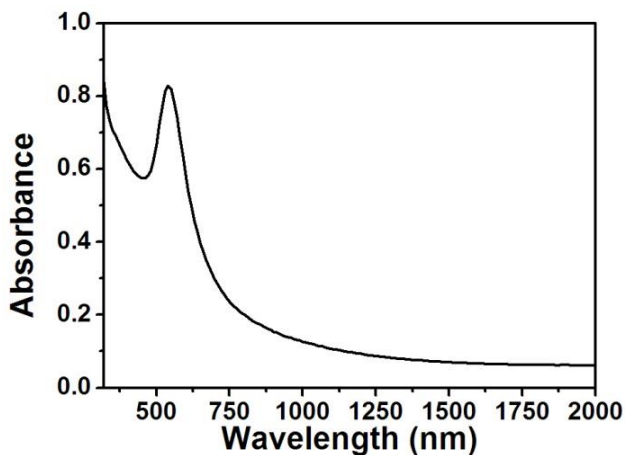


Figure A.2 Absorbance spectrum from a silica-Au inverse opal film.

A.2.2 Surface-Enhanced Raman Spectroscopy (SERS) Effects

Preliminary Raman studies were performed using the core-shell structure, Figure A.3. Not shown in Figure A.3 are the results obtained from an inverted structure and a plain Au film deposited onto glass and coated with a typical target analyte, 4-aminothiophenol (4-ATP).

This ‘control’ sample showed no evidence of any SERS enhancement effect, possibly because the film was flat and smooth and hence would not be expected to have a plasmon resonance near the wavelength of the laser line [15].

Appendix A

Concerning the samples evaluated here, Figure A.3 (a) is a typical Raman spectrum recorded from a bare PMMA opal film containing no Au NPs. This spectrum shows a number of features which are consistent with the structure of the PMMA.

Figure A.3 (b) is then a Raman spectrum recorded from the core-shell sample. Clearly some PMMA features are apparent, but from a preliminary comparison of scattering intensities with Figure A.3 (a) one would conclude that the spectrum shown in Figure A.3 (b) does indeed show some possible enhancement in intensity. Furthermore the more 'simple' spectrum (fewer bands) that is observed (again in comparison to that shown in Figure A.3 (a)) is reminiscent of the type of SERS spectra reported previously, where only certain vibrational modes appear in the SER spectrum- i.e. the SERS process demonstrates the operation of some new 'selection rules'[11].

Further control samples demonstrate that as might be expected, neither the Raman spectrum from a silica inverted opal nor that from an inverse silica opal+Au NPs shows any molecular vibrations due to the absence of any molecular species other than the silica itself.

Silica is a highly polar material and as such it gives rise to intense absorptions in the infrared region and only very weak Raman scattering [16, 17].

Thus it may be concluded that Figure A.3 (b) possibly represents a genuine example of a SERS signal, coming from the PMMA that is attached to, or very close to the plasmonic gold structure. Obviously further work is required in order to confirm or deny this

Appendix A

hypothesis, but this result could represent an example of the use of a simple, cheap, robust substrate that could be used in routine SERS investigations.

Clearly if there is any enhancement of the Raman signal in Figure A.3 (b) the enhancement factor must be quite low, perhaps only between 3x and 5x, as compared to the 'normal' Raman spectrum in Figure A.3 (a). This might be due to a lack of coupling of the incident radiation to the plasmon associated with the gold structure, which might be structural, or electronic in nature.

Structural factors seem unlikely to play a role here since a reduction in the enhancement factor would imply that the PMMA is not 'close' to the gold structure.

Alternatively a weak enhancement may arise because of the relationship between the exciting line and the electronic structure of the metal. It is known that the magnitude of the SERS effect can be affected by the wavelength of the laser used and the SPR wavelength of the metal nanoparticles, and thus some matching of the laser wavelength with the metal compositions is desirable. Wavelength-scanned SERS experiments by McFarland *et al.* [18] have shown that for a fixed Raman shift the surface plasmon wavelength should be roughly halfway between the incident laser wavelength and the Stokes shifted wavelength. They found that the SERS enhancement factor increases as the LSPR and laser wavelength are simultaneously shifted toward the red (up to a maximum wavelength of 785 nm).

Appendix A

Our data show that the enhancement in intensity of the Raman spectrum from the PMMA@Au core-shell material at the laser wavelength 514 nm, if indeed there is any, is quite weak. Where gold has been used previously for SERS experiments this phenomenon has been attributed to the presence of an inter-band transition near the green region of the spectrum for Au [19]. Indeed it has been found that efficient SERS from gold can only be observed when exciting with longer wavelength radiation, below the energy of the inter-band transition.

Thus it is suggested that experiments should be repeated using longer wavelength exciting lines in order to fully test this hypothesis.

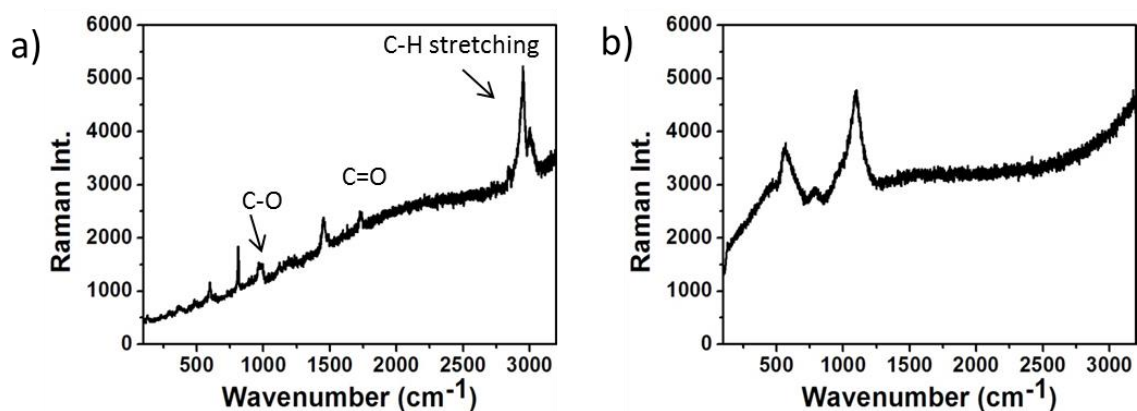


Figure A.3 Raman spectra of a) PMMA bare opal film b) PMMA@Au core-shell film
The excitation wavelength $\lambda = 514$ nm, diameter spot size = $1\mu\text{m}$, laser power = 5mW
and accumulation time = 30 s.

Appendix A

In terms of testing the ability of the photonic crystal to ‘focus’ the Raman scattered light towards the detector, it is not possible to comment on the efficacy or otherwise of this process for the samples shown here without considerably more experimental data.

However, it is possible to speculate on the nature of an experiment that would allow spatial separation of the exciting line and the Raman line for the PMMA@Au sample.

Firstly it would be necessary to shift the dispersion of the Bragg peak into an appropriate region of the spectrum. By trial and error, it may be shown that this would lie around 800 nm, being a wavelength that is readily accessible using a Ti:sapphire laser for example [20].

For the purposes of this example it will be assumed that the most intense Raman feature occurs at ca. 1000 cm^{-1} Raman shift. In absolute terms this equates to an energy of the Raman photon arising from the 800 nm line of the laser of $12500\text{ cm}^{-1} - 1000\text{ cm}^{-1}$ (Stokes shift) = 11500 cm^{-1} . In turn this becomes equivalent to a photon of wavelength 869 nm.

Thus between the Rayleigh line scattering at 800 nm and the Raman scattering at 869 nm there is a shift equivalent to 69 nm in wavelength.

We can now apply the Bragg-Snell equation to calculate the difference between the angles at which the Bragg peak associated with each wavelength would be expected.

Appendix A

Taking the composite refractive index η_{eff} as 1.51 (see chapter 4) and assuming a layer spacing of 305 nm based on the diameter of the PMMA spheres, we obtain for the two wavelengths concerned:

$$800 \text{ nm} = 2 \times 305 \text{ nm} ((1.51)^2 - \sin^2\theta_1)^{1/2}$$

$$869 \text{ nm} = 2 \times 305 \text{ nm} ((1.51)^2 - \sin^2\theta_2)^{1/2}$$

From these two equations the values of θ_1 and θ_2 are found to be 48.45 degrees and 30 degrees respectively. Thus the angular separation between the exciting line (Rayleigh scattering) and the Raman line Bragg peaks is estimated to be 18.45 degrees. Thus it may be seen that an experiment could be devised where the Raman scattered light could be preferentially reflected from the sample as compared to the Rayleigh line.

A.3 Conclusion

Although the evidence for a true SERS effect presented here is rather tenuous, the results are of sufficient interest to warrant further studies. In addition the potential use of the photonic crystal Bragg scattering to effectively separate Raman and Rayleigh scattering has been broadly demonstrated using a simple calculation.

References

1. Link, S., Wang, Z.L. and El-Sayed, M.A. *Alloy Formation of Gold–Silver Nanoparticles and the Dependence of the Plasmon Absorption on Their Composition*. The Journal of Physical Chemistry B, 1999. **103**(18): p. 3529-3533.
2. Willets, K.A. and Van Duyne, R.P. *Localized Surface Plasmon Resonance Spectroscopy and Sensing*. 2007, Annual Review of Physical Chemistry. p. 267-297.
3. Polavarapu, L., Manga, K.K., Yu, K., Ang, P.K., Cao, H.D., Balapanuru, J. Loh K.P. and Xu, Q.-H. *Growth and galvanic replacement of silver nanocubes in organic media*. Nanoscale,, 2011,. **3**: p. 2268-2274.
4. Wang, M., Fu, J., Huang, D., Zhang, C. and Xu, Q. *Nanofibrillated cellulose as the support and reductant for the facile synthesis of Fe₃O₄/Ag nanocomposites with catalytic and antibacterial activity*. Nanoscale, 2013. **5**: p. 7913-7919.
5. Haes, A.J., Zou, S., Schatz, G.C. and Van Duyne, R.P. *A nanoscale optical biosensor: The long range distance dependence of the localized surface plasmon resonance of noble metal nanoparticles*. Journal of Physical Chemistry B, 2004. **108**(1): p. 109-116.
6. Huang, X., El-Sayed, I.H., Qian, W. and El-Sayed, M.A. *Cancer Cell Imaging and Photothermal Therapy in the Near-Infrared Region by Using Gold Nanorods*. Journal of the American Chemical Society, 2006. **128**(6): p. 2115-2120.

Appendix A

7. Bardhan, R., Grady, N.K. Cole, J.R., Joshi, A. and Halas, N.J. *Fluorescence Enhancement by Au Nanostructures: Nanoshells and Nanorods*. ACS Nano, 2009. **3**(3): p. 744-752.
8. Tian, Z.-Q., Ren, B. and Wu, D.-Y. *Surface-Enhanced Raman Scattering: From Noble to Transition Metals and from Rough Surfaces to Ordered Nanostructures*. The Journal of Physical Chemistry B, 2002. **106**(37): p. 9463-9483.
9. Fleischmann, M., Hendra, P.J. and McQuillan, A.J. *Raman spectra of pyridine adsorbed at a silver electrode*. Chemical Physics Letters, 1974. **26**(2): p. 163-166.
10. Freitag, I., Neugebauer, U., Csaki, A., Fritzsche, W., Krafft, C. and Popp, J. *Preparation and characterization of multicore SERS labels by controlled aggregation of gold nanoparticles*. Vibrational Spectroscopy, 2012. **60**: p. 79-84.
11. Fateixa, A.V., Girão, H.I.S., Nogueira, T. and Trindade *Polymer based silver nanocomposites as versatile solid film and aqueous emulsion SERS substrates*. J. Mater. Chem. , 2011. **21**: p. 15629-15636.
12. Willets, K. *Surface-enhanced Raman scattering (SERS) for probing internal cellular structure and dynamics*. Analytical and Bioanalytical Chemistry, 2009. **394**(1): p. 85-94.
13. Baumberg, J.J., Kelf, T.A., Sugawara, Y., Cintra, S., Abdelsalam, M.E., Bartlett, P.N. and Russell, A.E. *Angle-Resolved Surface-Enhanced Raman Scattering on Metallic Nanostructured Plasmonic Crystals*. Nano Letters, 2005. **5**(11): p. 2262-2267.

Appendix A

14. Mahajan, S., Cole, R.M., Soares, B.F., Pelfrey, S.H., Russell, A.E., Baumberg, J.J. and Bartlett, P.N. *Relating SERS Intensity to Specific Plasmon Modes on Sphere Segment Void Surfaces*. The Journal of Physical Chemistry C, 2009. **113**(21): p. 9284-9289.
15. Campion, A. and Kambhampati, P. *Surface-enhanced Raman scattering*. Chemical Society Reviews, 1998. **27**(4): p. 241-250.
16. Alvarez-Puebla, R.A., Dos Santos Jr, D.S. and Aroca, R.F. *Surface-enhanced Raman scattering for ultrasensitive chemical analysis of 1 and 2-naphthalenethiols*. Analyst, 2004. **129**(12): p. 1251-1256.
17. Al-Ogaidi, I., Gou, H. Al-kazaz, A.K.A., Aguilar, Z.P., Melconian, A.K., Zheng, P. and Wu, N. *A gold@silica core-shell nanoparticle-based surface-enhanced Raman scattering biosensor for label-free glucose detection*. Analytica Chimica Acta, 2014. **811**(0): p. 76-80.
18. McFarland, A.D., Young, M.A., Dieringer, J.A. and Van Duyne, R.P. *Wavelength-Scanned Surface-Enhanced Raman Excitation Spectroscopy*. The Journal of Physical Chemistry B, 2005. **109**(22): p. 11279-11285.
19. Álvarez-Puebla, R.A. *Effects of the Excitation Wavelength on the SERS Spectrum*. The Journal of Physical Chemistry Letters, 2012. **3**(7): p. 857-866.
20. Sanchez, A. and Wall, K.F. *Titanium Sapphire Lasers*. The Lincoln Laboratory Journal, 1990. **3**(3).

Preparation and Properties of Silica Inverse Opal via Self-Assembly

This Appendix is based on the publication:

Syara Kassim, *Sibu C. Padmanabhan*, Joe McGrath., and *Martyn E. Pemble*, ‘‘**Preparation and Properties of Silica Inverse Opal via Self-Assembly**’’, *Applied Mechanics and Materials*, 2015, **699**: p. 318-324

Contributions:

Syara Kassim	Prepared PMMA spheres, produced silica inverse opals and wrote the paper
Sibu Padmanabhan	Suggested correction on the paper and conceive the idea
Joe McGrath	Did characterisation on SEM and suggested correction on the paper
Martyn Pemble	Suggested corrections on the paper

Preparation and Properties of Silica Inverse Opal via Self-Assembly

Syara Kassim^{1, 2, a}, Padmanabhan S³, McGrath J¹, and Pemble M.E^{1, 3}

¹Tyndall National Institute, University College Cork, Cork, Ireland

²Universiti Malaysia Terengganu, Kuala Terengganu, Terengganu, Malaysia

³Department of Chemistry, University College Cork, Cork Ireland

^asyara.kassim@tyndall.ie

Keywords: Photonic crystals; opal; silica inverse opal; co-crystallization.

Abstract. The bottom-up colloidal synthesis of photonic band gap (PBG) materials or photonic crystals (PC) has attracted considerable interest as compared to so-called top-down lithographic approaches due to the simple processing steps involved and the prospect of the economically viable production of complex 3-dimensional optical materials from simple colloidal particles. To date self-assembly techniques constitute the most popular approach to fabricate 3D photonic crystals from colloidal particle suspensions. Based on the natural tendency of monodisperse colloidal particles to organise into ordered arrays, this method represent the best option due to the ease of fabrication, ability to produce larger area samples and cost. Here we report on the fabrication of long range three-dimensional (3D) ordered poly (methyl methacrylate) (PMMA)-silica PC structures and the subsequent fabrication of robust silica inverse opals using self-assembly methods. The optical properties of these materials are described and discussed in terms of potential applications of these materials.

Introduction

Photonic crystals (PC) are periodic structures that exhibit a spatial modulation in their dielectric function, with the periodicity of this modulation being comparable to the wavelength of light usually in the ultraviolet, visible or infrared region of the electromagnetic spectrum. Such materials are currently of high fundamental and technological interest owing to their ability to confine and control the flow of light [1]. The complex light-matter interactions in these materials produce modified wave propagation when the periodicity of the PC goes from one or two dimensions to three dimensions, where it is possible to create optical phenomena similar to those seen in natural opal gemstones, which are made from the natural assembly of colloidal silica particles. As such 3-D colloidal photonic crystals made in the laboratory are often referred to as artificial opals. The transport of electromagnetic waves in photonic crystals is determined by the so-called photonic band gap [2], which is the optical analogue of a directional band gaps for electrons that exist in semiconductors and insulators. The unique properties of photonic crystals (PC) has attracted enormous interest as they could lead to a wide range of new or improved devices including decorative coatings, sensors, photovoltaic, solar concentrators, passive optical components (filters, splitters), negative refractive index media devices such as cloaking devices, perfect (aberration free) lenses and optical interconnect technologies [3-8].

So-called 'inverted opals' are known to exhibit more complete photonic band gaps than conventional opals [9]. These materials are the negative replicas of direct opals and could be seen as an ordered array of communicating voids in a solid matrix. Preparation of their inverted structures has therefore been envisaged as an alternative way to investigate further the optical properties of such 3D structures. Unfortunately it is often the case that successful experimental investigations of inverted structures are hampered due to the difficulty in manufacturing robust 3D inverted PC structures with long range order. Infilling a second material into the interstitial lattice voids between the colloidal spheres of the opal followed by removal of the spheres is one popular way of creating the inverted structure. In order to achieve this, techniques such as chemical vapour deposition [10] and atomic layer deposition [11, 12] have been employed with a reasonable degree of effectiveness, yet these methods often require the use of potentially expensive specialist equipment. In this present

work we highlight the use of an alternative approach for the infilling of the voids in the parent material which is both simple and easy to perform, requiring no specialist equipment other than laboratory glassware.

One useful method for the reliable production of colloidal silica based photonic crystals was first performed by Jiang et al. in 1999 [13]. This method employed a suspension of the silica particles in contact with a vertical substrate onto which the particles assembled as the solvent in the suspension evaporated. The method is often called “controlled-evaporation”, “vertical deposition” and even the “Colvin” method, after the head of the group at Rice University in the USA who demonstrated the particular approach. Easy and cheap to perform, this technique has rapidly attracted a huge amount of attention. The quality of the opal obtained with the controlled-evaporation method depends on many parameters such as the sphere size and their size distribution, the volume fraction of particles, the relative humidity, the evaporation time and drying temperature [13-15]. The control of these parameters allows the control of the film thickness and quality. Films prepared in this manner form as a result of close packing which results in a face-centred cubic structure, similar to that found in natural opals, the alternative hexagonal close packed arrangement being much less commonly observed.

By borrowing from a concept for the fabrication of large area 3D ordered colloidal arrays of nanoparticles reported elsewhere [16], we have infiltrated PMMA colloidal particles (475nm) with hydrolysed TEOS to form composite silica PMMA material. Following this the PMMA crystal template was removed by solvent dissolution to produce a robust silica inverse opal. This approach promises to yield high quality, large area samples that could be used in the fabrication of many types of optical devices.

Experimental Section

PMMA colloidal spheres (475 nm) were synthesised using a procedure that we have reported previously [17]. The composite silica-PMMA was prepared via controlled evaporation self-assembly from an aqueous colloidal suspension containing the two components, namely poly(methyl methacrylate) (PMMA) spheres and tetraethylorthosilicate (TEOS) solution (Sigma Aldrich). A 0.15 volume percent PMMA suspension of the particles in Millipore water was prepared containing 0.12 ml TEOS sol. The sol made up from the hydrolysis of the TEOS in solvent medium (using ethanol : HCl (0.1 molar) : TEOS with ratio 8:1:1; respectively). A cleaned glass substrate was tilted in the mixture of the suspension (PMMA+TEOS). The addition TEOS was important as it acts as the ‘cementing component’ that holds the PMMA together in the PC backbone. The PMMA template was removed by using acetone and further calcined at 450°C on a hot plate to form a silica inverse opal. This film exhibited opalescence confirming the successful formation of a PC film. The morphology of the resulting films was studied using scanning electron microscopy (SEM). The optical properties of the 3D silica inverse opals were measured using an optical bench set-up for wavelengths, λ , ranging from 450 to 1600 nm. Collimated un-polarized white light from a tungsten lamp was focused onto the sample using an 8 cm focal length lens and the transmitted light was collected through an optical fibre to the spectrometer (Ocean optics) and the data processed by SpectraSuite software. In both the reflectance (R) and transmittance (T) mode the baseline correction was done with a bare glass substrate to eliminate the effects such as light reflection at the air-glass interface and substrate absorption, if any. For angle resolved transmission data collection, the sample mounted onto a rotational stage was rotated at angles, theta, ranging from 0 to 65°, measured from the surface normal of the (111) hexagonal plane grown parallel to the substrate surface. For reflectance measurements, the unit was rotated to collect the reflected signal at a range of angles from 10 to 65°.

Results and Discussion

SEM images of the fabricated 3D silica inverse opals are presented in Fig. 1. The SEM top view images reveal the consistency of inverse opal formed over large domain sizes, $>20\ \mu\text{m}$. The efficiency of the method can be appreciated from fact that the three-coordinate interconnects from the second layers of the (111) planes of the PC can also be observed.

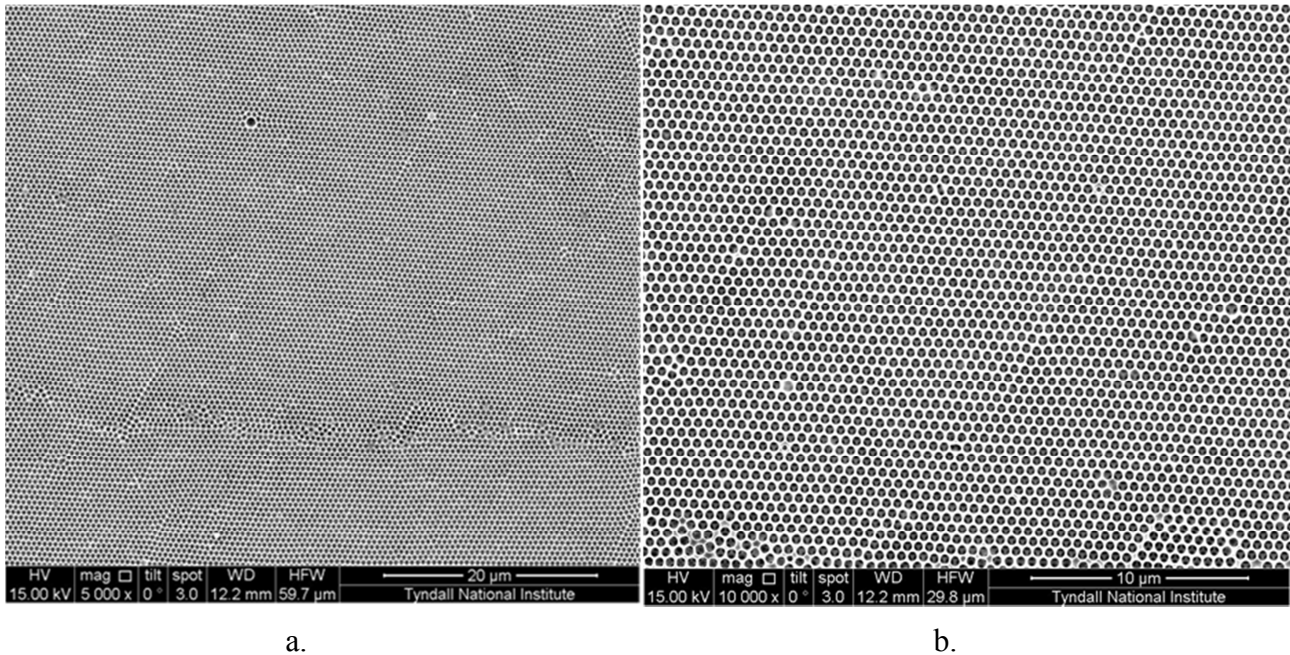


Fig. 1. Silica inverse opal structure with different magnifications. Scale bars are a. $20\ \mu\text{m}$, and b. $10\ \mu\text{m}$

Transmission spectra recorded for the bare PMMA opal as a function of angle of incidence are shown in Fig. 2. The absolute reflectance and transmission spectra recorded from a silica inverse opal consisting of 3D air spheres supported by an SiO_2 dielectric backbone are presented in Fig. 3. The presence of a reflection band, or so-called ‘stop band’ and a corresponding transmission dip centred at $864\ \text{nm}$ reveals the formation of a PBG. The bare PMMA opal shows a stop band centred at $1108\ \text{nm}$. The PBG of silica inverse opal thus exhibits a blue shift in the position of the stop band of $244\ \text{nm}$ as compared to that of the bare opal. This shift may be attributed to a combined effect of a small reduction in the effective refractive index of the material n_{eff} (composite SiO_2 : air as compared to composite PMMA: air) and a slight reduction in the lattice spacing between the layers of voids in the structure as compared to the spacing between the spheres in the parent structure, that arises because of the finite thickness of the SiO_2 layer grown between the spheres.

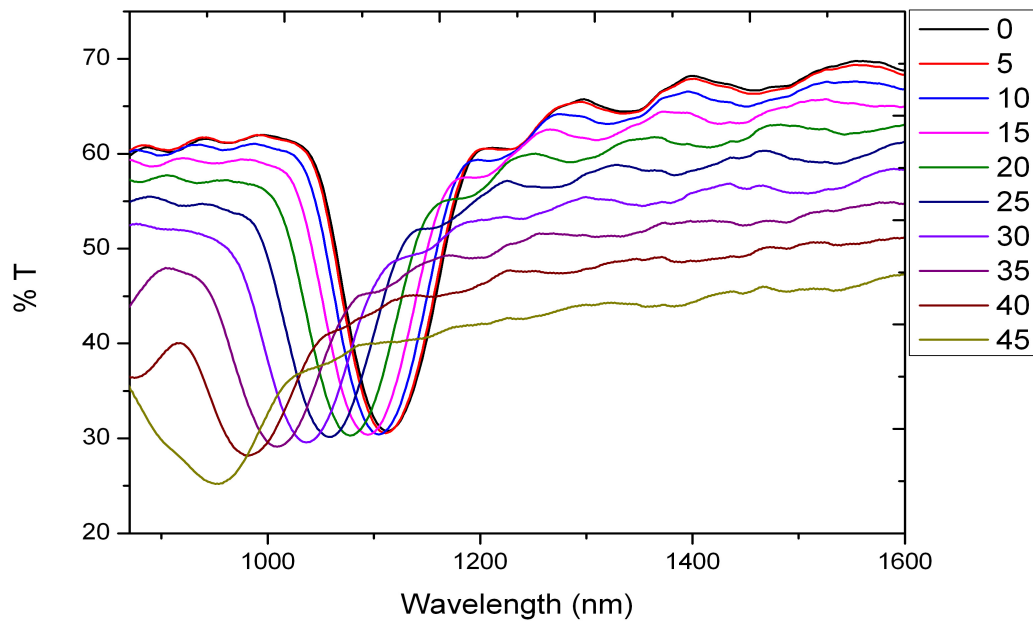


Fig. 2. Transmission spectra of the bare PMMA opal recorded as a function of angle of incidence

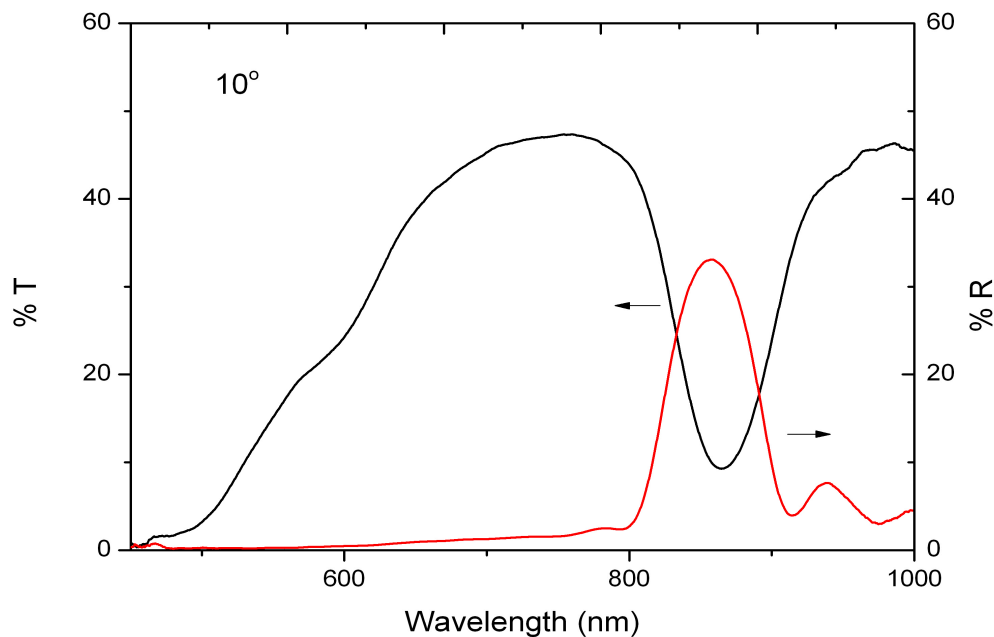


Fig. 3. Reflectance and transmission spectra recorded from the silica inverse opal at an angle of 10°

The reflectance spectrum of the silica inverse opal was also found to exhibit a shift in the position of the stop band as a function of angle of incidence, as expected for a PBG material. This observation is consistent with the expected behaviour for a photonic crystal in terms of the Bragg-Snell relationship. By altering the angle of incidence (θ), the effective refractive index (n_{eff}) and the inter planar spacing (d) can be determined by the following equation [2, 18]:

$$\lambda = 2d\sqrt{(n_{eff}^2 - \sin^2 \theta)}. \quad (1)$$

This equation is found to apply to most colloidal photonic crystals and their inverse analogues since the stop band is formed as a result of the diffraction resonance for light incident on the material surface arising from the (111) family of planes of the structure combined with refraction effects arising at the interface between the air and the material's surface.

The correlation with the Bragg-Snell relationship was further confirmed by fitting the data points obtained to a plot of the square of the wavelength maximum (λ_{\max}^2) for the stop bands recorded at varying angle of incidence angle, θ , against $\sin^2\theta$, Figure 4. The linear fit shown in Figure 4 is in complete agreement with the Bragg-Snell relationship prediction for photonic crystals. Using the plot shown in Fig. 4, n_{eff} can be measured and silica inverse opal was found to have reduced from 1.36 to 1.24 due to influence of filling fraction and change in materials.

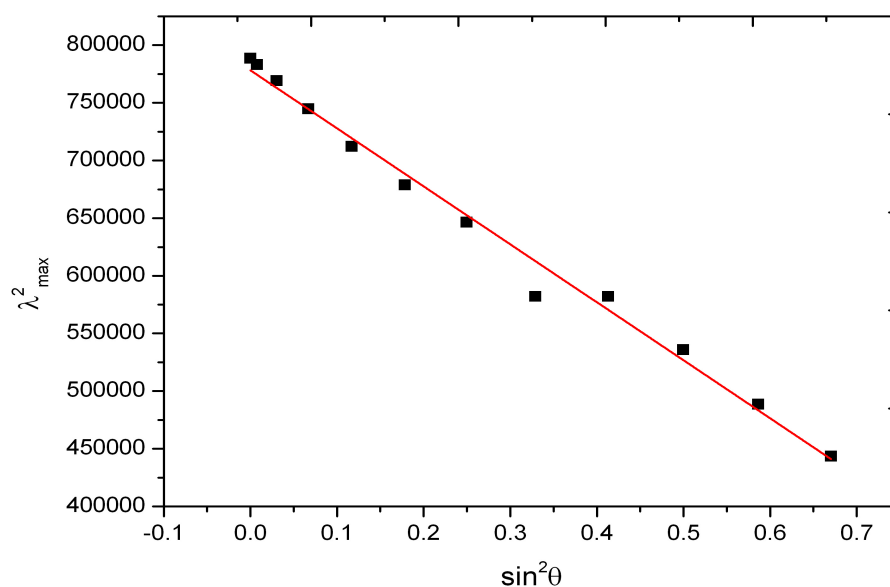


Fig. 4. Plot of λ_{\max}^2 vs $\sin^2\theta$ showing a linear fit based on silica inverse opal reflectance measurement.

The SiO_2 inverted structures were found to be quite robust and easy to handle, which suggests that the method presented here might make such materials genuinely accessible for applications where increased refractive index contrast is desirable. Such applications could include passive components such as mirrors and filters, or active components such as optical sensors where a high degree of discrimination between various wavelengths of light is required.

Conclusion

A simple and easy method for the infiltration of TEOS and its subsequent reaction to SiO_2 in the interstitial voids of a PMMA opal is reported. The infiltration was carried out using the one-step method involving co-crystallization of both TEOS and the PMMA spheres during self-assembly via a controlled evaporation process. The silica inverse opal exhibits a blue shift in the stop band as compared to that of the bare PMMA opal which we attribute to a reduction in effective refractive index and a reduction in the effective lattice spacing of the layers of voids in the inverted structure as compared to that of the layers of spheres in the bare PMMA structure. Optical reflectance measurements were made at various angles of incidence show good correlation using Bragg-Snell equation.

Acknowledgement

The support of Science Foundation Ireland for Principal Investigator Grants Numbers 11/PI/1117 and 07/IN.1/I787 is gratefully acknowledged. The support of the Universiti Malaysia Terengganu and Ministry of Higher Education Malaysia for funding a studentship for SK is also gratefully acknowledged.

References

- [1] Yablonovitch E., Inhibited spontaneous emission in solid-state physics and electronics *phys rev lett* (1987) 2059-62.
- [2] Waterhouse GIN, Waterland MR. Opal and inverse opal photonic crystals: Fabrication and characterization. *Polyhedron* 26 (2007) 356-68.
- [3] M. Bardosova FCD, M. E. Pemble, I. M. Povey, and R. H. Tredgold, Langmuir-Blodgett assembly of colloidal photonic crystals using silica particles prepared without the use of surfactant molecules. *Journal of colloid and interface science* 333 (2009) 816-9.
- [4] Yin JGaY. Responsive photonic crystals. *Angewandte Chemie (International ed in English)* 50 (2011) 1492-522.
- [5] Ge X, Wang M, Wang H, Yuan Q, Liu H, Tang T., Novel walnut-like multihollow polymer particles: synthesis and morphology control. *Langmuir* 26 (2010) 1635-41.
- [6] Sathish Kumar PS, Manivel A, Anandan S., Synthesis of Ag-ZnO nanoparticles for enhanced photocatalytic degradation of acid red 88 in aqueous environment. *Water Sci Technol* 59 (2009) 1423-30.
- [7] Galisteo JF, García-Santamaría F, Golmayo D, Juárez BH, López C, Palacios E., Self-assembly approach to optical metamaterials. *Journal of Optics A: Pure and Applied Optics* 7 (2005) 244.
- [8] Fudouzi H., Optical properties caused by periodical array structure with colloidal particles and their applications. *Advanced Powder Technology* 20 (2009) 502-8.
- [9] F. Meseguer AB, and H. Míguez, Synthesis of inverse opals. *Colloids and Surfaces A: Physicochemical and Engineering Aspects* 202 (2002) 281–90.
- [10] Zakhidov AA, Khayrullin II, Baughman RH, Iqbal Z, Yoshino K, Kawagishi Y, et al., CVD synthesis of carbon-based metallic photonic crystals. *Nanostructured Materials* 12 (1999) 1089-95.
- [11] King JS, Graugnard E, Summers CJ. TiO₂ inverse opals fabricated using low-temperature atomic layer deposition. *advanced materials* 17 (2005) 1010-3.
- [12] Povey IM, Whitehead D, Thomas K, Pemble ME, Bardosova M, Renard J., Photonic crystal thin films of GaAs prepared by atomic layer deposition. *Applied Physics Letters* 89 (2006).
- [13] P. Jiang JFB, K. S. Hwang, and V. L. Colvin, Single-crystal colloidal multilayers of controlled thickness. *chem mater* 11 (1999) 2132–40.
- [14] G. Q. Liu ZSW, and Y. H. Ji. Influence of growth parameters on the fabrication of high-quality colloidal crystals via a controlled evaporation self-assembly method thin solid films 518 (2010) 5083–90.

[15] Zhang J, Z. Sun, and B. Yang, Self-assembly of photonic crystals from polymer colloids. *Current Opinion in Colloid & Interface Science* 2 (2009) 103-14.

[16] Hatton B, Mishchenko L, Davis S, Sandhage KH, Aizenberg J., Assembly of large-area, highly ordered, crack-free inverse opal films. *Proceedings of the National Academy of Sciences* 107 (2010) 10354-9.

[17] Kassim S, Padmanabhan SC, Salaun M, Pemble ME, PMMA-Gold metallodielectric photonic crystals and inverse opals: preparation and optical properties. *AIP Conference Proceedings* 2011;1391:263-5.

[18] Schroden R, Balakrishnan N., inverse opal photonic crystals a laboratory guide. University of Minnesota, 2001, pp. 1-32.

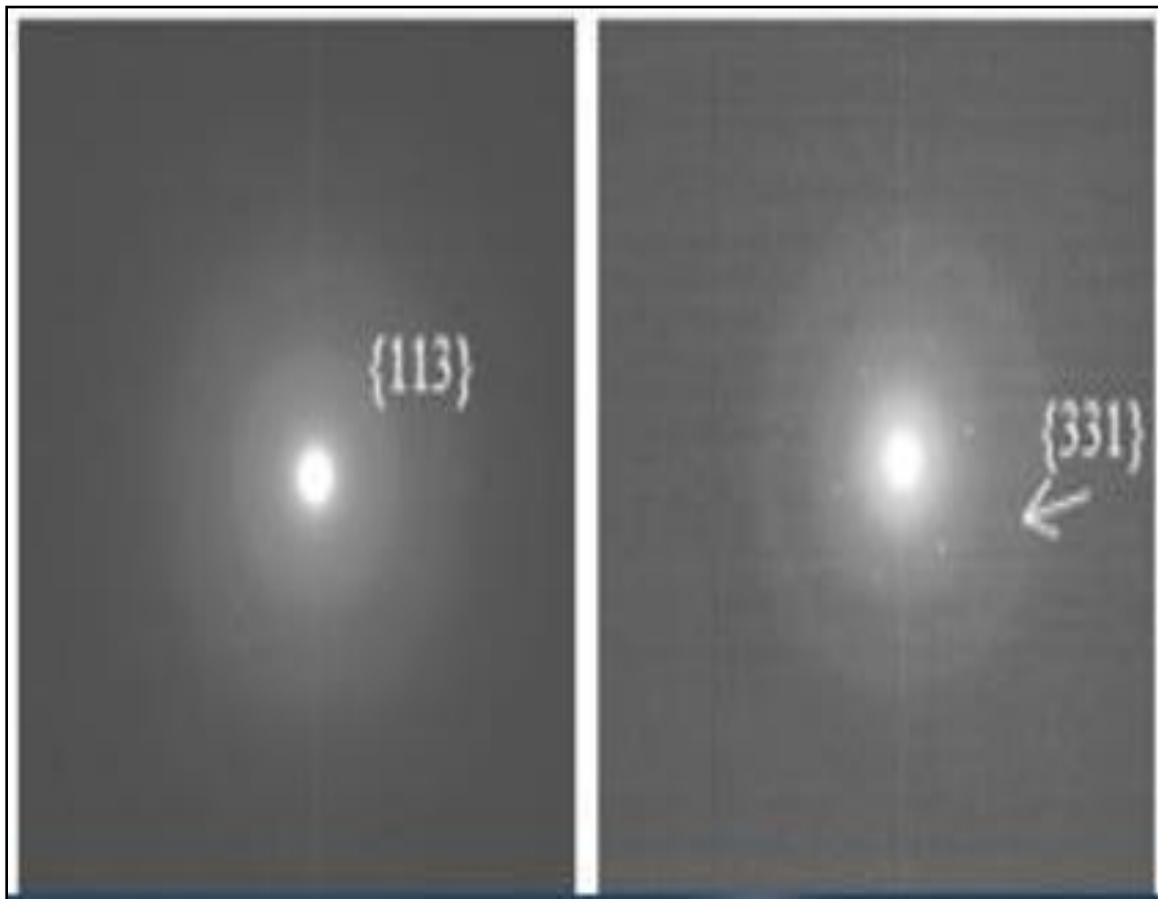
Sustainable Energy and Development, Advanced Materials

10.4028/www.scientific.net/AMM.699

Preparation and Properties of Silica Inverse Opal via Self-Assembly

10.4028/www.scientific.net/AMM.699.318

Chapter 7, Figure 1 (f) & (h) enlarged for clarity.



The rings represent the {113} and {331} planes of silicon.

List of Publications and Conference Presentations

1. *Syara Kassim, Siby C. Padmanabhan, Mathieu Salaun, and Martyn E. Pemble, ‘PMMAGold Metallodielectric Photonic Crystals and Inverse Opals: Preparation and Optical Properties’*, AIP Conference Proceedings, 2011. **1391(1)**: p. 263-265.
2. *Siby C. Padmanabhan, Keith Linehan, Shane O’Brien, Syara Kassim, Hugh Doyle, Ian M. Povey, Martyn E. Pemble, ‘A bottom-up fabrication method for the production of visible light active photonic crystals’*, J. Mater. Chem. C, 2014, **2(9)**: p. 1675-1682.
3. *Syara Kassim, Siby C. Padmanabhan, Joe McGrath., and Martyn E. Pemble, ‘Preparation and Properties of Silica Inverse Opal via Self-Assembly’*, Applied Mechanics and Materials, 2015, **699**: p. 318-324
4. *Syara Kassim, Siby C. Padmanabhan and Martyn E. Pemble, ‘Synthesis Poly(methyl methacrylate)-Gold Core Shell Metallodielectric Photonic Crystals’* Will be submitted to Journal of Materials Chemistry.
5. *Siby C. Padmanabhan, Syara Kassim, Min Yan, Min Qiu and Martyn E. Pemble, ‘Three-dimensional colloidal metallodielectric photonic crystals with optical band gaps’* will be submitted to Journal of Materials Chemistry

Appendix D

1. Syara Kassim, Siby C. Padmanabhan and Martyn E. Pemble, “**PMMA-Gold Metallodielectric Photonic Crystals and Inverse Opals: Preparation and Optical Properties**”, 1st International Symposium on Colloids and Materials 8-11 May 2011, Amsterdam, the Netherlands (Poster)
2. Siby C. Padmanabhan, Syara Kassim and Martyn E. Pemble “**Metallodielectric photonic crystals from engineered nano-building blocks: New ways of light matter interactions**”, Photonics Ireland, 7-9 September 2011, Malahide, Dublin, Ireland (Poster)
3. Syara Kassim, Siby C. Padmanabhan, and Martyn E. Pemble “**Polymer and Metallodielectric based Photonic Crystal**”, SFP7 “PhANTASY” NATO ASI, Nanomaterials and Nano Architectures, Advanced Study Institute NATO, 30th June to 7th July 2013 (Poster)
4. Syara Kassim, and Martyn E. Pemble “**Polymer and Metallodielectric based Photonic Crystal**”, PhD Research Day 2011, University College Cork, Cork, Ireland (Poster)
5. Syara Kassim, Siby C. Padmanabhan, and Martyn E. Pemble, “**PMMAGold Metallodielectric Photonic Crystals and Inverse Opals: Preparation and Optical Properties**” OPTICS’11 : A Conference on Light, 23–25 May 2011, Kerala, India (Poster)

Appendix D

6. Syara Kassim, and Martyn E. Pemble “**Polymer and Metallodielectric based Photonic Crystal**”, PhD Research Day 2012, University College Cork, Cork, Ireland (Talk)
7. Siby C. Padmanabhan, Syara Kassim, Maria Bardosova and Martyn E. Pemble “**Photonic and Plasmonic Coupling in Gold/Silicon Dioxide Incorporated Colloidal PMMA Photonic Crystals and Inverted Structures**”, MRS Spring meeting, Metamaterials and Plasmonics April 26 - 29, 2011 San Francisco, California (Talk)
8. Syara Kassim, Joe McGrath, Siby Padmanabhan, and Martyn E. Pemble “**Preparation and Properties of Silica Inverse Opal via Self-Assembly**”, 3rd International Conference and Exhibition on Sustainable Energy and Advanced Materials (ICE-SEAM 2013) 30–31 October 2013, Melaka, Malaysia (Talk)